The Single Degenerate Progenitor Scenario for Type Ia Supernovae and the Convective Urca Process

A Dissertation presented

by

Donald Eugene Willcox

to

The Graduate School

in Partial Fulfillment of the

Requirements

for the Degree of

Doctor of Philosophy

in

Physics

Stony Brook University

August 2018

Stony Brook University

The Graduate School

Donald Eugene Willcox

We, the dissertation committe for the above candidate for the

Doctor of Philosophy degree, hereby recommend

acceptance of this dissertation

Alan Calder – Dissertation Advisor
Associate Professor, Physics and Astronomy

Michael Zingale – Chairperson of Defense
Associate Professor, Physics and Astronomy

Joanna Kiryluk – Committee Member
Associate Professor, Physics and Astronomy

Matthew Reuter – External Committee Member
Assistant Professor, Applied Mathematics and Statistics

This dissertation is accepted by the Graduate School

Charles Taber
Dean of the Graduate School

Abstract of the Dissertation

The Single Degenerate Progenitor Scenario for Type Ia Supernovae and the Convective Urca Process

by

Donald Eugene Willcox

Doctor of Philosophy

in

Physics

Stony Brook University

2018

This dissertation explores the effects of properties of the progenitor massive white dwarf (WD) on thermonuclear (Type Ia) supernovae. It includes a study of explosions from "hybrid" C/O/Ne progenitors and focuses primarily on the convective Urca process occurring in C/O progenitors shortly before their explosion. Pre-supernova WDs approaching the Chandrasekhar mass can possess sufficiently high central densities that ^{23}Na synthesized via ^{12}C fusion undergoes electron capture to ^{23}Ne. Convection sweeps ^{23}Ne to regions of lower density where it reverts via beta decay to ^{23}Na, and vice versa. Cyclic weak nuclear processes of this type constitute the convective Urca process in WDs. It has long been theorized that the convective Urca process significantly influences stellar structure at ignition by opposing convective buoyancy, redistributing energy, and driving energy losses via neutrino emission. Nevertheless, studies to date have been unable to capture three-dimensional convection in numerical simulations of the convective Urca process because of the severe timestep limitations that low-Mach number convection presents for compressible hydrodynamics codes. As a result, the physical implications of the convective Urca process have remained a significant systematic uncertainty for the origins of Type Ia supernovae (SNIa). I present new three-dimensional simulations of the convective Urca process in WDs using the low-Mach hydrodynamics code Maestro. I compare these simulations with previous studies of the convective Urca process in one and two dimensions and discuss the ramifications of a physical, three dimensional treatment of turbulence. Finally, I discuss the implications of these results for the thermonuclear runaway stage leading to the final incineration of the WD as a SNIa.

Dedication Page

This page is optional.

Frontispiece

The frontispiece is generally an illustration, and is an optional page.

Table of Contents

List of Figures/Tables/Illustrations

Preface

This page is optional.

Acknowledgements

The content in section 2 is reproduced from an article published in the *Astrophysical Journal* (Willcox et al., 2016) with minor formatting modifications. The content in subsection 5.2 is adapted with minimal modification from an article published in the *Journal of Open Source Software* (Willcox & Zingale, 2018).

This work was supported in part by the Department of Energy under grant DE-FG02-87ER40317. An award of computer time was provided by the Innovative and Novel Computational Impact on Theory and Experiment (INCITE) program. This research used resources of the Oak Ridge Leadership Computing Facility located in the Oak Ridge National Laboratory, which is supported by the Office of Science of the Department of Energy under Contract DE-AC05-00OR22725. Projects AST106 and AST106SBU supported use of the ORNL/Titan resource. This research used resources of the National Energy Research Scientific Computing Center, which is supported by the Office of Science of the U.S. Department of Energy under Contract No. DE-AC02-05CH11231. Results in this dissertation were obtained using the high-performance computing system at the Institute for Advanced Computational Science at Stony Brook University. This research has made use of NASA's Astrophysics Data System Bibliographic Services.

1 Introduction

1.1 Type Ia Supernovae

Type Ia Supernovae (SNIa) are rare, brilliant explosions that incinerate approximately 1 $M_\odot$ of ^{12}C and ^{16}O in an electron-degenerate environment (Hoyle & Fowler, 1960; Arnett et al., 1971), emitting a peak luminosity comparable to that of an entire galaxy comprising hundreds of billions of stars. SNIa are not only of theoretical interest but also practical utility for cosmological research, since they can provide observers with distance measurements to the SNIa host galaxies. This application takes advantage of the empirical relation between different SNIa explosions in that brighter explosions decay from their peak luminosity more slowly than less luminous explosions, originally described by Phillips (1993). Using this Phillips relation, observers can standardize SNIa based on their measured luminosity and light curve decay time to extract the explosion luminosity, and thereby, the distance to the explosion. Combining this luminosity distance with the redshift of the host galaxy then allowed cosmologists to infer that the expansion of the Universe is accelerating, thereby introducing the dark energy problem, as the reason for this acceleration is not presently understood (Perlmutter et al., 1997; Riess et al., 1998).

The physical basis for the Phillips relation is that the luminosity is determined by the mass of unstable ^{56}Ni synthesized by the chain of fusion reactions occurring during the explosion (Colgate & McKee, 1969). Similarly, the opacity of the ejecta is dominated by the line opacity of low-ionization iron group elements synthesized during the explosion since such Fe group elements have $\approx 10\times$ the number of lines compared to low-ionization intermediate-mass elements such as Si, S, or Ca (Mazzali et al., 2001; Mazzali & Podsiadlowski, 2006). As ^{56}Ni is one of the Fe group elements, the same physical mechanisms that set the amount of Fe group elements synthesized will correlate the explosion luminosity with the ejecta opacity.

In spite of the brilliance of these explosions, it has been difficult to identify the system or systems in which these explosions originate. Not only do SNIa occur at the low rate of 1-2 per century, per galaxy (see Maoz & Mannucci (2012) for a detailed review of SNIa rates), but it is also not possible at present to observe the progenitor prior to the explosion, which then leaves no bound remnant. Nevertheless, the explosion energy and light spectra emitted by the ejected material do indicate certain properties of the progenitor system, giving rise to several theoretical models for SNIa explosion mechanisms. The composition and mass of the material consumed in the explosion is consistent with that of one or more white dwarf (WD) stars, the endpoints of stellar evolution for stars with main-sequence masses below approximately $5 - 7$ $M_\odot$, where this range depends on uncertainties in the ^{12}C burning rate (Chen et al., 2014). White dwarfs are composed of ^{12}C and ^{16}O with an average mass around $0.6 - 0.7$ $M_\odot$ (Tremblay et al., 2016) and support themselves against gravitational collapse via electron degeneracy pressure in their dense cores. Because electron degeneracy pressure is sufficient to support a WD below the Chandrasekhar mass (≈ 1.4 $M_\odot$), such a WD will not collapse to ignite ^{12}C fusion following the exhaustion of ^4He fuel within its core.

1.2 Progenitor Models for SN Ia

Solitary $0.6 - 0.7$ $M_\odot$ WDs are therefore stable and will not explode as SNIa, so a variety of models have been proposed to explain how such events may occur. One such model involves the merger of two WDs in a binary star system, where their orbits decay due to gravitational wave emission leading to an inspiral and merger event Iben & Tutukov (1984); Webbink (1984). Such an event could lead to ignition of the WDs either during or following the inspiral, especially if the WD combined masses exceeded the Chandrasekhar mass. This scenario has been explored most recently by Moll et al. (2014); Dan et al. (2014); Kashyap et al. (2015); Sato et al. (2015); Tanikawa et al. (2015); Katz et al. (2016) and is an area of ongoing research. A similar model to the WD merger scenario is the collision of two WDs, proposed by Rosswog et al. (2009), in which two WDs in a triple system are destabilized in their orbits by a third star, leading to a head-on or glancing collision that initiates a detonation in the contact region. The collision model is thought to be less likely to occur than WD mergers due to the very precise conditions required to cause such a collision Livio & Mazzali (2018), but both models are being explored in the literature. A third scenario is the double detonation model in which a WD with a mass below the Chandrasekhar limit possesses a ^{4}He shell of accreted material which supports convective ^{4}He-burning that undergoes a detonation via local thermonuclear runaway. Such a detonation would initiate a shockwave that would compress the C-O WD core below the ^{4}He shell, and could potentially initiate a secondary detonation of the C-O WD core via ^{12}C fusion, as for example was recently investigated by Shen & Bildsten (2014). The conditions for detonation as well as the convective processes leading to detonation of the ^{4}He shell are current areas of research, as for example, in Zingale et al. (2013); Jacobs et al. (2016). The WD merger, collision, and double-detonation models all incorporate WDs with masses similar to those seen commonly in nature and so they do not require that the WD gain mass over a long period of time.

If a single WD were able to gain mass via accretion from a companion star, it would become dynamically unstable as it approached 1.4 $M_\odot$ and support a thermonuclear runaway due to the temperature sensitivity of ^{12}C burning (Nomoto et al., 1984; Woosley & Weaver, 1986). This is the general picture of the single-degenerate paradigm for SNIa progenitors, and there are various hypotheses for the mechanics of the thermonuclear runaway involving pure deflagrations, detonations, or some combination thereof. A great deal of theoretical and computational effort has been devoted to exploring the properties of such explosions and predicting various observables of the explosion, such as the recent work of García-Senz & Bravo (2005); Röpke et al. (2007); Jordan et al. (2008); Krueger et al. (2010); Calder et al. (2010); Krueger et al. (2012); Miles et al. (2016). Because the degree of neutronization of the ejecta is sensitive to the density at which burning occurs, it is highly dependent on the speed of the flame front burning through the WD and on whether there is sufficient time for thermal expansion of the WD to occur (Livne & Arnett, 1993). Studies such as Khokhlov (1991); Höflich et al. (1995) also favor a transition from an initially subsonic deflagration to a supersonic detonation front as the WD is consumed. For further discussion, see section 2, which presents the deflagration to detonation transition paradigm in further detail and uses this mechanism to carry out explosion simulations for C-O and C-O-Ne WDs in a comparison study.

In the single degenerate paradigm, the accretion phase and corresponding heating and contraction of the WD core initiate a period of several thousand years of convective simmering. During this simmering period, the central temperature of the WD is sufficient to ignite ^{12}C fusion that powers convection within the WD core. As the WD continues to gain mass, ^{12}C accelerates, driving the growth of the convective core to encompass more of the WD. This continues for as long as convection remains efficient at transporting heat away from the WD core. The two relevant timescales for this process are the convective eddy turnover time and the nuclear energy generation timescale Woosley et al. (2004), and ^{12}C burning remains stable so long as the convective eddy turnover time is shorter than the nuclear energy generation timescale. This continues until the two timescales are comparable, at which point the WD central temperature rises rapidly and initiates a thermonuclear runaway due to the extreme dependence of the ^{12}C fusion rate on temperature. For example, Woosley et al. (2004) show that the energy generation rate from ^{12}C fusion depends on temperature T as T^{23} around typical ignition temperatures of $6 - 8 \times 10^8$ K. At this point, the explosion mechanisms of deflagration and detonation come into play. However, the exact structure of the convective WD core at thermonuclear runaway in the single degenerate progenitor model is highly uncertain due to the effects of the convective Urca process.

1.3 The Convective Urca Process

The convective Urca process describes the effect of electron capture and beta decay reactions which interchange a pair of nuclei (A, Z) and $(A, Z-1)$ depending on the local density, temperature, and composition. In all cases, the electron capture reactions occur at densities sufficiently high that the electron energy is greater than the threshold energy for the electron capture process. Conversely, the beta decay reactions occur when there is sufficient phase space available at lower densities for the emitted electron to occupy. Each electron capture or beta decay reaction produces a neutrino or anti-neutrino, respectively, and these neutrinos freely escape from the WD since the WD core densities are only several 10^9 g cm^{-3}. These neutrinos present an energy loss mechanism, while the electrons involved in these reactions serve to transport energy as convection carries the nuclei within the WD core. Several such pairs of nuclei are relevant to the convective simmering phase in WDs, but the most influential is the A = 23 pair, ^{23}Na/^{23}Ne and is the subject of the bulk of this dissertation.

The convective Urca process was introduced by Paczyński (1972) as an energy loss mechanism to delay thermonuclear runaway of the WD. Follow up analytical work by Bruenn Bruenn (1973) accounted for heating due to the relaxation of the electron distribution in regions of higher density than the electron capture threshold and argued that the convective Urca process would not stabilize the WD core against thermonuclear runaway. Subsequent studies using analytic results and 1D stellar evolution models Couch & Arnett (1973, 1974, 1975); Lazareff (1975); Iben (1978b,a, 1982) showed that the convective Urca process is a complex phenomenon that depends on the detailed structure of convection in the WD core. Nevertheless, the long timescales involved in the WD convective simmering phase were historically out of reach for full 3D hydrodynamic simulations necessary to address this problem.

More recently, Stein & Wheeler (2006) simulated convection in 2D with the DWARF implicit hydrodynamics code in order to evaluate the interaction between electron capture,

β^--decay, and convection, but this study was limited to a 2D wedge of the star. Depending on the conditions chosen, Stein & Wheeler (2006) showed that it was possible for the A = 23 convective Urca process to limit the extent of the core convection zone to the interior of the A = 23 Urca shell. This is a critical result, as the extent of the convection zone across the A = 23 Urca shell is important in the energy evolution of the core (as a result of the convective Urca process) and is not possible to constrain based on 1D models. For example, the approach taken by Denissenkov et al. (2015) (c.f. their Figure 9) for 1D models is to calculate the evolution of WDs with many different assumptions about the structure of the convection zone around the A = 23 Urca shell and then compare the results of these assumptions on the desired evolution path. Recent work has included the convective Urca process in 1D stellar evolution calculations (Lesaffre et al., 2005; Denissenkov et al., 2013, 2015; Martínez-Rodríguez et al., 2016; Schwab et al., 2017a,b), but the limitation of 1D stellar structure models is that they must make simplifying assumptions about the turbulent convective flow, an inherently 3D phenomenon in nature.

Most of the work of this dissertation is to construct 3D WD models of the convective Urca process for the A = 23 Urca pair and quantify its effects on convection using the low Mach hydrodynamics code Maestro. We focus on the time during the WD simmering phase when the convection reaches the A = 23 Urca shell. In section 4 we present our computational methodology and microphysics implementation. We detail construction of our reaction network in section 5 along with general purpose tools we published as a result of this work. We then discuss our construction of appropriate 3D models of the A = 23 Urca process in section 6. Then in section 7 we present exploratory simulations using Maestro to model the WD convection in 3D for a series of central densities in order to clarify the influence of the convective Urca process with a realistic convective velocity field. We then discuss the ramifications of our results and outline questions for further study.

2 Explosions from C/O/Ne White Dwarfs

My initial research evaluated the suitability of "hybrid" C-O-Ne WDs as potential progenitors of SNIa-like events. Such stars were predicted by stellar evolution mixing length theory in the literature as a possible endpoint for SAGB stars given certain assumptions of the role of convective boundary mixing. Using the reaction network code Torch, I conducted a series of ZND detonation calculations to show that even in the carbon-poor core of such a WD, a fuel mixture of ^{12}C, ^{20}Ne, and ^{16}O could support a detonation with nucleosynthesis reaching nuclear statistical equilibrium.

I then simulated suites of explosions from these "hybrid" WDs as well as C-O WDs using the FLASH code and the deflagration to detonation transition (DDT) mechanism to determine how explosions from these different progenitors would compare. This entailed mapping a representative C-O-Ne WD MESA model from Denissenkov et al. (2015) into FLASH and constructing a parameterized set of ignition conditions in 2D, axisymmetric FLASH simulations to sample a variety of possible ignition geometries and burned masses. I found that if such a "hybrid" WD were to undergo thermonuclear runaway via a DDT, the explosion would unbind the WD, producing a comparable amount of ^{56}Ni as for C-O WDs while depositing significantly less kinetic energy in the ejecta. This work on "hybrid" WDs was the basis for my first publication as Willcox et al. (2016), reproduced as follows. For a further discussion of these results in the context of similar explosion studies for C-O WDs, see Calder et al. (2017).

The Astrophysical Journal, 832:13 (14pp), 2016 November 20 doi:10.3847/0004-637X/832/1/13

TYPE Ia SUPERNOVA EXPLOSIONS FROM HYBRID CARBON–OXYGEN–NEON WHITE DWARF PROGENITORS

Donald E. Willcox[1], Dean M. Townsley[2], Alan C. Calder[1,3], Pavel A. Denissenkov[4,5], and Falk Herwig[4,5]
[1] Department of Physics and Astronomy, Stony Brook University, Stony Brook, NY 11794-3800, USA; donald.willcox@stonybrook.edu
[2] Department of Physics and Astronomy, The University of Alabama, Tuscaloosa, AL 35487-0324, USA
[3] Institute for Advanced Computational Sciences, Stony Brook University, Stony Brook, NY 11794-5250, USA
[4] Department of Physics and Astronomy, University of Victoria, PO Box 1700, STN CSC, Victoria, BC V8W 2Y2, Canada
[5] Joint Institute for Nuclear Astrophysics, Notre Dame, IN 46556, USA
Received 2016 February 19; revised 2016 August 31; accepted 2016 September 1; published 2016 November 11

ABSTRACT

Motivated by recent results in stellar evolution that predict the existence of hybrid white dwarf (WD) stars with a C–O core inside an O–Ne shell, we simulate thermonuclear (Type Ia) supernovae from these hybrid progenitors. We use the FLASH code to perform multidimensional simulations in the deflagration-to-detonation transition (DDT) explosion paradigm. Our hybrid progenitor models were produced with the MESA stellar evolution code and include the effects of the Urca process, and we map the progenitor model to the FLASH grid. We performed a suite of DDT simulations over a range of ignition conditions consistent with the progenitor's thermal and convective structure assuming multiple ignition points. To compare the results from these hybrid WD stars to previous results from C–O WDs, we construct a set of C–O WD models with similar properties and similarly simulate a suite of explosions. We find that despite significant variability within each suite, trends distinguishing the explosions are apparent in their ^{56}Ni yields and the kinetic properties of the ejecta. We compare our results with other recent work that studies explosions from these hybrid progenitors.

Key words: hydrodynamics – nuclear reactions, nucleosynthesis, abundances – supernovae: general – white dwarfs

1. INTRODUCTION

Type Ia supernovae (SNe Ia) are bright stellar explosions that produce $\sim 0.6\,M_{\odot}$ of radioactive ^{56}Ni, the decay of which powers the light curve and leads to a relation between the peak brightness of an event and the rate of its decline from maximum (Phillips 1993). This relation enables SNe Ia to be used as "standard candles" for cosmological studies, and this use led to the discovery that the expansion of the universe is accelerating due to dark energy (Riess et al. 1998; Perlmutter et al. 1999; Leibundgut 2001).

Despite intense study (driven in part by their application as distance indicators for cosmology), we still have only an incomplete understanding of the explosion mechanism, and fundamental questions, such as the likely progenitor system(s), persist. It is widely accepted that SNe Ia result from the thermonuclear explosion of a white dwarf (WD) composed largely of C and O, with this understanding going back many decades (Hoyle & Fowler 1960; Arnett et al. 1971). The rapid thermonuclear fusion of C and O in a WD releases enough energy to unbind it, produces the ^{56}Ni necessary to power the light curve, and explains the lack of H observed in the spectra.

There are, however, several possible progenitor systems for such a configuration. All models involve a binary system and at least one C–O WD, which follows from the original association of SNe Ia with C–O burning under degenerate conditions (Hoyle & Fowler 1960). Some proposed systems posit a single WD, the single-degenerate (SD) paradigm, and some posit the merger or collision of two WDs, the double-degenerate (DD) paradigm, and within these are variations.

The "classic" model is the Chandrasekhar-mass model, in which a WD gains mass from a companion, a main-sequence or red giant star, or perhaps an He WD, and a thermonuclear runaway occurs just as it approaches the Chandrasekhar limiting mass (Hoyle & Fowler 1960; Truran & Cameron 1971; Whelan & Iben 1973; Nomoto et al. 1984). Alternately, in the sub-Chandrasekhar-mass scenario, explosive burning in the accreted layer triggers a detonation at the surface or in the core of a lower-mass WD (Nomoto 1980; Woosley et al. 1980; Sim et al. 2010).

The other main class of models is the DD progenitor (Webbink 1984; Iben & Tutukov 1984), in which two WDs inspiral and merge. This scenario includes inspiraling pairs, collisions, violent mergers, and also the "core-degenerate" model, where the merger takes place in a common envelope (Raskin et al. 2009; Kashi & Soker 2011; Pakmor et al. 2011, 2012; Shen et al. 2012). Also see Hillebrandt & Niemeyer (2000), Howell (2011), Hillebrandt et al. (2013), and Calder et al. (2013) for additional discussion.

The observational evidence of one progenitor versus another is conflicting. SNe Ia show a wide range of luminosities and also the possibility that there are two classes of progenitor (-Mannucci et al. 2006; Howell et al. 2009; Howell 2011). Observational and population synthesis (Yungelson & Livio 2000; Maoz 2008; Toonen et al. 2012; Claeys et al. 2014) arguments suggest that there simply may not be enough Chandrasekhar-mass progenitors to explain the observed SN Ia rate. There is, however, disagreement over the significance of these observations (Hachisu et al. 2008), and our understanding of the different progenitor systems is subject to uncertainties in aspects of their pre-SN evolution, including the effects of self-absorption on the number of supersoft X-ray sources predicted from the SD channel (Nielsen et al. 2013). Certainly there is disagreement in the interpretation of observations that stems from uncertainty in the accretion phase of SD evolution (Hachisu et al. 2010).

Additionally, the oft-cited claim that the WD in the SD channel would lose mass via nova explosions, thereby preventing it from reaching the Chandrasekhar mass, is questioned on the basis of high observed WD masses in

cataclysmic variables (CVs) relative to pre-CVs (Zorotovic et al. 2011). Prior work on novae and rapidly accreting WDs strongly suggests that novae will not be able to grow (Denissenkov et al. 2013a, 2014), especially not from WD masses of 0.83 $M_{\odot}$, suggested to be the mean mass of WDs in CVs in Zorotovic et al. (2011). Recently, binary population synthesis calculations by Wijnen et al. (2015) explored both thermal timescale mass transfer and mass increase during novae as potential solutions, finding that both mechanisms result in contradictions with observations and cannot satisfy the observed WD mass difference.

However, if it is possible to get an SN Ia out of the SD scenario, then "hybrid" C–O–Ne WDs (WDs with a C–O core in an O–Ne shell; Denissenkov et al. 2015) may play a key role (see Section 2). Prior stellar evolution work by García-Berro et al. (1997) produced an O–Ne WD with a ^{12}C abundance as high as 0.048 and suggested that this is sufficient to ignite an explosion if the WD accreted matter to approach the Chandrasekhar mass. The hybrid WD of Denissenkov et al. (2015) has a significantly higher average ^{12}C abundance of 0.17, and such WDs would provide readily ignitable SN Ia progenitors that are already very close to the Chandrasekhar limiting mass and are therefore perhaps the most likely to produce a SN Ia.

Acknowledging the ignitability of hybrid C–O–Ne WDs, Wang et al. (2014) and Meng & Podsiadlowski (2014) presented binary population synthesis studies for these hybrid WDs and suggested that they find consistency with the observed properties of Type Iax events, though uncertainties remain in estimating the rate of SNe Ia from hybrid WDs due to the uncertain carbon-burning rate and common-envelope ejection efficiency. The study we present here addresses SN Ia explosions from these hybrid models, and other research groups have also recently explored this possibility using hydrodynamic simulations. Kromer et al. (2015) performed pure deflagration simulations from C-core models, and Bravo et al. (2016) simulated explosions from a variety of progenitor models, including WDs with similar stellar evolution to those of Denissenkov et al. (2015). We compare these explosion studies to ours in the discussion below.

While there is uncertainty, some contemporary observations do strongly support the SD progenitor. Events like PTF11kx and others show distinct circumstellar shells of material that can be best explained in the SD context (Dilday et al. 2012; Silverman et al. 2013). The supernova remnant 3C 397 is heralded as a case where only an explosion from a Chandrasekhar-mass progenitor can produce the nuclei seen in the remnant, due to the need for electron captures at high density (Yamaguchi et al. 2015). The recent observation of a UV pulse (Cao et al. 2015) in the early evolution of an SN Ia also supports the SD model. Observations of remnants also offer support for Chandrasekhar-mass explosions, including wind-blown shells in RCW 86 (Williams et al. 2011) and shocked circumstellar material/bubble in the *Kepler* remnant (Chiotellis et al. 2012; Burkey et al. 2013). Altogether, there is substantial evidence that suggests that the SD channel plays a role in at least some of the observed SNe Ia (Baron 2014).

The sub-Chandrasekhar-mass model does not have the population synthesis arguments working against it, and we know that low-mass WDs in binary systems exist. Systems for which it is believed that they will evolve to an explosion have been observed (Kilic et al. 2014), potential events have been identified (Geier et al. 2013; Inserra et al. 2015), and the Type Iax subclass of SNe Ia (Foley et al. 2013; Wang et al. 2013) has been suggested as consisting of sub-Chandrasekhar-mass events themselves.

Observational evidence also supports the DD progenitor system, and the scenario is increasingly seen as the likely progenitor of some events. SN 2011fe has been intensely observed and does not show features in its spectra that would be expected if there were a normal stellar companion (Graham et al. 2015), suggesting a DD system. Super-Chandrasekhar-mass explosions like SN 2007if (Scalzo et al. 2010; Yuan et al. 2010) and SNLS 03D3bb (Howell et al. 2006) also suggest mergers. There are also many population synthesis arguments in favor of mergers as well (see Maoz et al. 2014, for a review).

1.1. The Chandrasekhar-mass SD Scenario

In the Chandrasekhar-mass scenario, the central temperature and density of the WD increase as it accretes mass from a binary companion and approaches the limiting Chandrasekhar mass. As the mass approaches the limit, central conditions become hot enough for carbon fusion to begin (via the ^{12}C–^{12}C reaction), driving the development of convection throughout the interior of the WD (Baraffe et al. 2004; Woosley et al. 2004; Wunsch & Woosley 2004; Kuhlen et al. 2006; Nonaka et al. 2012). As the central temperature reaches $\sim 7 \times 10^8$ K, the fuel in a convective plume burns to completion before it can cool via expansion (Nomoto et al. 1984; Woosley et al. 2004), and a flame is born.

The nature of this burning, be it a supersonic detonation or subsonic deflagration, largely determines the outcome of the explosion. It has been known for some time that a purely supersonic burning front cannot explain observations because the supersonic front very rapidly incinerates the star without it having time to react and expand (Arnett et al. 1971). The lack of expansion allows most of the star to burn at high densities, which produces an excessive ^{56}Ni yield and does not match the stratified composition of observed remnants (Mazzali et al. 2008). Instead, a subsonic deflagration must ignite, which allows the outer layers of the star to expand ahead of the burning front. In this case, the density of the expanding material decreases, which leads to incomplete burning of more mass and thus increased production of intermediate-mass elements. This deflagration must accelerate via instabilities and turbulent interaction, a topic that has been explored extensively in the past (Khokhlov 1993, 1995; Bychkov & Liberman 1995; Niemeyer & Hillebrandt 1995; Khokhlov et al. 1997; Cho et al. 2003, pp. 56–98; Röpke et al. 2003, 2004; Bell et al. 2004; Zingale et al. 2005; Schmidt et al. 2006a, 2006b; Zingale & Dursi 2007; Aspden et al. 2008; Ciaraldi-Schoolmann et al. 2009, 2013; Woosley et al. 2009; Hicks & Rosner 2013; Jackson et al. 2014; Hicks 2015; Poludnenko 2015).

A deflagration alone will not produce an event of normal brightness and expansion velocity (Röpke et al. 2007). Instead, the initial deflagration must transition to a detonation after the star has expanded some in order to produce abundances and a stratified ejecta in keeping with observations (Khokhlov 1991; Hoflich et al. 1995). The physics of this "deflagration-to-detonation transition" (DDT) are not completely understood, but there has been considerable study based on mechanisms involving flame fronts in highly turbulent conditions

(Blinnikov & Khokhlov 1986; Woosley 1990; Khokhlov 1991; Hoflich et al. 1995; Höflich & Khokhlov 1996; Khokhlov et al. 1997; Niemeyer & Woosley 1997; Hoeflich et al. 1998; Niemeyer 1999; Gamezo et al. 2005; Röpke 2007; Poludnenko et al. 2011; Ciaraldi-Schoolmann et al. 2013; Poludnenko 2015). These models generally reproduce the observations under certain assumptions about the ignition (Townsley et al. 2009), but research has shown that the results are very sensitive to the details of the ignition (Plewa et al. 2004; Gamezo et al. 2005; García-Senz & Bravo 2005; Röpke et al. 2007; Jordan et al. 2008). In our simulations, we initialize a detonation once the deflagration front reaches a characteristic DDT fuel density, which controls the degree of expansion the star undergoes during the deflagration stage. The implementation details are described further in Section 3.4.

1.2. Systematic Effects

Contemporary observational campaigns typically investigate how the brightness and rates of SNe correlate to properties of the host galaxy such as mass and star formation rate (see Graur & Maoz 2013; Graur et al. 2015). Of particular interest is the delay-time distribution (DTD), the SN rate as a function of time elapsed from early, rapid star formation in the host galaxy, and how it may be used to constrain progenitor models (Hachisu et al. 2008; Bianco et al. 2011; Conley et al. 2011; Graur et al. 2011; Howell 2011; Maoz et al. 2012). See also the review by Maoz & Mannucci (2012). Very recent results indicate evolution of the UV spectrum with redshift, providing evidence for systematic effects with cosmological time (Milne et al. 2015).

Motivated by this interest in correlations between properties of the host galaxy and the brightness and rate of events, earlier incarnations of our group performed suites of simulations in the DDT scenario with a modified version the FLASH code (described below) to explore systematic effects on the brightness of an event measured by the yield of ^{56}Ni (Jackson et al. 2010; Krueger et al. 2010, 2012). The study we present here explores how explosions following from a new class of "hybrid" progenitors (Denissenkov et al. 2013b, 2015; Chen et al. 2014) compare with these previous results.

2. HYBRID PROGENITOR MODELS

Rumors that the structure and evolution of stars are a solved problem (Hansen et al. 2004) are greatly exaggerated. Recent developments obtained with the modern software instrument MESA (Paxton et al. 2011, 2013, 2015) indicate that convective boundary mixing (CBM) in the cores of super asymptotic giant branch (super-AGB) stars plays a more critical role than previously thought. There are several examples in which the inclusion of CBM improves agreement between models and observations, including that of Denissenkov et al. (2013b), which studied WD interior shell convection, and Herwig (2005) and Werner & Herwig (2006), which treated He shell burning in AGB stars. Denissenkov et al. (2013b) and Chen et al. (2014) found that in some super-AGB stars, CBM halts the progression of carbon burning into the stellar core, leaving an unburned C-rich core as large as 0.2 $M_\odot$ surrounded by an O–Ne-rich intershell region extending out to the accretion layer at the end of hydrostatic carbon burning. This effect of C-flame quenching via CBM is also confirmed by the extensive parameter study on C burning in super-AGB stars in

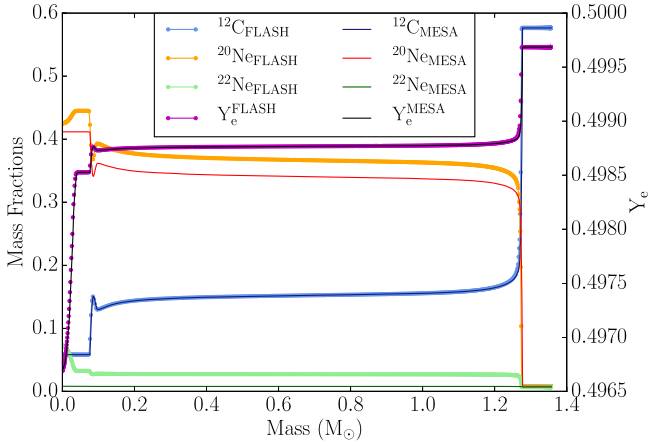

Figure 1. Abundance profile of MESA progenitor (MESA) and its reconstruction on a uniform grid at 4 km spatial resolution with the hydrostatic equilibrium condition of Equation (2) enforced (FLASH). The reduced set of nuclides are shown, where $X_{^{16}O} = 1 - X_{^{12}C} - X_{^{20}Ne} - X_{^{22}Ne}$ for the abundances labeled FLASH. Solid lines and circles denote the abundances used in FLASH, whereas plain solid lines denote the abundances used in MESA.

Farmer et al. (2015). Nevertheless, the true test of whether or not CBM is effective enough to quench the carbon flame awaits sufficiently resolved hydrodynamic simulations or further evidence via observational consequences.

Accounting for CBM, Denissenkov et al. (2015) explored the stellar evolution of a super-AGB star with initial mass of 6.9 $M_\odot$ and obtained the hybrid WD that is the focus of the present work. After hydrostatic carbon burning has ceased, the WD accretes carbon-rich material at its surface, leading to the rise of temperature near its center. This results in carbon burning in the upper layer of the small carbon-rich core, which, together with the thermal effects of the ^{23}Ne/^{23}Na Urca process, provides off-center heating (Denissenkov et al. 2015) that drives convection throughout the entire WD except the carbon-rich core.

Convection subsequently mixes the carbon-poor material in the O–Ne intershell region with carbon-rich material on the accreted layer and also partially mixes carbon-rich material from the core with the carbon-poor material in the O–Ne intershell. This proceeds along with accretion and carbon burning, until the latter yields peak temperatures near 10^9 K, around which the local heating time is shorter than the eddy turnover time so as to ignite thermonuclear runaway (Wunsch & Woosley 2004). At this point, the carbon-rich core has been significantly depleted of carbon and consists mostly of ^{16}O and ^{20}Ne, while the O–Ne intershell region has been enriched to a ^{12}C abundance of $\approx$0.14 due to convective mixing. This scenario, immediately preceding the SN Ia-like explosion, is shown in Figures 1 and 2. The process of mapping this MESA progenitor into hydrostatic equilibrium (HSE) in FLASH is described in Section 3.2.

This hybrid WD has the interesting property that its mass before the onset of accretion is 1.06 $M_\odot$, naturally closer to the Chandrasekhar limit than a traditional C–O WD. Such hybrid WD progenitors thus require less mass accretion to approach the Chandrasekhar limit, which helps to resolve one of the difficulties with the SD progenitor system (Chen et al. 2014; Denissenkov et al. 2015; Kromer et al. 2015). The mass of this hybrid WD following accretion is 1.36 $M_\odot$.

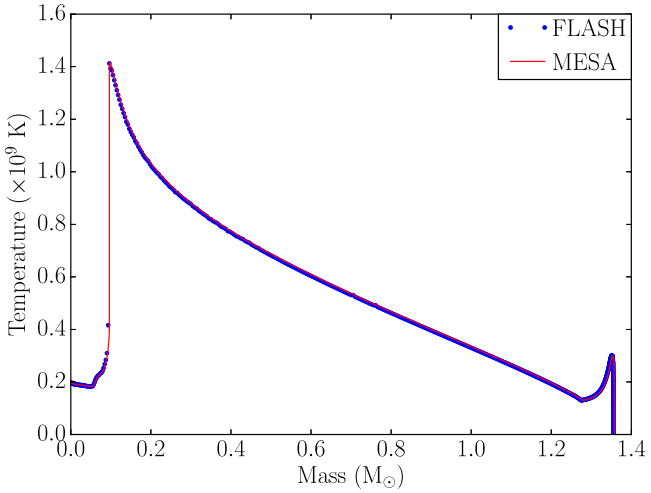

Figure 2. Temperature profile of MESA progenitor (MESA) shown with a solid red line and its reconstruction on a uniform grid at 4 km spatial resolution (FLASH) with grid zones shown in blue circles.

We note that these models include the influence of the Urca process on the convective phase of the pre-explosion progenitor. Our progenitor profiles are taken directly from MESA models presented in Denissenkov et al. (2015). These include contributions to the energy from thermal energy produced by the Urca process, but the underlying mixing length theory was not modified correspondingly. Thus, the effect on the convection is only due to the energy loss/generation rate. Our progenitor profiles are shown in Figures 1 and 2 and correspond to the models in Figure 9(a) of Denissenkov et al. (2015). In this regard, this progenitor differs from the carbon-core models of Kromer et al. (2015) in that it includes the pre-explosion convective burning phase that spreads the carbon enrichment throughout the star before ignition of the flame front. While the progenitor we study consists mostly of ^{16}O and ^{20}Ne, having the average composition of (^{12}C = 0.17, ^{16}O = 0.42, ^{20}Ne = 0.32), it differs from the O–Ne WD of Marquardt et al. (2015) by having a much higher abundance of ^{12}C due to accumulation and mixing of ^{12}C material during the accretion phase, as described above. As discussed below in Sections 3.1 and 4.2, given the temperature profile of Figure 2, this available ^{12}C is sufficient to drive both a subsonic deflagration and subsequently a supersonic detonation front as in previous work that applied the same DDT approach to C–O WD progenitors (Krueger et al. 2012).

3. METHODOLOGY

A few significant new developments in our computational methods were necessary to simulate the explosion of the hybrid C–O–Ne WD. In Section 3.1, we obtain the steady-state detonation structure for the hybrid C–O–Ne fuel and compare its detonation characteristics with those of C–O fuel to analyze the suitability of our combustion model in FLASH. Then in Section 3.2 we map the hybrid C–O–Ne WD into a uniform spatial grid to initialize FLASH while taking care to preserve HSE. We comment in Section 3.3 on our FLASH combustion model and in Section 3.4 on the DDT scheme. Finally, we describe the simulation geometry and the adaptive mesh refinement used in Section 3.5.

3.1. Modifications for C–O–Ne Burning

The combustion model in FLASH that we use for SN Ia simulations (Calder et al. 2007; Townsley et al. 2007, 2009, 2016; Seitenzahl et al. 2009; Jackson et al. 2014) separates the burning into four states: unburned fuel, C-fusion ash, a silicon-group-dominated nuclear statistical quasi-equilibrium (NSQE) state, and a full nuclear statistical equilibrium (NSE) state dominated by iron-group elements (IGEs). The progress of combustion from one of these states to the next is tracked by three scalar progress variables whose dynamics is calibrated to reproduce the timescales of reactions that convert material among these states. Previous work has focused on fuel mixtures composed principally of ^{12}C, ^{16}O, and ^{22}Ne. Simulation of the hybrid models required extension of this burning model to account for the presence of ^{20}Ne as a large abundance in the fuel. Here we describe both how ^{20}Ne is processed during combustion and the modifications made to the burning model in order to incorporate 20Ne burning.

The burning stages above are determined by the hierarchy of timescales for the consecutive consumption of C and O via fusion and Si via photodisintegration and alpha capture. Investigation of the inclusion of ^{20}Ne focused on whether an additional Ne-consumption stage would be required, and, if not, what stage should include Ne consumption. In order to characterize the physical burning sequence that we want to model, we performed a series of simulations of detonations propagating through WD material with the TORCH nuclear reaction network software (Timmes 1999, 2015).[6] TORCH is a general reaction network package capable of solving networks with up to thousands of nuclides. A mode is implemented that computes the one-dimensional spatial thermodynamic and composition structure of a steady-state planar detonation using the the Zel'dovich, von Neumann, and Döring (ZND) model (Fickett & Davis 1979; Townsley et al. 2016). We use a reaction network composed of 225 nuclides consisting of the 200 nuclides in Woosley & Weaver (1995) in addition to the 25 neutron-rich nuclides added by Calder et al. (2007) to improve coverage of electron capture processes in the Fe group.

For the multi-species fuel and ash relevant to typical WD material, the ZND detonation exhibits the stages that motivate the combustion model. Figure 3 shows these stages as they appear in a ZND detonation calculation in fuel with the fractional composition (^{12}C = 0.50, ^{16}O = 0.48, ^{22}Ne = 0.02) corresponding to the composition found in the interior of a C–O WD, and a fuel density of 10^7 g cm^{-3}. The evolution of the mass fractions in time following the passage of the shock through the zone of material is plotted below the density structure in Figure 3. The time ranges of the four states representing the burning stages are indicated by colors in the top panel of Figure 3, with the consecutive states separated by the ^{12}C–^{28}Si, ^{16}O–^{28}Si, and ^{28}Si–^{54}Fe crossing times. It can be seen that the times of the density plateaus are directly comparable to the times at which the primary energy release transitions from one fuel source to another, as, e.g., when the ^{12}C fraction has fallen to ≈1% of its initial value just before 10^{-8} s.

In our combustion models for C–O progenitors, consumption of the initial fuel is modeled as a two-step process. The two

[6] TORCH is available from http://cococubed.asu.edu, and the modified version used for this study is available from http://astronomy.ua.edu/townsley/code.

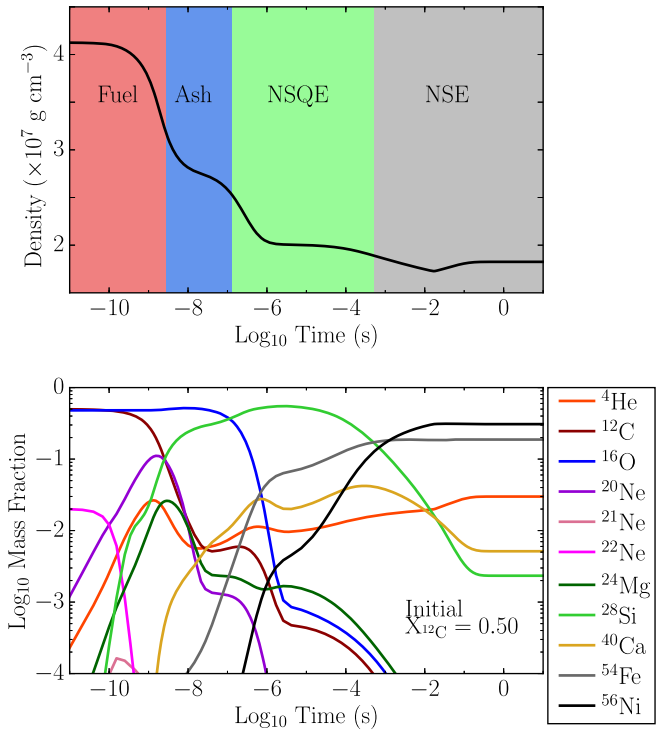

Figure 3. Density (top) and abundance (bottom) structure in the post-shock flow of a ZND detonation calculation of C–O WD material. The upper panel is shaded to show the fuel (red), ash (blue), NSQE (green), and NSE (gray) burning stages, demarcated by the ^{12}C–^{28}Si, ^{16}O–^{28}Si, and ^{28}Si–^{54}Fe crossing times. The initial composition is $X_{16_O} = 0.48$, $X_{22_{Ne}} = 0.02$, $X_{12_C} = 0.50$, and $X_{20_{Ne}} = 0.00$, and the pre-shock density is 10^7 g cm^{-3}.

stages represent the consumption first of ^{12}C, then of ^{16}O, mimicking the sequence seen in the detonation structure shown in Figure 3 for "Fuel" and "Ash" stages. At the end of this second stage the material is in a ^{28}Si-dominated NSQE state (Calder et al. 2007; Townsley et al. 2007). To determine how the burning stages change with the inclusion of ^{20}Ne, as is the case in the hybrid C–O–Ne progenitor, we perform ZND calculations with an admixture of ^{20}Ne ranging from 0.01 to 0.45, at the expense of ^{12}C content. For each composition we find the minimally overdriven solution, as was done in the C–O case. Out to the minimum in density, this solution is the same as the eigenvalue ZND solution, which corresponds to a self-supported detonation (Fickett & Davis 1979; Townsley et al. 2016). This computation gives the resolved detonation structure in C–O–Ne hybrid WD matter.

The eigenvalue detonation speeds from ZND calculations in material with ^{12}C fraction varying from 0.05 to 0.5 are shown in Figure 4, demonstrating that self-supported detonations in this progenitor are feasible with only small variation in speed across this range of ^{12}C fractions. Figure 5 shows the effect of simultaneously adding ^{20}Ne and reducing ^{12}C on the density profile. Lowering the ^{12}C fraction weakens the shock and lengthens the timescales of the step features, corresponding to more slowly burning fuel and ash, as might be expected from the lower energy release afforded by the ^{20}Ne. However, it is noteworthy that no qualitatively new features arise from the change in fuel source that would suggest that more than four representative burning stages are needed.

Qualitative similarity between C–O and C–O–Ne detonation structures is visible in the mass fractions as well. To demonstrate this, the abundance structures with initial ^{12}C

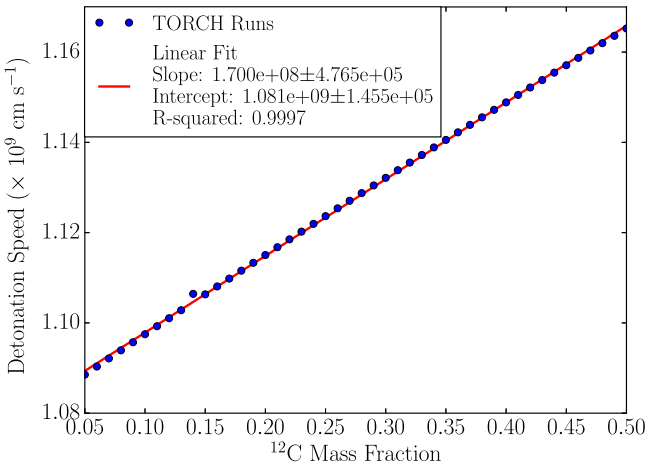

Figure 4. Self-supported detonation speed plotted vs. carbon fraction in fuel with initial (pre-shock) density of 10^7 g cm^{-3} and initial composition of $X_{16_O} = 0.48$ and $X_{22_{Ne}} = 0.02$. The sum $X_{12_C} + X_{20_{Ne}}$ is kept constant.

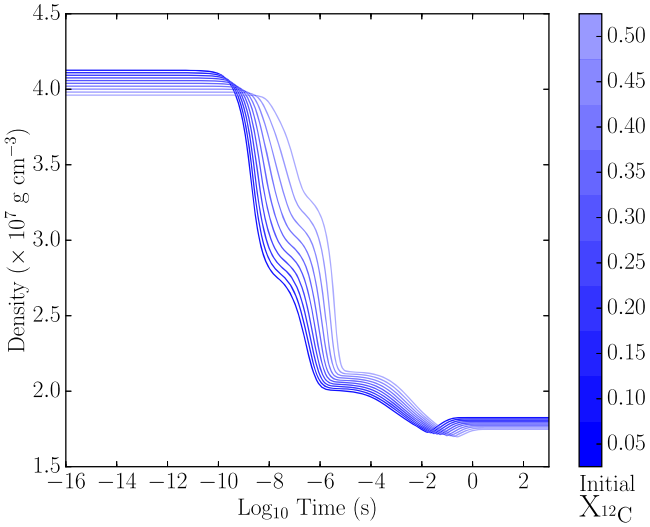

Figure 5. Density structures shaded with varying ^{12}C mass fraction, keeping constant the sum $X_{12_C} + X_{20_{Ne}}$. The rest of the composition is $X_{16_O} = 0.48$ and $X_{22_{Ne}} = 0.02$.

abundances of 0.5, 0.3, 0.15, and 0.05 are shown in Figure 6. We find that the ^{20}Ne burns simultaneously with whatever ^{12}C is present, producing primarily ^{28}Si. The Ne–C-burning stage is then followed by ^{16}O burning to silicon-group NSQE elements and then on to NSE, just as in a model with no initial ^{20}Ne, except for the progressively later ^{16}O burning time.

A graphic representation of the most significant nuclides by mass fraction and the stage in which they are important is shown in Figure 7 for an initial ^{12}C fraction of 0.15, representative of the majority of the hybrid stellar profile (see Figure 1). Nuclides are categorized based on the time at which they were maximally abundant in the network and shaded by their maximum abundance. Nuclides within the purple color palette were maximally abundant during the initial "fuel-burning" stage after the beginning of fusion and before the ^{28}Si becomes equally abundant with ^{12}C, the ^{12}C–^{28}Si crossing time t_{fa}. Blue nuclides were maximally abundant after t_{fa} but prior to the ^{16}O–^{28}Si crossing time t_{aq}, and nuclides maximally abundant after t_{aq} but before the ^{28}Si–^{54}Fe crossing time t_{qn} are plotted in green. Nuclides maximally abundant following

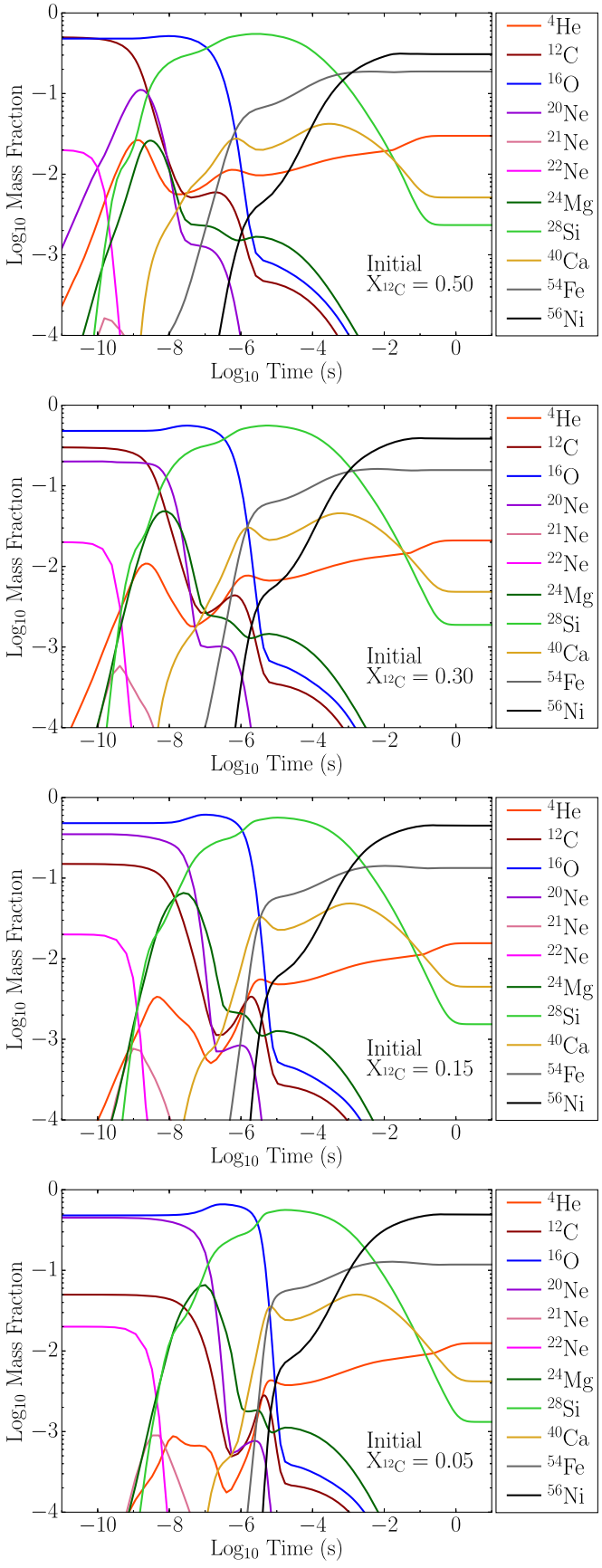

Figure 6. Mass fraction evolution for ZND detonations with varying initial ^{12}C and ^{20}Ne mass fractions, calculated for an initial density of 10^7 g cm^{-3}.

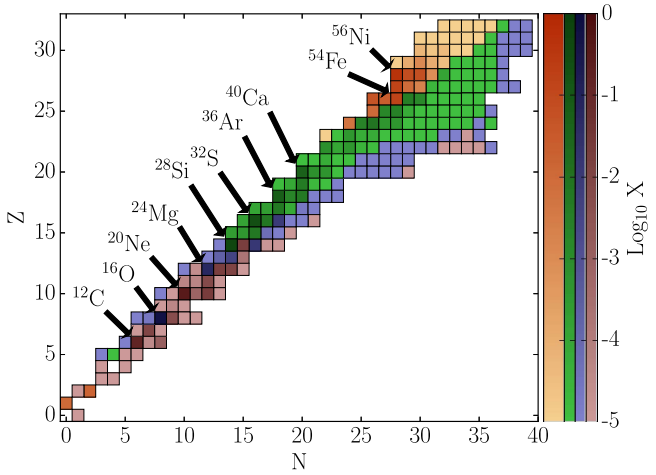

Figure 7. Our reaction network of 225 nuclides is shown, with nuclides shaded by their maximum abundance and categorized based on whether they were maximally abundant before the earliest of the following crossing times: ^{12}C–^{28}Si (purple), ^{16}O–^{28}Si (blue), ^{28}Si–^{54}Fe (green). Nuclides maximally abundant after the ^{28}Si-^{54}Fe crossing time are shown in orange. The initial composition used is $X_{^{16}\mathrm{O}} = 0.48$, $X_{^{22}\mathrm{Ne}} = 0.02$, $X_{^{12}\mathrm{C}} = 0.15$, and $X_{^{20}\mathrm{Ne}} = 0.35$.

t_{qn} are IGEs together with protons and alpha particles and are shaded in orange. Note that for the timescales we adopt the notation of Townsley et al. (2016), which describes the burning stages in detail.

The burning model we are using computes the rates for progression through the burning stages from the local temperature and the energy release from a set of major fuel abundances, previously including ^{12}C, ^{16}O, and ^{22}Ne. We have found here that any ^{20}Ne is consumed along with ^{12}C and that otherwise the burning is quite similar to that with just ^{12}C and ^{16}O as principal constituents. In consequence, the only necessary modification to our burning model is to include ^{20}Ne in the abundances of the initial state in the burning model. This accounts for the difference in binding energy of ^{20}Ne compared to ^{12}C and gives lower burning temperatures. Additionally, throughout the majority of the progenitor outside the core ignition region, due to prior convective mixing, the ^{12}C content is high enough that we will extrapolate the laminar flame speeds of Timmes & Woosley (1992) and Chamulak et al. (2008). We consider this a reasonable approximation since much of the flame propagation is dominated by Rayleigh–Taylor overturn and turbulence.

3.2. Mapping a MESA Profile to FLASH While Preserving HSE

The temperature and composition at the base of the convective zone in the hybrid C–O–Ne WD provide a natural flame initialization region for simulation of thermonuclear runaway in the DDT scenario, so we map the MESA profile into the FLASH domain, preserving its features at 4 km spatial resolution. We do this by first converting the MESA model to a uniform grid by mass-weighted averaging of quantities in MESA zones with spacing less than 4 km and using quadratic interpolation to estimate quantities where MESA zones have spacing greater than 4 km. Although our combustion model in FLASH does not evolve nuclide abundances, it uses the initial abundances of ^{12}C, ^{20}Ne, and ^{22}Ne (assuming that the rest is ^{16}O) to compute the initial mean nuclear binding energy and electron fraction. Therefore, we also represent the full set of

nuclides in the MESA profile by this reduced set of four nuclides in the uniformly gridded profile, requiring the carbon mass fractions to be identical because there is still sufficient ^{12}C in the star to sustain a detonation front. In addition, we use ^{22}Ne in the reduced set to account for the Y_e of the full set of nuclides, and we constrain ^{20}Ne and ^{16}O to be in the same ratio R in both sets of abundances. These constraints provide the following definitions for the reduced abundances used for FLASH:

$$X_{^{12}\mathrm{C}}^{\mathrm{FLASH}} = X_{^{12}\mathrm{C}}^{\mathrm{MESA}}, \tag{1a}$$

$$X_{^{22}\mathrm{Ne}}^{\mathrm{FLASH}} = 22 \times \left(\frac{1}{2} - Y_e^{\mathrm{MESA}}\right), \tag{1b}$$

$$R = X_{^{20}\mathrm{Ne}}^{\mathrm{MESA}} / X_{^{16}\mathrm{O}}^{\mathrm{MESA}}, \tag{1c}$$

$$X_{^{16}\mathrm{O}}^{\mathrm{FLASH}} = \frac{1 - X_{^{12}\mathrm{C}}^{\mathrm{FLASH}} - X_{^{22}\mathrm{Ne}}^{\mathrm{FLASH}}}{R + 1}, \tag{1d}$$

$$X_{^{20}\mathrm{Ne}}^{\mathrm{FLASH}} = R \times X_{^{16}\mathrm{O}}^{\mathrm{FLASH}}. \tag{1e}$$

Nothing constrains the resulting uniformly gridded profile to be in HSE, however, so we next construct an equilibrium profile by applying the HSE pressure constraint

$$P_{\mathrm{EOS}}(\rho_i, T_i, X_i) = \frac{g\Delta r}{2}(\rho_i + \rho_{i-1}). \tag{2}$$

Starting at the uniformly gridded profile's central density and using its temperature and composition in each zone together with the Helmholtz equation of state (EOS) of Almgren et al. (2010), we solve Equation (2) for the density in each zone. In Equation (2), Δr indicates the zone width, T_i is the temperature in zone i, X_i is the composition in zone i, and g is the gravitational acceleration at the boundary of zone i and $i-1$ due to the mass enclosed by zone $i-1$ and below. The resulting uniformly gridded equilibrium profile (FLASH) and the original profile (MESA) are shown for comparison in Figures 1 and 2. The values of the total mass before and after this procedure differ by $6 \times 10^{-3}\,M_\odot$. This procedure produced a structure that was stable in FLASH, with fluctuations in central density less than 3%, for at least 5 s with no energy deposition. Finally, we replaced the EOS routine in the public FLASH distribution with that from CASTRO (Timmes & Swesty 2000; Almgren et al. 2010) to obtain a more consistent tabulation.[7]

3.3. Combustion and Explosion Mechanisms in the FLASH Code

To simulate the explosion from either hybrid or traditional progenitor models, we use a modified version of FLASH,[8] an Eulerian adaptive mesh compressible hydrodynamics code developed by the ASC/Alliances Center for Astrophysical Thermonuclear Flashes at the University of Chicago (Fryxell et al. 2000; Calder et al. 2002). While FLASH is capable of evolving thermonuclear reaction networks coupled to the hydrodynamics, in order to treat a $\leqslant$1 cm flame front in full-star simulations of SNe Ia, we use a coarsened flame model that uses an advection-diffusion-reaction scheme to evolve a scalar variable representing the progression of burning from fuel to ash compositions as detailed in Calder et al. (2007) and Townsley et al. (2007, 2009). An additional scalar represents the burning progress from ash to intermediate-mass silicon-group elements in NSQE. A final scalar represents the burning of silicon-group elements to IGEs in NSE. The timescales for evolving these scalars are density and temperature dependent and are determined from self-heating and steady-state detonation calculations with a 200+-species nuclear reaction network (Calder et al. 2007; Townsley et al. 2016). For our evaluation of the suitability of this burning scheme for fuel with an admixture of ^{20}Ne, see Section 3.1.

The two-dimensional (2D) models we present do not utilize a subgrid-scale model for the turbulence–flame interaction (TFI). Earlier work produced subgrid-scale TFI models by extending terrestrial combustion models to consider astrophysical flames (Schmidt et al. 2006a, 2006b; Jackson et al. 2014); however, the resulting subgrid-scale models only capture TFI in three-dimensional (3D) simulations. 2D models inherently lack true turbulence, so instead we use the mimimal enhancement based on the Rayleigh–Taylor strength introduced by Townsley et al. (2007). This assumes that the TFI will self-regulate on resolved scales so that results are insensitive to the detailed treatment of the TFI. We believe this to be sufficient for 2D comparative studies like that undertaken here.

3.4. Deflagration-to-detonation Transition

This study presents simulations of the thermonuclear explosions of both a hybrid C–O–Ne WD progenitor (Denissenkov et al. 2015) and a C–O WD progenitor similar to that used in previously published suites of SN Ia simulations (Krueger et al. 2012). In both cases, we initialize the simulations with a "matchhead" consisting of a region near or at the WD's center that is fully burned to NSE. The energy release from this initial burn ignites a subsonic thermonuclear flame front that buoyantly rises and partially consumes the star while the star expands in response. As detailed in Townsley et al. (2009) and Jackson et al. (2010), in order to effect a DDT, we suppose the DDT point to be parameterizable by a fuel density ρ_{DDT} at which the subsonic flame reaches the distributed burning regime where the flame region has become sufficiently turbulent that a supersonic detonation front may arise, self-supported by the energy release from the nuclear burning proceeding behind the detonation shock front.

We thus use a similar DDT parameterization for our C–O and hybrid C–O–Ne simulations as in the C–O WD SN Ia simulations of Krueger et al. (2010, 2012) for consistency. Our choice is to ignite the detonation when a rising plume reaches the threshold density, but reality may be quite different. For example, the turbulent intensity may be greatest at the underside of a rising plume, which would imply igniting a detonation deeper in the core and possibly later, both of which would affect the yield. For purposes of this paper, which was to compare the yield from a hybrid model to a traditional C–O model, we prefer to use a simply consistent condition across cases. Jackson et al. (2010) address the dependence of the DDT density on composition separately.

Consequently, when the deflagration reaches a point where it is at $\rho_{\mathrm{DDT}} = 10^{7.2}$ g cm^{-3}, we place a region with its fuel stage (representing ^{12}C and ^{20}Ne, if present) fully burned 32 km

[7] The Helmholtz EOS table used in CASTRO is in the public BoxLib Microphysics repository at https://github.com/BoxLib-Codes/Microphysics.git (commit hash 45ed859b6c1dc80d831d93f9728986d6ad6e1ddc).

[8] FLASH is available from http://flash.uchicago.edu. Our modifications for C–O WDs are available from http://astronomy.ua.edu/townsley/code.

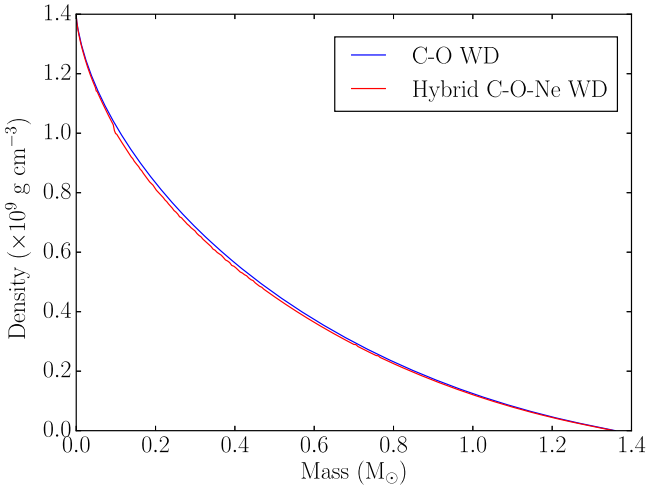

Figure 8. Density profiles of the hybrid C–O–Ne WD (red) and the reference C–O WD (blue), prepared at the same central density.

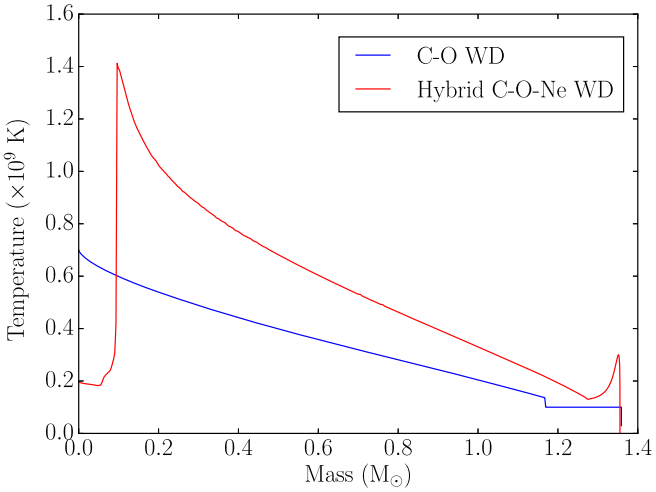

Figure 9. Temperature profiles of the hybrid C–O–Ne WD (red) and the reference C–O WD (blue).

radially outward from this point that is of size 12 km in radius. Multiple DDT points may arise, but they are constrained to be at least 200 km apart. Our choice of DDT density is slightly high in order to ensure robust ignition of a detonation shock in all cases. We note that this choice strongly influences the ^{56}Ni yield because it determines the amount of expansion of the star prior to the detonation, which determines the overall density profile (Jackson et al. 2010).

3.5. Mesh Geometry and Refinement

We performed our calculations in 2D $z - r$ cylindrical coordinates, extending radially from 0 to 65,536 km and along the axis of symmetry from −65,536 to 65,536 km. We selected a maximum refinement level corresponding to 4 km resolution using the PARAMESH adaptive mesh refinement scheme described in Fryxell et al. (2000). This resolution permitted efficiency in performing many repeated simulations with different initial conditions. The 4 km resolution was also informed by previous resolution studies in Townsley et al. (2007, 2009), which found that in 2D DDT simulations of C–O WD explosions the trends with resolution of total mass above the DDT density threshold at the DDT time are fairly robust. The amount of high-density mass at the DDT is important because it reflects the extent of neutronization during the deflagration and thus correlates with the IGE yield of the explosion. In addition, we wish to compare the hybrid IGE yields and other explosion characteristics with those of explosions from C–O WD progenitors previously explored in Krueger et al. (2012), which used 4 km resolution in FLASH with the same $z - r$ geometry we describe above. We can thus make our comparison robust by controlling for resolution and geometry factors.

4. SIMULATIONS AND RESULTS

4.1. Reference C–O WD Model

To compare the resulting features of SNe Ia produced by the hybrid model to those of previous studies of centrally ignited C–O WDs in the DDT paradigm (Krueger et al. 2010, 2012), we generate a reference C–O model. The reference model has the same central density as the hybrid model with a central temperature of 7×10^8 K, a core composition of (^{12}C = 0.4, ^{20}Ne = 0.03, ^{16}O = 0.57), and an envelope composition of (^{12}C = 0.5, ^{20}Ne = 0.02, ^{16}O = 0.48). For comparison, Figures 8 and 9 show the density and temperature profiles of the C–O and C–O–Ne hybrid WD.

We use the deflagration initialization of Krueger et al. (2012), which followed the method of Townsley et al. (2009). Townsley et al. (2009) reported that the scatter in ^{56}Ni yield from SNe Ia could be produced in a theoretical sample of SN Ia simulations from C–O WD progenitors in the DDT scenario if the evolution of the flame surface shortly following the start of deflagration is described by a deformed spherical burned region within the progenitor core. This deformation consists of a perturbation of the sphere's surface by a set of spherical harmonic functions with randomly chosen amplitudes. The theoretical SN Ia sample is formed by thus constructing a set of randomized burned geometries and then using each as the initial condition for a DDT simulation of the explosion.

We adopt this procedure to burn a spherical ignition region extending to a nominal radius of 150 km before applying a set of 35 randomly seeded amplitude perturbations, including those of Krueger et al. (2012), to ignite a suite of 35 C–O WD explosions. Finally, previous work has made the point that the explosion yield from simulations such as these may be sensitive to the initial conditions, motivating us to perform suites of 2D simulations instead of a modest number of 3D simulations (Calder et al. 2011). Although this kind of "vigorous" ignition is disfavored by convection zone ignition simulations (Nonaka et al. 2012), it appears necessary for DDT simulations to reproduce observed SNe (e.g., Seitenzahl et al. 2013; Sim et al. 2013).

4.2. Ignition Conditions for the C–O–Ne Hybrid WD

Given the temperature and composition profile of the hybrid model, if it is to undergo thermonuclear runaway, ^{12}C ignition will begin at the base of the convective zone, where temperatures are highest. This coincides with a ^{12}C abundance of ≈0.14 at a stellar radius of 350 km. Because the hybrid progenitor model was produced by the one-dimensional MESA code and has only radial dependence, a shell-like ignition region naturally results when mapping the model to a multidimensional grid. Because this scheme cannot adequately

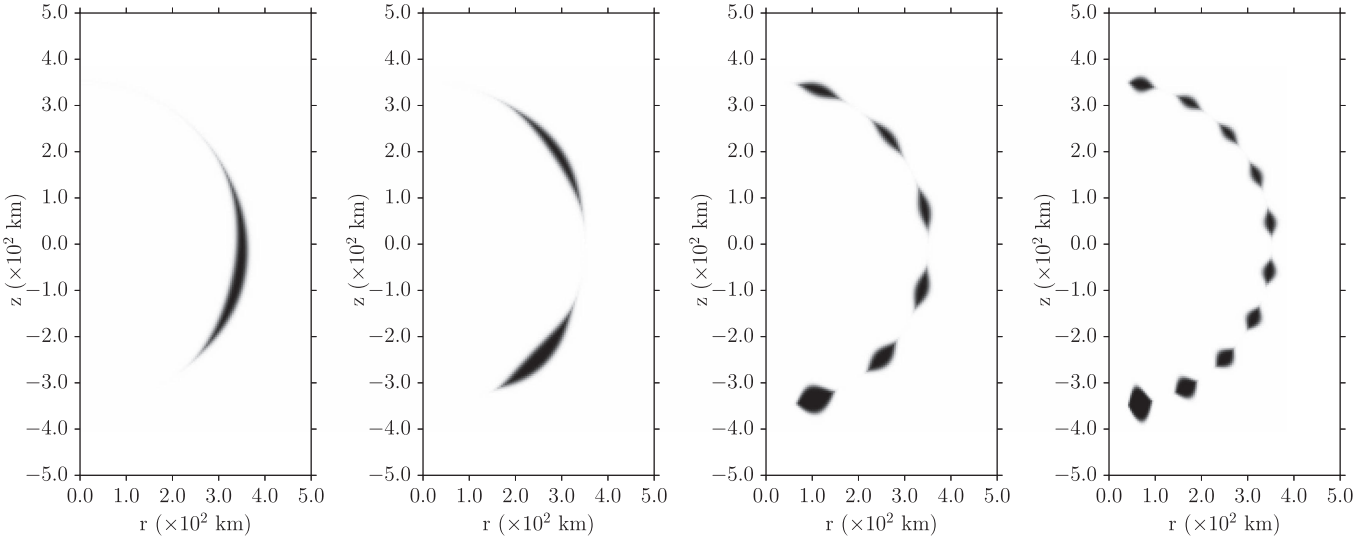

Figure 10. Distribution of initially burned mass for different choices of the harmonic number controlling the angular sinusoidal function. From left to right, the number of initially burned regions is 1, 2, 6, and 10. The harmonic number parameter is twice the number of ignition points. White denotes unburned fuel (^{12}C, ^{16}O, and ^{20}Ne), and black denotes material in NSE (IGEs and α-particles). The burned mass is located at a radial distance of 350 km, consistent with the location of maximum temperature at the base of the convective zone in the MESA profile used to initialize the FLASH simulations. For these four initial configurations, the average initially burned mass is $(6.67 \pm 0.02) \times 10^{-3}\ M_{\odot}$.

capture the effects of any low-mode, large-scale convection present in such a star, it is not clear what is the correct choice of ignition geometry for this hybrid WD model.

Lacking constraints on the exact geometry of the ignition region, we modify the ignition scheme described in Section 4.1 minimally for the hybrid progenitor by replacing the burned sphere with a thin burned shell modulated by a spherical harmonic function with variable amplitude and harmonic number, as shown in Figure 10 for different choices of the harmonic number. With this parameterization, the harmonic number controls the spatial localization and the amplitude controls the amount of initially burned mass. We therefore use our ignition parameterization to generate a suite of 35 hybrid realizations corresponding to a range of initially burned masses from $3.0 \times 10^{-3}\ M_{\odot}$ to $1.3 \times 10^{-2}\ M_{\odot}$ and a number of initial burned regions from 1 to 10. We note that our implementation of the initial conditions produced a slight asymmetry in the initially burned regions as a function of angle, as may be observed in Figure 10.

We demonstrate the influence of the number-and-amplitude parameters using the final ^{56}Ni yield as a proxy for the explosion results in Figures 11 and 12. Because we use the same ignition geometry and conditions for the C–O realizations as were used in Krueger et al. (2012), the general size of the initially burned region for the C–O realizations remains very near $0.0084\ M_{\odot}$. However, because the nature of the ignition in the C–O–Ne hybrid progenitor is unknown, we chose to sample the number-and-amplitude parameter space to provide a range of initially burned masses for comparison. In spite of the scatter in Figure 11, we performed a linear fit between the ^{56}Ni yield and initially burned mass for the C–O–Ne realizations, obtaining a slope indistinguishable from zero within uncertainties and an intercept that matches the average ^{56}Ni yield for the C–O–Ne realizations (Table 1). We also show in Figure 12 that most of the variation in ^{56}Ni yield from the C–O–Ne realizations originates from the interplay between the number of ignition regions and their size. The more ignition regions

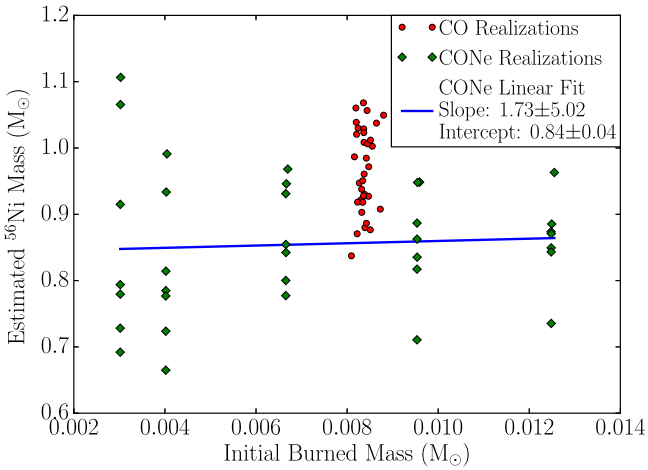

Figure 11. Dependence of the final ^{56}Ni yield on the initially burned mass at ignition for the 35 C–O (red) and 35 C–O–Ne realizations (green).

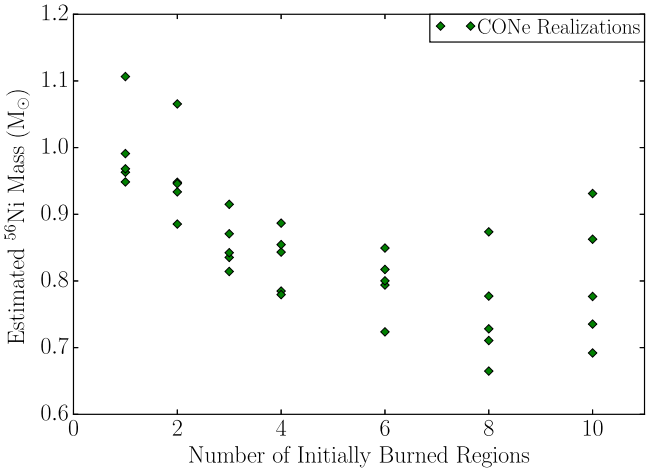

Figure 12. Dependence of the final ^{56}Ni yield on the distribution of the initially burned mass at ignition for the 35 C–O–Ne realizations.

Table 1
Average Yields and Kinetic Energy

Progenitor Type	^{56}Ni ($M_\odot$)	IGE ($M_\odot$)	Kinetic Energy ($\times 10^{51}$ ergs)
C–O	0.97 ± 0.06	1.12 ± 0.07	1.39 ± 0.05
C–O–Ne	0.86 ± 0.10	0.98 ± 0.11	1.06 ± 0.10

that are used, the greater effect the variation on their size has on the spread in ^{56}Ni yields.

Using these parameters to vary the initial burned mass and its distribution within the progenitor, we evaluate the effect of this parameterization on the estimated ^{56}Ni yield, IGE yield, binding energy, and other explosion properties in the following section.

4.3. Characteristics of Explosions from C–O and C–O–Ne WD Models

We simulate the explosions of the hybrid and C–O realizations through the end of the detonation phase and compare their features in Figures 13, 14, and 16–20 below. We compare the ^{56}Ni yields in the C–O and hybrid models, estimated from Y_e and the NSE progress variable, by assuming that the composition in NSE is ^{56}Ni plus equal parts ^{54}Fe and ^{58}Ni, as described in Townsley et al. (2009) and Meakin et al. (2009).

Production of ^{56}Ni is comparable between the C–O and hybrid cases (Figure 13), with the full range of values from each suite of simulations shown in the shaded regions and the mean values shown by solid curves. The DDT event can be distinguished in the ^{56}Ni evolution by the sharp increase in the rate of ^{56}Ni production around 1.5 s that rapidly yields over 0.5 $M_\odot$ of ^{56}Ni. While the C–O cases show a wider variation in the time at which the DDT occurs, these also have a narrower spread in final ^{56}Ni mass relative to the hybrid models. The hybrid models also tend to produce more ^{56}Ni in the deflagration phase, and some of them show a temporary plateau in ^{56}Ni production between 1.5 and 2 s. The same feature is also evident in the binding energy curves of Figure 14, computed by summing the realization's gravitational potential, internal, and kinetic energies.

This feature is a peculiarity of the off-center ignition in the hybrid models that is absent in the C–O cases and results from the relatively ^{12}C-poor, cooler core region burning about 0.25 s after the detonation front has swept through the rest of the star. This delayed burning is shown in Figure 15, which demonstrates the progression of the detonation front into the core. Although a feature evolving over so short a time this early in the explosion will likely not be visible in the SN light curves, the delayed contribution of the core to ^{56}Ni production may modify the ^{56}Ni distribution in space and velocity, potentially yielding spectral differences compared to nondelayed hybrid as well as C–O WD explosions.

The dynamical qualities of the explosion shown in the binding energy curves of Figure 14 indicate that the time distribution of unbinding is narrower for the hybrid models than for the C–O models, though the hybrid models have a wider distribution of final binding energies in all cases lower than the binding energies of the C–O models within 1 s of becoming unbound. This should correlate to a lower expansion velocity of the ejecta and thus slower cooling and delayed

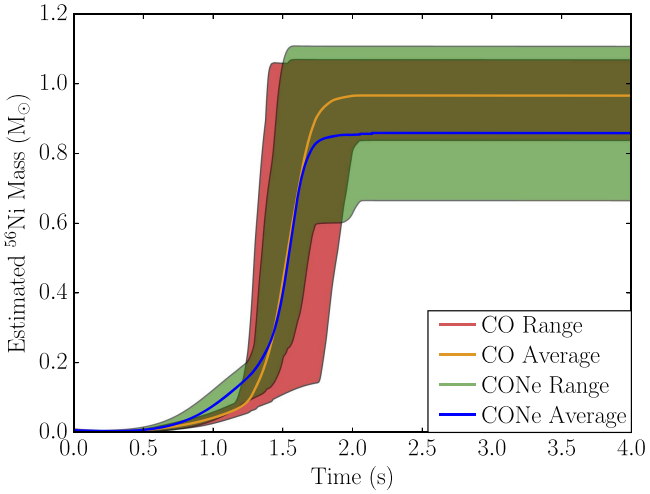

Figure 13. Evolution of the estimated ^{56}Ni yields for C–O and hybrid C–O–Ne WD realizations. The time-averaged value among C–O realizations is shown in yellow, with the full range of values at any point in time for the C–O realizations shown in red. Likewise, the time-averaged value among C–O–Ne realizations is shown in blue and their range of values shown in green.

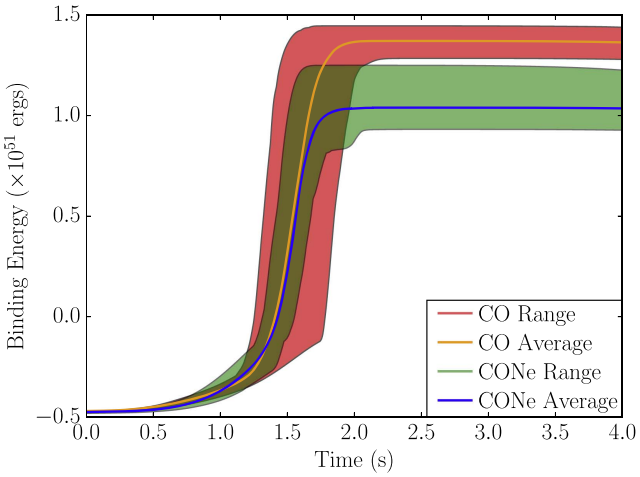

Figure 14. Evolution of the binding energy for C–O and hybrid C–O–Ne WD realizations. The time-averaged value among C–O realizations is shown in yellow, with the full range of values at any point in time for the C–O realizations shown in red. Likewise, the time-averaged value among C–O–Ne realizations is shown in blue and their range of values shown in green.

transparency relative to ejecta from C–O models. The binding energy curves also explain the differences in expansion the models undergo during deflagration and detonation, shown by the mass above the density threshold 2×10^7 g cm^{-3} in Figure 16. For times prior to ≈1.2 s, the C–O mass curves lie slightly lower than the average hybrid mass curve, indicative of a greater degree of expansion on average for the C–O models. However, the hybrid mass curve range encompasses that of the C–O mass curves until ≈1.4 s, reflective of the fact that until then, some hybrid realizations are more tightly bound than all the C–O realizations due to burning less mass and thus expanding less. During the detonation phase, however, the C–O models show a much wider variation in expansion than do the hybrid models in spite of having a smaller range of kinetic energies and mass burned to IGEs (Figures 14 and 20) once unbound. This is due to the C–O models demonstrating a much wider range of DDT times than the hybrid models.

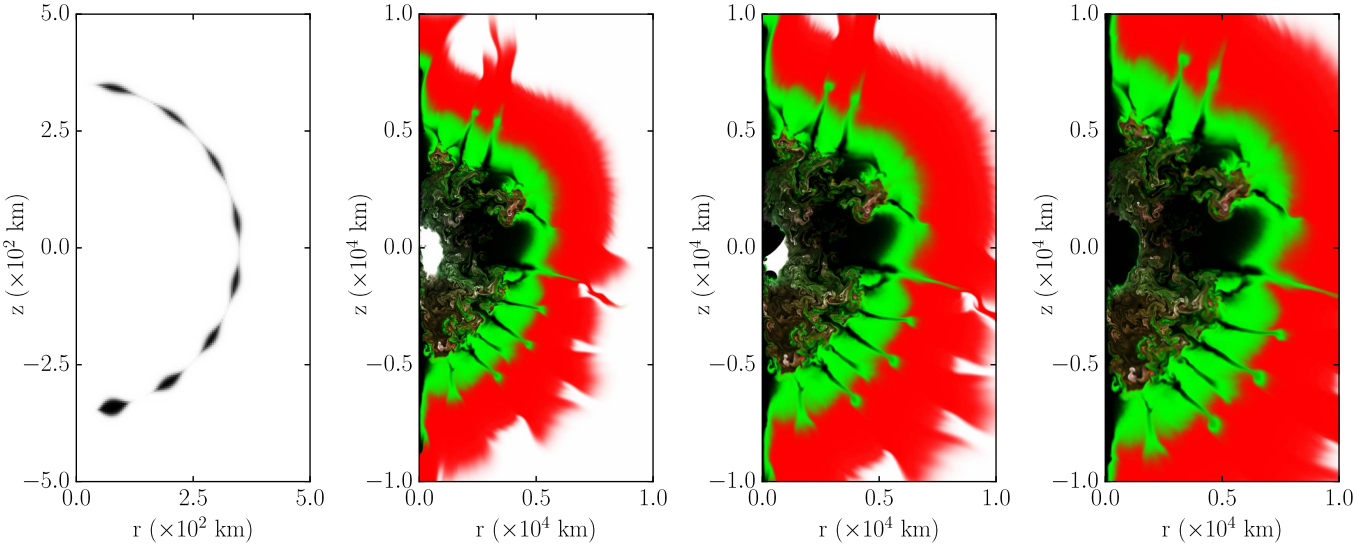

Figure 15. Progress of the burning front into the stellar core for one hybrid C–O–Ne realization, delayed relative to complete burning throughout the rest of the star. For reference, the initially burned geometry is shown at left. Material is shaded based on the reaction progress variables so that white denotes unburned fuel (^{12}C, ^{16}O, and ^{20}Ne) and red denotes ash from ^{12}C and ^{20}Ne burning. Green then denotes material in NSQE (primarily intermediate-mass silicon-group elements), and black denotes material in NSE (IGEs and α-particles). From left to right, the burning is shown at 0.0, 1.9, 2.0, and 2.1 s. The DDT time for this realization is ≈1.4 s.

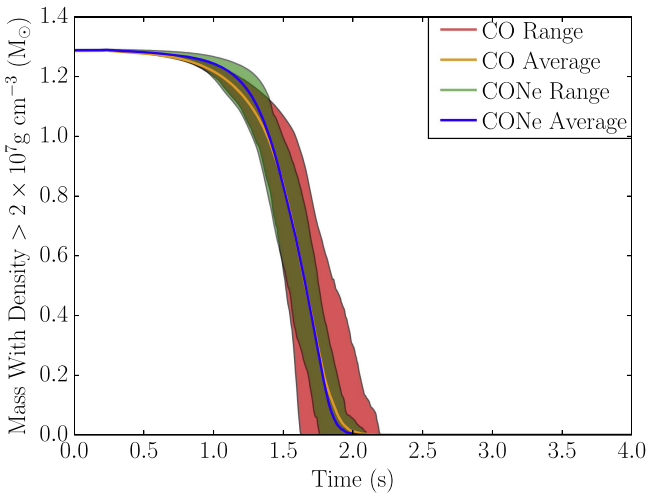

Figure 16. Evolution of the total mass having density greater than 2×10^7 g cm^{-3} for C–O and hybrid C–O–Ne WD realizations. The time-averaged value among C–O realizations is shown in yellow, with the full range of values at any point in time for the C–O realizations shown in red. Likewise, the time-averaged value among C–O–Ne realizations is shown in blue and their range of values shown in green.

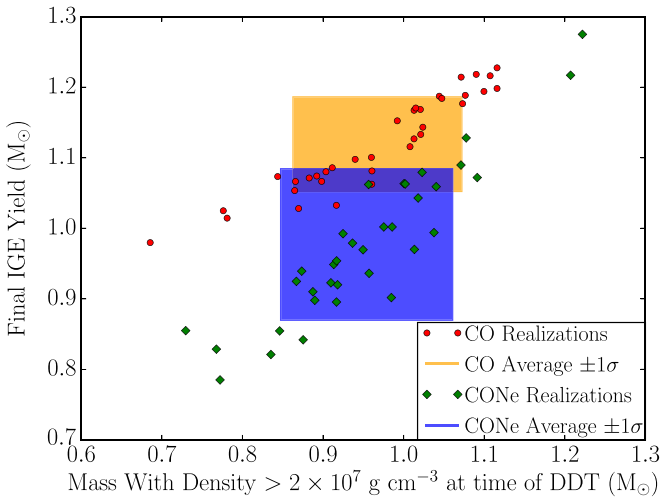

Figure 17. Final IGE yields for a range of deflagration expansion, where the degree of expansion is characterized by mass denser than 2×10^7 g cm^{-3} at the DDT time. Individual C–O (red) and C–O–Ne (green) realizations are shown, together with a rectangular area centered at their average values with size extending $\pm 1\sigma$ along each axis for C–O (yellow) and C–O–Ne (blue) groups.

Figure 17 compares the final IGE yield of the C–O and C–O–Ne models with the degree by which the models expand during the deflagration phase. The latter is characterized by the mass above 2×10^7 g cm^{-3} at the DDT time, with more high-density mass indicating less expansion during deflagration. The averages of both the C–O and C–O–Ne suites along both axes are indicated by the shaded regions with $\pm 1\sigma$ widths. The trend for both C–O and C–O–Ne models is that less expansion during the deflagration phase results in greater IGE yields, expected because low expansion results in there being more high-density fuel for the detonation to consume. In addition, both the C–O and C–O–Ne models expand over similar ranges during deflagration on average, showing that they are dynamically comparable in spite of having qualitatively different deflagration ignition geometries. Furthermore, for similar deflagration expansion, the C–O models tend to yield consistently greater IGE mass, suggesting that the lower IGE yields from C–O–Ne models are not a result of these models expanding differently than the C–O models. Rather, we interpret this disparity as indicating that the lower IGE yield in C–O–Ne models results from their lower ^{12}C abundance and the fact that given similar fuel density, their ^{20}Ne-rich fuel will burn to cooler temperatures than fuel in the C–O models. This in turn will result in slower burning to IGEs and thus a lower IGE yield.

The estimated ^{56}Ni yields are shown in Figure 18 across the range of masses burned to IGEs for all C–O and C–O–Ne realizations at 4.0 s simulation time, at which point the total mass burned to ^{56}Ni had become constant (see Figure 13). For comparable masses burned to IGEs, the hybrid models tend to

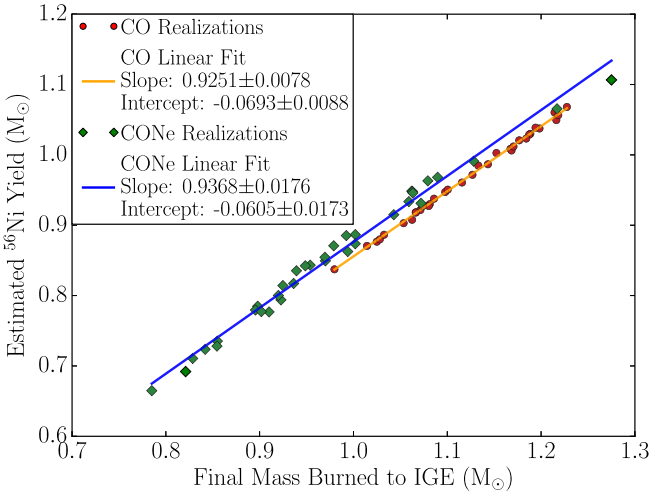

Figure 18. Production of ^{56}Ni and mass burned to IGEs for C–O (red) and hybrid C–O–Ne (green) WD realizations. To estimate the overall fraction for each case, a linear fit is shown for C–O (yellow) and C–O–Ne (blue) realizations.

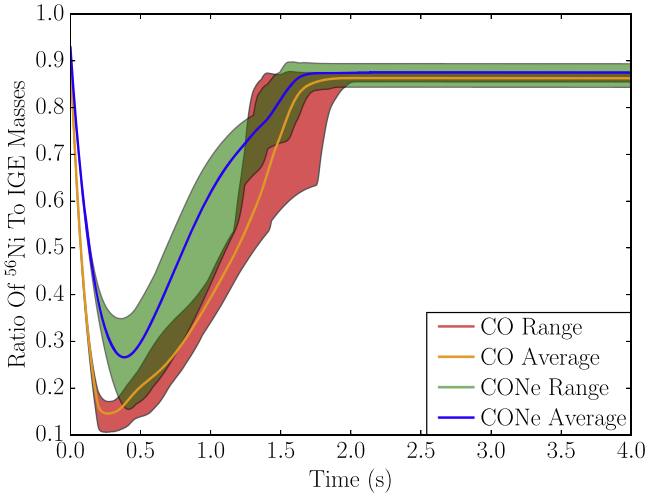

Figure 19. Estimated fraction by mass of IGE material producing ^{56}Ni evolving in time for C–O and hybrid C–O–Ne WD realizations. The time-averaged value among C–O realizations is shown in yellow, with the full range of values at any point in time for the C–O realizations shown in red. Likewise, the time-averaged value among C–O–Ne realizations is shown in blue and their range of values is shown in green.

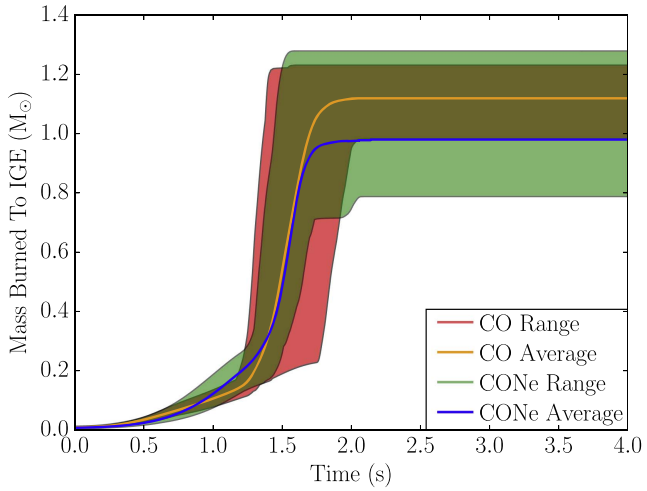

Figure 20. Mass burned to IGEs for C–O and hybrid C–O–Ne WD realizations evolving in time. The time-averaged value among C–O realizations is shown in yellow, with the full range of values at any point in time for the C–O realizations shown in red. Likewise, the time-averaged value among C–O–Ne realizations is shown in blue and their range of values shown in green.

consistently produce slightly more ^{56}Ni than the C–O models, although the ratio of IGE mass producing ^{56}Ni given by the slope is the same in both cases, within the fit error. The reason for this trend is evident from Figure 19, which shows the fraction by mass of IGE material producing ^{56}Ni evolving in time, and Figure 20, which shows the concurrent evolution of mass burned to IGE. During the deflagration phase, the C–O–Ne models on average burn more material to IGEs and also had a significantly higher fraction of IGE material producing ^{56}Ni, yielding more ^{56}Ni than the C–O models. This may be due to greater neutronization in the early deflagration of the C–O models, which are ignited closer to the center and thus at slightly higher density than the initial deflagration of the C–O–Ne models. However, during the subsequent detonation phase, the C–O models on average burn more mass to IGE while maintaining a ^{56}Ni/IGE fraction very similar to that of the C–O–Ne models, yielding significantly more ^{56}Ni by the end of the detonation phase. For reference, Table 1 summarizes the average values of ^{56}Ni yield, IGE yield, and final kinetic energy for the 35 C–O and 35 C–O–Ne realizations with one standard deviation uncertainties.

5. CONCLUSIONS

Our simulations of thermonuclear (Type Ia) SNe from both hybrid C–O–Ne and reference C–O WD progenitors using the DDT paradigm have shown that on average the hybrid progenitors yield 0.1 $M_\odot$ less ^{56}Ni than the C–O WDs. While this indicates that SNe Ia from C–O–Ne hybrids will be dimmer on average than those from C–O WDs, we also find sufficient variance in burning efficiency with the geometry of the ignition region precipitating thermonuclear runaway such that there are some hybrid progenitors that yield more ^{56}Ni than some C–O progenitors. Furthermore, we have found that not only do hybrid C–O–Ne progenitors deposit an average of 24% less kinetic energy in their ejecta than C–O progenitors but also this trend of more weakly expelled ejecta from hybrids is robust across all ignition geometries. The consistency of this result suggests that it is a consequence of the lower energy release from Ne burning compared to C burning in spite of the fact that using ^{20}Ne as an alternate fuel can still yield comparable ^{56}Ni production in some cases.

As we noted above, we found considerable variation in the ^{56}Ni production for both hybrid and traditional C–O models, and in particular, we found a much wider range of DDT times in the C–O models than the hybrid models. While in the realm of speculation, this result could follow from a greater degree of randomization in the geometry of the initially burned region for the C–O models than in the hybrids. The C–O models are initialized with an amplitude perturbation of the initially burned region composed of several angular modes, whereas the thickness of the initially burned region in each of the hybrid models is controlled by a single angular mode.

We also found that for some ignition geometries in the hybrid progenitor, a combination of off-center ignition, flame buoyancy, and composition permits their cooler core region to

delay burning until nearly 0.25 s after the detonation front has consumed the rest of the star. This result is unique to the hybrid progenitors that rely on the Urca process to provide a lower bound on the convective zone outside the core of the WD. Delayed core burning in these WDs may result in a modified ^{56}Ni distribution in their ejecta compared to ejecta from C–O WDs or even other hybrids with prompt core burning. Exploration of such effects is the subject of future work.

As our explosions from hybrid progenitors have a lower ^{56}Ni yield and hence lower brightness than traditional C–O models, the question of these events as the source of observed subluminous events, e.g., Type Iax SNe (Foley et al. 2013), arises. Our finding of an average ^{56}Ni yield of 0.1 $M_{\odot}$ less than the C–O (and the larger range of yields) indicates that explosions from these progenitors in the DDT paradigm are not subluminous and cannot on their own explain subluminous events like Type Iax SNe.

A recent study by Kromer et al. (2015) addressed pure deflagrations in near-Chandrasekhar-mass hybrid WDs as the possible progenitor systems of these faint events. The study found that most of the mass stays bound and that early epoch light curves and spectra calculated from the explosion models are consistent with observations of SN 2008ha (Foley et al. 2009). We note that comparison between our results and these is difficult for reasons besides the obvious difference of the detonation phase in our simulations. The near-Chandrasekhar-mass progenitor model of Kromer et al. (2015) is substantially different in that it is parameterized and it does not include the effects of late-time convection, or the Urca process. Also, the ignition of the deflagration is substantially different. For these reasons, there is limited utility in a direct comparison between results.

Another recent study by Bravo et al. (2016) investigated explosions from two classes of hybrid WDs, those with relatively large central C–O regions that follow from off-center C burning that stops prior to consuming the core due to neutrino cooling and those with somewhat smaller C–O cores that follow from CBM inhibiting burning. The latter "medium-sized" cores are most similar to our models as they assume similar stellar evolution.

The group performed suites of one-dimensional simulations evoking explosions via both pure detonations and DDTs and including "homogeneous" models that include the effect of mixing during C simmering prior to the ignition of the explosion. Some of the DDT models produce ^{56}Ni yields consistent with our results, but the model closest to ours (number 28) produces a yield substantially lower than our average result. This difference follows from the choice of $\rho_{\rm DDT}$ and its very different role in one dimension compared to two dimensions. DDT in two dimensions occurs at the tops of plumes, so that the degree of pre-expansion for a particular $\rho_{\rm DDT}$ is significantly less in two dimensions than in one dimension. Thus, 2D simulations produce significantly higher ^{56}Ni yields than one-dimensional simulations for a similar $\rho_{\rm DDT}$. For similar reasons, one-dimensional simulations with a higher $\rho_{\rm DDT}$ give comparable yields to 2D simulations with lower $\rho_{\rm DDT}$, leading to some cases with comparable yields.

This work was supported in part by the Department of Energy under grant DE-FG02-87ER40317. The software used in this work was in part developed by the DOE-supported ASC/Alliances Center for Astrophysical Thermonuclear Flashes at the University of Chicago. Results in this paper were obtained using the high-performance computing system at the Institute for Advanced Computational Science at Stony Brook University. The authors thank Sam Jones and Ivo Seitenzahl for fruitful discussions at the Fifty One Ergs conference, 2015 June 1–6.

REFERENCES

Almgren, A. S., Beckner, V. E., Bell, J. B., et al. 2010, ApJ, 715, 1221
Arnett, W. D., Truran, J. W., & Woosley, S. E. 1971, ApJ, 165, 87
Aspden, A. J., Bell, J. B., Day, M. S., Woosley, S. E., & Zingale, M. 2008, ApJ, 689, 1173
Baraffe, I., Heger, A., & Woosley, S. E. 2004, ApJ, 615, 378
Baron, E. 2014, NuPhA, 928, 319
Bell, J. B., Day, M. S., Rendleman, C. A., Woosley, S. E., & Zingale, M. 2004, ApJ, 608, 883
Bianco, F. B., Howell, D. A., Sullivan, M., et al. 2011, ApJ, 741, 20
Blinnikov, S. I., & Khokhlov, A. M. 1986, SvAL, 12, 131
Bravo, E., Gil-Pons, P., Gutiérrez, J. L., & Doherty, C. L. 2016, A&A, 589, A38
Burkey, M. T., Reynolds, S. P., Borkowski, K. J., & Blondin, J. M. 2013, ApJ, 764, 63
Bychkov, V., & Liberman, M. A. 1995, A&A, 302, 727
Calder, A. C., Fryxell, B., Plewa, T., et al. 2002, ApJS, 143, 201
Calder, A. C., Krueger, B. K., Jackson, A. P., et al. 2011, in Proc. SciDAC 2010, Oak Ridge http://computing.ornl.gov/workshops/scidac2010/papers/astro_a_calder.pdf
Calder, A. C., Krueger, B. K., Jackson, A. P., & Townsley, D. M. 2013, FrPhy, 8, 168
Calder, A. C., Townsley, D. M., Seitenzahl, I. R., et al. 2007, ApJ, 656, 313
Cao, Y., Kulkarni, S. R., Howell, D. A., et al. 2015, Natur, 524, 502
Chamulak, D. A., Brown, E. F., Timmes, F. X., & Dupczak, K. 2008, ApJ, 677, 160
Chen, M. C., Herwig, F., Denissenkov, P. A., & Paxton, B. 2014, MNRAS, 440, 1274
Chiotellis, A., Schure, K. M., & Vink, J. 2012, A&A, 537, A139
Cho, J., Lazarian, A., & Vishniac, E. T. 2003, LNP, 614, 56
Ciaraldi-Schoolmann, F., Schmidt, W., Niemeyer, J. C., Röpke, F. K., & Hillebrandt, W. 2009, ApJ, 696, 1491
Ciaraldi-Schoolmann, F., Seitenzahl, I. R., & Röpke, F. K. 2013, A&A, 559, A117
Claeys, J. S. W., Pols, O. R., Izzard, R. G., Vink, J., & Verbunt, F. W. M. 2014, A&A, 563, A83
Conley, A., Guy, J., Sullivan, M., et al. 2011, ApJS, 192, 1
Denissenkov, P. A., Herwig, F., Bildsten, L., & Paxton, B. 2013a, ApJ, 762, 8
Denissenkov, P. A., Herwig, F., Truran, J. W., & Paxton, B. 2013b, ApJ, 772, 37
Denissenkov, P. A., Truran, J. W., Herwig, F., et al. 2015, MNRAS, 447, 2696
Denissenkov, P. A., Truran, J. W., Pignatari, M., et al. 2014, MNRAS, 442, 2058
Dilday, B., Howell, D. A., Cenko, S. B., et al. 2012, Sci, 337, 942
Farmer, R., Fields, C. E., & Timmes, F. X. 2015, ApJ, 807, 184
Fickett, W., & Davis, W. C. 1979, Detonation (Berkeley, CA: Univ. California Press)
Foley, R. J., Challis, P. J., Chornock, R., et al. 2013, ApJ, 767, 57
Foley, R. J., Chornock, R., Filippenko, A. V., et al. 2009, AJ, 138, 376
Fryxell, B., Olson, K., Ricker, P., et al. 2000, ApJS, 131, 273
Gamezo, V. N., Khokhlov, A. M., & Oran, E. S. 2005, ApJ, 623, 337
García-Berro, E., Ritossa, C., & Iben, I., Jr. 1997, ApJ, 485, 765
García-Senz, D., & Bravo, E. 2005, A&A, 430, 585
Geier, S., Marsh, T. R., Wang, B., et al. 2013, A&A, 554, A54
Graham, M. L., Nugent, P. E., Sullivan, M., et al. 2015, MNRAS, 454, 1948
Graur, O., Bianco, F. B., & Modjaz, M. 2015, MNRAS, 450, 905
Graur, O., & Maoz, D. 2013, MNRAS, 430, 1746
Graur, O., Poznanski, D., Maoz, D., et al. 2011, MNRAS, 417, 916
Hachisu, I., Kato, M., & Nomoto, K. 2008, ApJL, 683, L127
Hachisu, I., Kato, M., & Nomoto, K. 2010, ApJL, 724, L212
Hansen, C. J., Kawaler, S. D., & Trimble, V. 2004, Stellar Interiors: Physical Principles, Structure, and Evolution (New York: Springer)
Herwig, F. 2005, ARA&A, 43, 435
Hicks, E. P. 2015, ApJ, 803, 72
Hicks, E. P., & Rosner, R. 2013, ApJ, 771, 135
Hillebrandt, W., Kromer, M., Röpke, F. K., & Ruiter, A. J. 2013, FrPhy, 8, 116
Hillebrandt, W., & Niemeyer, J. C. 2000, ARA&A, 38, 191

Hoeflich, P., Wheeler, J. C., & Thielemann, F. K. 1998, ApJ, 495, 617
Höflich, P., & Khokhlov, A. 1996, ApJ, 457, 500
Hoflich, P., Khokhlov, A. M., & Wheeler, J. C. 1995, ApJ, 444, 831
Howell, D. A. 2011, NatCo, 2, 350
Howell, D. A., Sullivan, M., Brown, E. F., et al. 2009, ApJ, 691, 661
Howell, D. A., Sullivan, M., Nugent, P. E., et al. 2006, Natur, 443, 308
Hoyle, F., & Fowler, W. A. 1960, ApJ, 132, 565
Iben, I., Jr., & Tutukov, A. V. 1984, ApJS, 54, 335
Inserra, C., Sim, S. A., Wyrzykowski, L., et al. 2015, ApJL, 799, L2
Jackson, A. P., Calder, A. C., Townsley, D. M., et al. 2010, ApJ, 720, 99
Jackson, A. P., Townsley, D. M., & Calder, A. C. 2014, ApJ, 784, 174
Jordan, G. C., IV, Fisher, R. T., Townsley, D. M., et al. 2008, ApJ, 681, 1448
Kashi, A., & Soker, N. 2011, MNRAS, 417, 1466
Khokhlov, A. 1993, ApJL, 419, L77
Khokhlov, A. M. 1991, A&A, 245, 114
Khokhlov, A. M. 1995, ApJ, 449, 695
Khokhlov, A. M., Oran, E. S., & Wheeler, J. C. 1997, ApJ, 478, 678
Kilic, M., Hermes, J. J., Gianninas, A., et al. 2014, MNRAS, 438, L26
Kromer, M., Ohlmann, S. T., Pakmor, R., et al. 2015, MNRAS, 450, 3045
Krueger, B. K., Jackson, A. P., Calder, A. C., et al. 2012, ApJ, 757, 175
Krueger, B. K., Jackson, A. P., Townsley, D. M., et al. 2010, ApJL, 719, L5
Kuhlen, M., Woosley, S. E., & Glatzmaier, G. A. 2006, ApJ, 640, 407
Leibundgut, B. 2001, ARA&A, 39, 67
Mannucci, F., Della Valle, M., & Panagia, N. 2006, MNRAS, 370, 773
Maoz, D. 2008, MNRAS, 384, 267
Maoz, D., & Mannucci, F. 2012, PASA, 29, 447
Maoz, D., Mannucci, F., & Brandt, T. D. 2012, MNRAS, 426, 3282
Maoz, D., Mannucci, F., & Nelemans, G. 2014, ARA&A, 52, 107
Marquardt, K. S., Sim, S. A., Ruiter, A. J., et al. 2015, A&A, 580, A118
Mazzali, P. A., Sauer, D. N., Pastorello, A., Benetti, S., & Hillebrandt, W. 2008, MNRAS, 386, 1897
Meakin, C. A., Seitenzahl, I., Townsley, D., et al. 2009, ApJ, 693, 1188
Meng, X., & Podsiadlowski, P. 2014, ApJL, 789, L45
Milne, P. A., Foley, R. J., Brown, P. J., & Narayan, G. 2015, ApJ, 803, 20
Nielsen, M. T. B., Dominik, C., Nelemans, G., & Voss, R. 2013, A&A, 549, A32
Niemeyer, J. C. 1999, ApJL, 523, L57
Niemeyer, J. C., & Hillebrandt, W. 1995, ApJ, 452, 769
Niemeyer, J. C., & Woosley, S. E. 1997, ApJ, 475, 740
Nomoto, K. 1980, SSRv, 27, 563
Nomoto, K., Thielemann, F.-K., & Yokoi, K. 1984, ApJ, 286, 644
Nonaka, A., Aspden, A. J., Zingale, M., et al. 2012, ApJ, 745, 73
Pakmor, R., Hachinger, S., Röpke, F. K., & Hillebrandt, W. 2011, A&A, 528, A117
Pakmor, R., Kromer, M., Taubenberger, S., et al. 2012, ApJL, 747, L10
Paxton, B., Bildsten, L., Dotter, A., et al. 2011, ApJS, 192, 3
Paxton, B., Cantiello, M., Arras, P., et al. 2013, ApJS, 208, 4
Paxton, B., Marchant, P., Schwab, J., et al. 2015, ApJS, 220, 15
Perlmutter, S., Aldering, G., Goldhaber, G., et al. 1999, ApJ, 517, 565
Phillips, M. M. 1993, ApJL, 413, L105
Plewa, T., Calder, A. C., & Lamb, D. Q. 2004, ApJL, 612, L37
Poludnenko, A. Y. 2015, PhFl, 27, 014106
Poludnenko, A. Y., Gardiner, T. A., & Oran, E. S. 2011, PhRvL, 107, 054501
Raskin, C., Timmes, F. X., Scannapieco, E., Diehl, S., & Fryer, C. 2009, MNRAS, 399, L156
Riess, A. G., Filippenko, A. V., Challis, P., et al. 1998, AJ, 116, 1009
Röpke, F. K. 2007, ApJ, 668, 1103
Röpke, F. K., Hillebrandt, W., & Niemeyer, J. C. 2004, A&A, 420, 411
Röpke, F. K., Hillebrandt, W., Schmidt, W., et al. 2007, ApJ, 668, 1132
Röpke, F. K., Niemeyer, J. C., & Hillebrandt, W. 2003, ApJ, 588, 952
Scalzo, R. A., Aldering, G., Antilogus, P., et al. 2010, ApJ, 713, 1073
Schmidt, W., Niemeyer, J. C., & Hillebrandt, W. 2006a, A&A, 450, 265
Schmidt, W., Niemeyer, J. C., Hillebrandt, W., & Röpke, F. K. 2006b, A&A, 450, 283
Seitenzahl, I. R., Ciaraldi-Schoolmann, F., Röpke, F. K., et al. 2013, MNRAS, 429, 1156
Seitenzahl, I. R., Townsley, D. M., Peng, F., & Truran, J. W. 2009, ADNDT, 95, 96
Shen, K. J., Bildsten, L., Kasen, D., & Quataert, E. 2012, ApJ, 748, 35
Silverman, J. M., Nugent, P. E., Gal-Yam, A., et al. 2013, ApJS, 207, 3
Sim, S. A., Röpke, F. K., Hillebrandt, W., et al. 2010, ApJL, 714, L52
Sim, S. A., Seitenzahl, I. R., Kromer, M., et al. 2013, MNRAS, 436, 333
Timmes, F. X. 1999, ApJS, 124, 241
Timmes, F. X. 2015, Torch Code, http://cococubed.asu.edu/, freely available
Timmes, F. X., & Swesty, F. D. 2000, ApJS, 126, 501
Timmes, F. X., & Woosley, S. E. 1992, ApJ, 396, 649
Toonen, S., Nelemans, G., & Portegies Zwart, S. 2012, A&A, 546, A70
Townsley, D. M., Calder, A. C., Asida, S. M., et al. 2007, ApJ, 668, 1118
Townsley, D. M., Jackson, A. P., Calder, A. C., et al. 2009, ApJ, 701, 1582
Townsley, D. M., Miles, B. J., Timmes, F. X., Calder, A. C., & Brown, E. F. 2016, ApJS, 225, 3
Truran, J. W., & Cameron, A. G. W. 1971, Ap&SS, 14, 179
Wang, B., Justham, S., & Han, Z. 2013, A&A, 559, A94
Wang, B., Meng, X., Liu, D.-D., Liu, Z.-W., & Han, Z. 2014, ApJL, 794, L28
Webbink, R. F. 1984, ApJ, 277, 355
Werner, K., & Herwig, F. 2006, PASP, 118, 183
Whelan, J., & Iben, I., Jr. 1973, ApJ, 186, 1007
Wijnen, T. P. G., Zorotovic, M., & Schreiber, M. R. 2015, A&A, 577, A143
Williams, B. J., Blair, W. P., Blondin, J. M., et al. 2011, ApJ, 741, 96
Woosley, S. E. 1990, in Supernovae, ed. A. G. Petschek (New York: Springer)
Woosley, S. E., Kerstein, A. R., Sankaran, V., Aspden, A. J., & Röpke, F. K. 2009, ApJ, 704, 255
Woosley, S. E., & Weaver, T. A. 1995, ApJS, 101, 181
Woosley, S. E., Weaver, T. A., & Taam, R. E. 1980, in Texas Workshop on Type I Supernovae, ed. J. C. Wheeler (Austin, TX: Univ. Texas Press), 96
Woosley, S. E., Wunsch, S., & Kuhlen, M. 2004, ApJ, 607, 921
Wunsch, S., & Woosley, S. E. 2004, ApJ, 616, 1102
Yamaguchi, H., Badenes, C., Foster, A. R., et al. 2015, ApJL, 801, L31
Yuan, F., Quimby, R. M., Wheeler, J. C., et al. 2010, ApJ, 715, 1338
Yungelson, L. R., & Livio, M. 2000, ApJ, 528, 108
Zingale, M., & Dursi, L. J. 2007, ApJ, 656, 333
Zingale, M., Woosley, S. E., Rendleman, C. A., Day, M. S., & Bell, J. B. 2005, ApJ, 632, 1021
Zorotovic, M., Schreiber, M. R., & Gänsicke, B. T. 2011, A&A, 536, A42

3 An Overview of the Convective Urca Process

3.1 The Urca Shell

We next began work on the convective Urca problem in the single-degenerate (SD), Chandrasekhar-mass progenitor model for SNIa by exploring the role of the A = 23 convective Urca process in the simmering phase of C-O WD progenitors. In the following, we detail the physics of the A = 23 Urca process as well as the main questions we intend to answer with this study. The A = 23 convective Urca process consists of electron capture (Equation 1) and beta decay (Equation 2) weak reactions which interchange ^{23}Ne and ^{23}Na nuclei and emit a steady energy flux as neutrino radiation. This energy loss to neutrinos and the associated weak reactions are rapid within the dense white dwarf core and affect the energetics of convection. In addition, an Urca shell forms in the stellar core where the electron Fermi energy is comparable to the threshold energy for electron captures, so that ^{23}Ne or ^{23}Na crossing this shell region will respectively undergo either beta decay or electron capture. The Urca shell thus retards buoyancy by increasing the ratio of nucleons to degenerate electrons below the shell, permitting higher densities there than would otherwise be possible and modifying the distribution of nuclei synthesized by carbon fusion throughout the star.

$$^{23}\mathrm{Na} + e^- \rightarrow {}^{23}\mathrm{Ne} + \nu_e \quad (1)$$

$$^{23}\mathrm{Ne} \rightarrow {}^{23}\mathrm{Na} + e^- + \bar{\nu}_e \quad (2)$$

3.2 The Convective WD Core

The main question for SNIa regards whether or not it is possible for the central convection zone in the WD to extend beyond the Urca shell. It is useful to reference the schematic of a WD core as shown in Figure 1 for this discussion. If the convective Urca process affects convection sufficiently weakly, then convection will mix material processed by ^{12}C burning into the region above the Urca shell and will mix unburned material into the core. This will give rise to a well-mixed chemical composition (except for the Urca species) both above and below the Urca shell near the time of thermonuclear runaway, which will influence the electron fraction throughout the WD and thereby the nucleosynthesis during the explosion. Conversely, a convection zone restricted to the Urca shell will stratify the composition within the WD, with ^{12}C burning products remaining below the Urca shell. In addition, a volume-restricted convection zone will evolve with a very different convective eddy turnover time than if it were allowed to extend throughout the WD. The convective eddy turnover time is an important timescale compared to the nuclear energy generation timescale within the core, and both of these may be strongly affected by the endothermic electron captures within the Urca shell. Assessing the effects of the convective Urca process is the goal of this study.

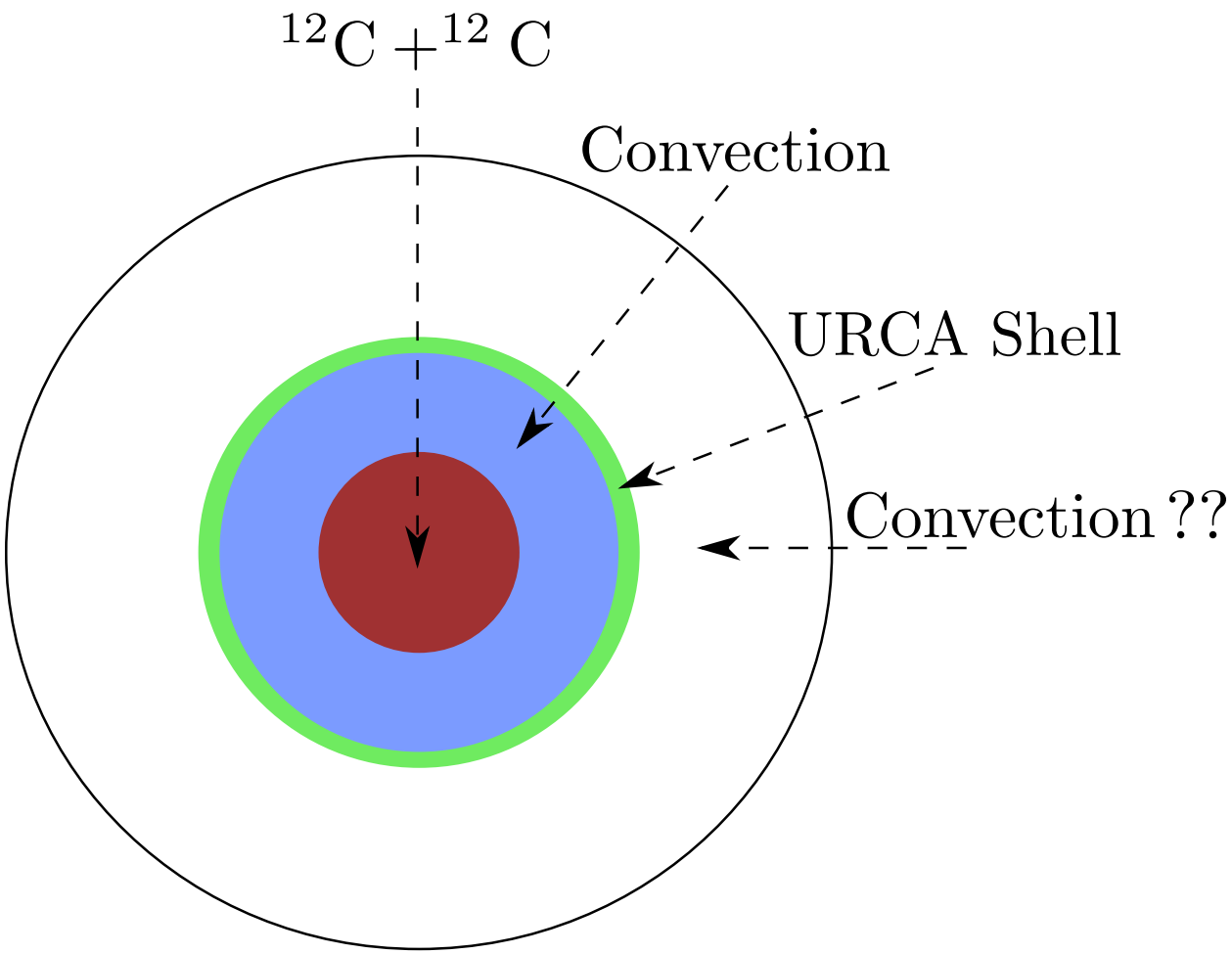

Figure 1: A schematic of a convective WD core, with the central ^{12}C burning region shown in red. The convection zone powered by ^{12}C burning is shown in blue, up to the radius of the A = 23 Urca shell, drawn in green. It is poorly understood whether the central convection zone extends past the Urca shell.

3.3 The Urca Reactions

To clarify the dynamics of the Urca reactions, we refer to Figure 2, where we illustrate the role of the electron phase space in the reactions. For an electron capture reaction with the parent nucleus ^{23}Na in excited state i, the parent removes an electron with an energy greater than the threshold energy for the capture process near the high energy side of the Fermi distribution for the degenerate electrons in the WD core. The electron capture produces the daughter nucleus ^{23}Ne in excited state j and emits an electron neutrino. The WD central density is sufficiently low that it is transparent to the neutrino, so the rate is not limited by the neutrino phase space. For the beta decay, the parent nucleus ^{23}Ne in excited state i emits an electron into the surrounding Fermi distribution of degenerate electrons, where the phase space for the decay is shown as the shaded region in the Fermi distribution. The beta decay leaves a daughter nucleus ^{23}Na in an excited state with energy j and emits an electron antineutrino, which also freely streams away from the WD.

The neutrinos emitted by these reactions only carry away energy from the WD – in the electron capture case, the neutrino energy is given by $E_\nu = E_{e^-} + E_i - E_j - |Q|$, whereas for the beta decay, the antineutrino energy is $E_{\bar{\nu}} = |Q| + E_i - E_j - E_{e^-}$. For the A = 23 Urca process, $|Q| = 4.37581$ MeV (Suzuki et al., 2016). The typical electron Fermi energy at zero temperature is given by Equation 3 of Fuller et al. (1980), who show (their Figure 1) that although the effects of finite temperature are to lower the electron chemical potential, this is not significant until several 10^9 K for WD core densities above 10^9 g cm^{-3}. Evaluating Equation 3 at several densities of interest for symmetric matter (for which the electron mean molecular weight $\mu_e = 2$, a good approximation for a C-O WD) we find the energy dependence of Figure 3. This demonstrates that at high density in the WD core, the electron chemical potential exceeds the reaction Q-value by approximately 1-2 MeV and that we can expect the electron neutrinos emitted by the electron captures of Equation 1 to carry away approximately that much more energy than electron antineutrinos emitted by beta decays of Equation 2, especially for transitions between the nuclear ground states.

$$E_F = 0.511 \text{ MeV } \times \left(\sqrt{1.02 \times 10^{-4} \left(\frac{\rho}{\mu_e} \right)^{\frac{2}{3}} + 1} - 1 \right) \tag{3}$$

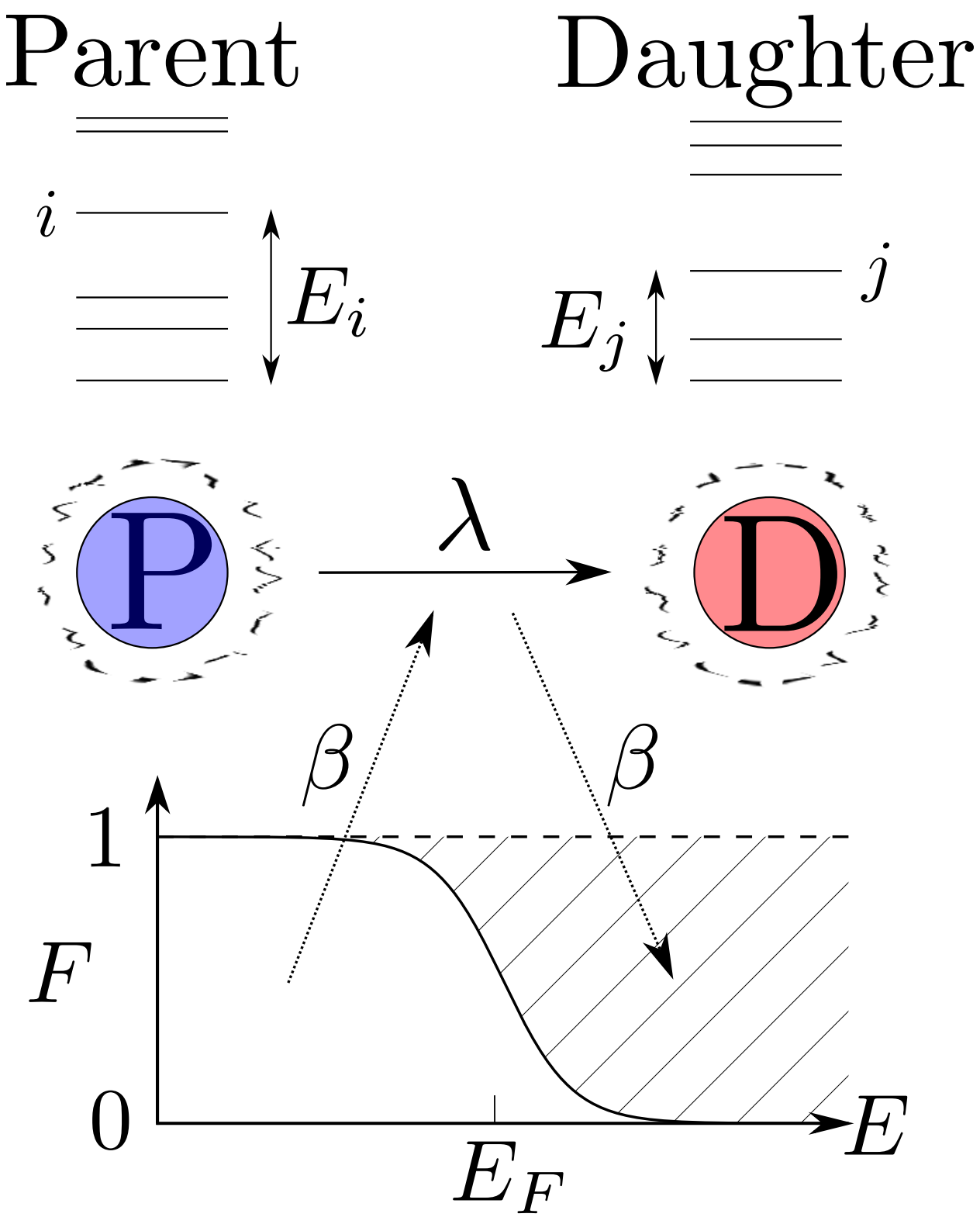

Figure 2: A schematic of the electron capture and beta decay Urca reactions, showing the parent (P) and daughter (D) nuclei together with a Fermi-Dirac distribution indicating the electron phase space for each process.

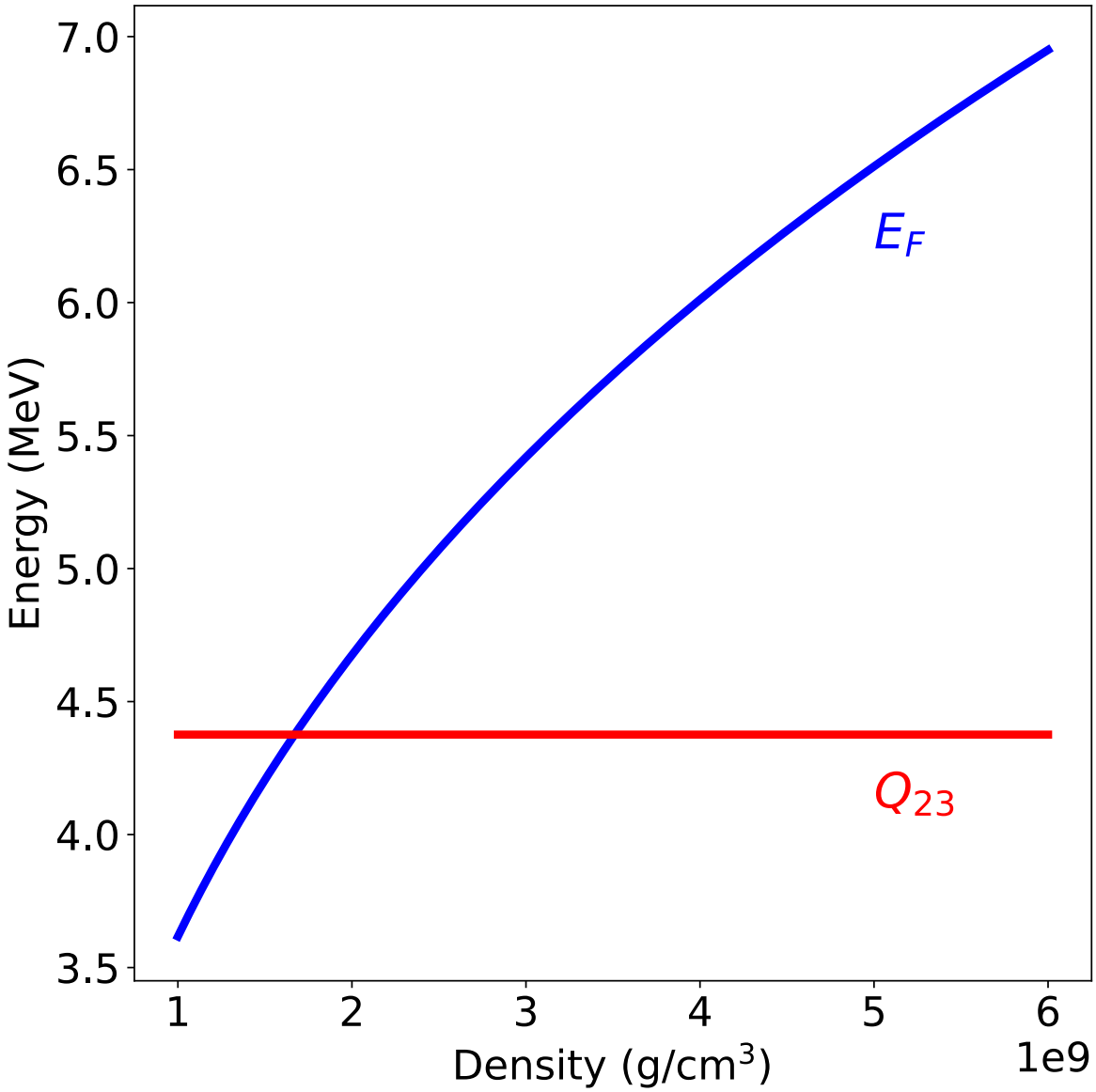

Figure 3: A plot of the electron chemical potential at zero temperature for densities comparable to the WD core densities of interest, shown in blue. Symmetric matter with $\mu_e = 2$ is assumed for convenience. The absolute Q value of the A = 23 Urca reactions is shown for comparison in red.

4 Methodology for the Convective Urca Process

In the following sections, we describe how we implemented these processes in hydrodynamics simulations of convective WD cores. We thus present the algorithmic details for the hydrodynamics code Maestro together with our microphysics implementation in the StarKiller Microphysics code. We describe our equation of state (subsection 4.2), nuclear reaction network (subsection 4.3), thermal neutrino losses (subsection 4.4), and total energy generation calculation (subsection 4.5). All of this detail is necessary to implement the physics we have described previously in section 3.

4.1 Low Mach Hydrodynamics with Maestro

This Urca work in simmering WDs is based on the use of Maestro to model low-Mach WD convection during the ^{12}C-burning simmering phase of WD evolution as originally explored by Zingale et al. (2009). That work follows a series of papers (Almgren et al., 2006a,b; Almgren et al., 2008) which present the development of the low-Mach hydrodynamics code Maestro for the study of WD convective simmering. Maestro has since been adapted for other astrophysical applications including Type I X-ray bursts (Malone et al., 2011, 2014) and convection in helium shells of sub-Chandrasekhar mass WDs in the double-detonation progenitor model for SNIa (Zingale et al., 2013; Jacobs et al., 2016).

Maestro reformulates the Euler equations to filter out acoustic waves, while accounting for the compressibility effects of stratification and energy generation. Maestro can therefore take much larger timesteps than compressible codes at low Mach numbers characteristic of convection within simmering white dwarfs because the timestep is limited only by the advective velocities, not the sound speed. We use the same velocity sponge scheme as Zingale et al. (2009) as in order to damp the velocities at low density far outside the WD core so they do not restrict the Maestro timestep.

4.2 Equation of State

We model the WD matter using the Helmholtz equation of state (EOS) of Timmes & Swesty (2000), which implements a fast table interpolation scheme that ensures the EOS remains thermodynamically consistent. This EOS treats the total pressure P as a sum of contributions from ions, photons, electrons, and positrons as in Equation 4.

$$P = P_{ions} + P_{\gamma} + P_{e^-} + P_{e^+} \tag{4}$$

All these pressure sources are treated as existing in local thermodynamic equilibrium at the local temperature. The more massive ions are non-relativistic and are treated as an ideal gas, whereas electrons and positrons have an arbitrary degree of relativity and degeneracy and are treated as non-interacting Fermi gases. We do supplement this model with Coulomb screening corrections for the ions as a result of their interactions with the background electron gas. Meanwhile, photons are treated as a Planckian blackbody as the density of WD cores is sufficiently high that the material is opaque to photons and Maestro does not track the radiation field separately.

4.3 Nuclear Reactions

For the Urca work presented here we needed to incorporate energy release from the nuclear reactions involved in ^{12}C fusion (strong force interactions) as well as the A = 23 Urca rates (weak interactions). The two primary ^{12}C burning reactions form either ^{20}Ne or ^{23}Na, and it is this ^{23}Na, together with the amount present from pollution by the stellar environment, that participates in the A = 23 Urca reactions. Each of the two-body reactions we use yield contributions to the time derivative of the molar concentrations of various species in our network as in Equation 5.

$$\frac{dY_i}{dt} = -\rho N_A \langle \sigma v \rangle_{(i,j)\to k} Y_i Y_j \tag{5}$$

The one body weak reactions, including the Urca reactions, contribute terms to the molar concentration evolution equations of the form of Equation 6.

$$\frac{dY_i}{dt} = -\lambda_{i\to j} Y_i \tag{6}$$

The full set of reactions we use for the Urca study we incorporated into the `URCA-simple` network in StarKiller Microphysics and are listed in Equation 7.

$$\begin{aligned}
^{12}\mathrm{C} + {}^{12}\mathrm{C} &\to {}^{4}\mathrm{He} + {}^{20}\mathrm{Ne} \\
^{12}\mathrm{C} + {}^{12}\mathrm{C} &\to p + {}^{23}\mathrm{Na} \\
^{12}\mathrm{C} + {}^{12}\mathrm{C} &\to n + {}^{23}\mathrm{Mg} \\
^{12}\mathrm{C} + {}^{4}\mathrm{He} &\to {}^{16}\mathrm{O} \\
n &\to p + e^- \\
^{23}\mathrm{Na} + e^- &\to {}^{23}\mathrm{Ne} \\
^{23}\mathrm{Ne} &\to {}^{23}\mathrm{Na} + e^-
\end{aligned} \tag{7}$$

The last two reactions listed in Equation 7 comprise the A = 23 Urca reactions, and we use the rate tabulations of Suzuki et al. (2016). For the remainder of the reactions in Equation 7 we use the parameterized fits of the Reaclib nuclear reaction rate database Cyburt et al. (2010) to obtain the terms $N_A \langle \sigma v \rangle_{(i,j)\to k}$ and $\lambda_{i\to j}$ in Equation 5 and Equation 6. We wrote pynucastro to construct the code implementation of this reaction network incorporating these Reaclib and Urca rates and further details on the pynucastro package are provided in section 5.

We incorporate reaction rate screening for the Reaclib rates to account for modification of the two-body interaction probability as a result of Coulomb screening by electrons in the local environment of the ions. These screening factors can speed up ^{12}C fusion by several orders of magnitude in the dense WD cores we study, and we use the screening routines provided by the StarKiller Microphysics package. These screening routines include the weak screening prescription of Dewitt et al. (1973) and the intermediate and strong screening prescription of Alastuey & Jancovici (1978). The weak Urca rates of Suzuki et al. (2016) already incorporate electron screening both for the electron chemical potential Itoh et al. (2002) and ion chemical potentials Slattery et al. (1982); Ichimaru (1993) so we do not multiply these rates by a separate screening factor.

4.4 Thermal Neutrino Losses

In addition, we calculate the energy losses from thermal neutrino reactions in the hot WD plasma using the analytic fits of Itoh et al. (1996). Because WDs such as the ones we study in this work have maximum densities of several 10^9 g cm^{-3}, the WD material is transparent to neutrinos and they freely stream out of the star and are lost. Thus the energy loss to thermal neutrinos is simply the total energy luminosity from thermal neutrino processes, listed in Equation 8.

$$\begin{aligned}
\text{recombination: } & e^-_{cont.} \rightarrow e^-_{bound} + \nu_e + \bar{\nu}_e \\
\text{pair neutrinos: } & e^+ + e^- \rightarrow \nu_e + \bar{\nu}_e \\
\text{plasma neutrinos: } & \gamma_p \rightarrow \nu_e + \bar{\nu}_e \\
\text{photoneutrinos: } & e^\pm + \gamma \rightarrow e^\pm + \nu_e + \bar{\nu}_e \\
\text{neutrino bremsstrahlung: } & e^- + (Z,A) \rightarrow e^- + (Z,A) + \nu + \bar{\nu} \\
& n + n \rightarrow n + n + \nu + \bar{\nu} \\
& n + p \rightarrow n + p + \nu + \bar{\nu}
\end{aligned} \tag{8}$$

For details about which thermal neutrino processes are dominant under varying thermodynamic conditions, see Itoh et al. (1996). We show the specific energy loss in erg g^{-1} s^{-1} in one of our simulations for a WD model initialized with central density 3.5×10^9 g cm^{-3} and central temperature 3.0×10^8 K after 460 s of evolution in Figure 4. We see that the thermal neutrino losses are spherically symmetric, which is consistent with their dependence on density and temperature and the fact that the asymmetries introduced into these quantities by convection are very small. In addition, the thermal neutrino losses peak at the core of the WD where the temperature is highest and have a maximum value of approximately 2×10^3 erg g^{-1} s^{-1}, which is several orders of magnitude lower than the typical total specific energy generation rate in the core. The energy loss rate integrated over the WD core for thermal neutrinos in the model shown in Figure 4 is approximately 3×10^{35} erg s^{-1}, significantly smaller in magnitude than the total energy generation rate of approximately -8×10^{38} erg s^{-1} integrated over the WD core. For more details on the structure of the energy generation for this model, see subsection 7.4.

4.5 Energy Generation and Losses

We calculate the nuclear energy generation rate $\dot{\epsilon}$ as the sum of the ionic binding energy contribution $\dot{\epsilon}_{\rm bind}$, the Q-value modification for the Urca rates $\dot{\epsilon}^{\rm urca}_{dQ}$, particle energy contributions for the Urca rates $\dot{\epsilon}^{\rm urca}_{\gamma,\nu,\bar{\nu}}$, and thermal neutrino energy losses $\dot{\epsilon}^{\rm thermal}_{\nu}$. To calculate $\dot{\epsilon}_{bind}$ we first compute the right hand side of the system of reaction network ODEs to obtain the rate of change for ionic molar concentrations $\dot{Y}_i$ and then use Equation 9 with n being the number of nuclear species and $m_i^{\rm ion}$ being the ionic mass of species i.

$$\dot{\epsilon}_{\rm bind} = -N_A c^2 \sum_{i=1}^{n} \dot{Y}_i m_i^{\rm ion} \tag{9}$$

The Q-value modification for the Urca rates is included because the Q value of these rates depends on the local density and temperature as a result of Coulomb corrections to the

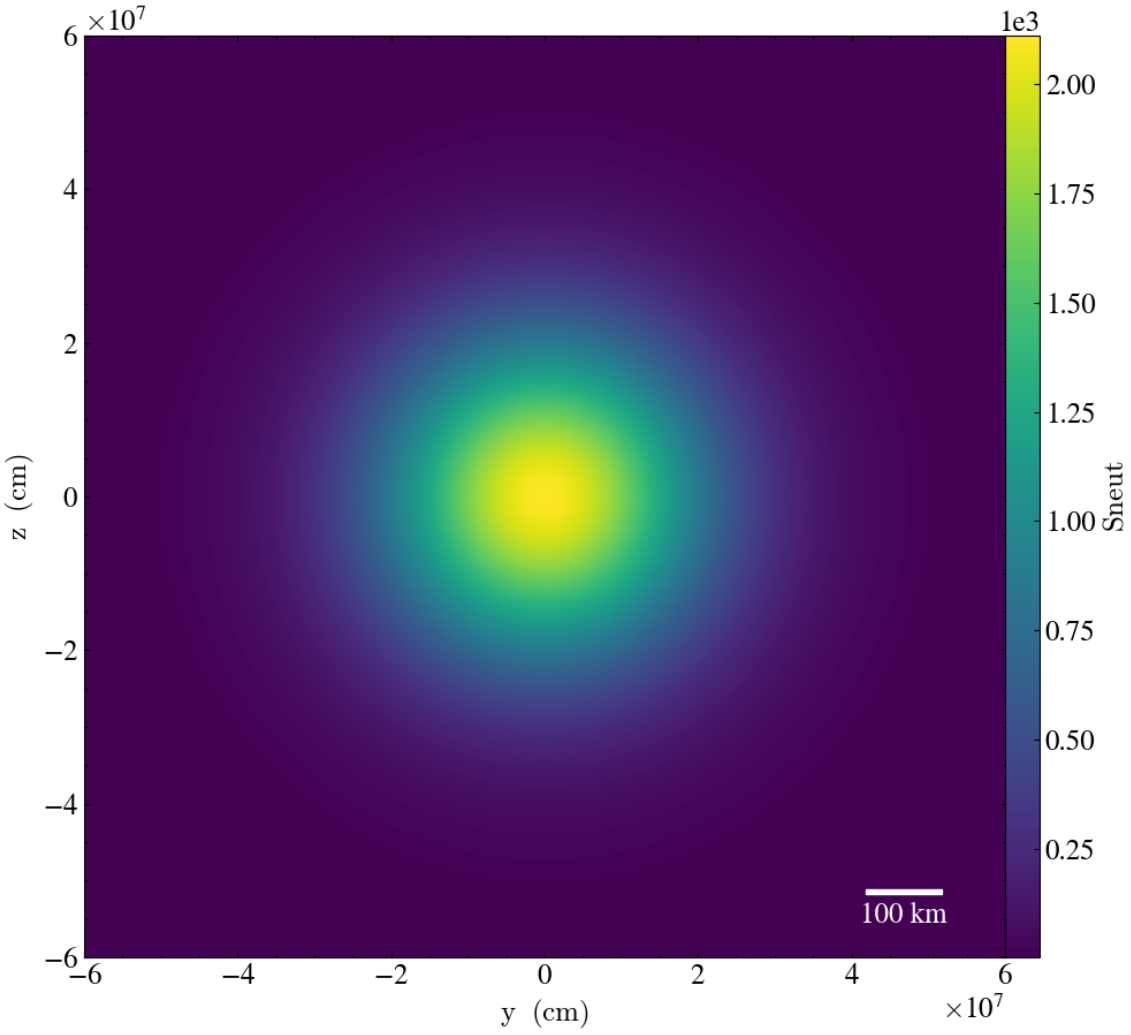

Figure 4: Slice along the x-axis in 3-D cartesian geometry at $t = 460$ s showing specific energy loss (erg g^{-1} s^{-1}) to thermal neutrino processes in the core of a WD. The central density is 3.5×10^9 g cm^{-3} and central temperature is 3.0×10^8 K.

ion chemical potentials Suzuki et al. (2016) and we compute its contribution to the energy generation as in Equation 10 where δQ is provided by the weak rate tables.

$$\dot{\epsilon}_{dQ}^{\rm urca} = N_A \sum_{i,{\rm urca}} \dot{Y}_i \delta Q_{i\rightarrow j} \tag{10}$$

Next we calculate the contributions from particle energy for the Urca rates as the sum of the γ-ray heating rates due to decays from excited final nuclear states and the (anti-)neutrino energy loss rates for these weak reactions as in Equation 11. The particle energy generation for the Urca reaction of the form $i \rightarrow j$ is denoted by $\dot{\epsilon}_{\gamma,\nu,\bar{\nu},i\rightarrow j}$ and obtained from the weak rate tables.

$$\dot{\epsilon}_{\gamma,\nu,\bar{\nu}}^{\rm urca} = N_A \sum_{i,{\rm urca}} Y_i \dot{\epsilon}_{\gamma,\nu,\bar{\nu},i\rightarrow j} \tag{11}$$

5 Pynucastro

5.1 Motivation for Pynucastro

The pynucastro code grew out of an exam problem given by Michael Zingale in his Stars course where students were to use the Reaclib nuclear reaction rate parameterizations of Cyburt et al. (2010) to implement and solve a hydrogen-burning CNO network. Seeing that there wasn't at the time a straightforward interface to build a set of reaction network ODEs from a set of Reaclib rates, Zingale wrote a python script to parse Reaclib rate files and output the ODE right hand sides in python for integration with Brown et al. (1989) provided by the scipy package of Jones et al. (2001).

When we needed to construct an Urca reaction network for StarKiller Microphysics, we adapted this into what is now pynucastro. Among other modifications, we implemented a template processing system so permit us to set up template Fortran code for a skeletal reaction network of arbitrary size and use Sympy to generate Fortran code to fill in the right hand side, Jacobian entries, and nuclear data. As a result, we were able to construct the `URCA-simple` reaction network for StarKiller Microphysics from the set of Reaclib and weak rates discussed in subsection 4.3 using only a few lines of Python as shown in Figure 5. pynucastro can also produce a graphical representation of the links between nuclei in the reaction network, and we show this for the `URCA-simple` network in Figure 6.

```
from pynucastro.networks import StarKillerNetwork

files = ["c12-c12a-ne20-cf88",
         "c12-c12n-mg23-cf88",
         "c12-c12p-na23-cf88",
         "c12-ag-o16-nac2",
         "na23--ne23-toki",
         "ne23--na23-toki",
         "n--p-wc12"]

urca_net = StarKillerNetwork(files)
urca_net.write_network()
```

Figure 5: The Python code required to construct the Urca network used for this study with pynucastro, incorporating Reaclib rates and tabulated Urca rates.

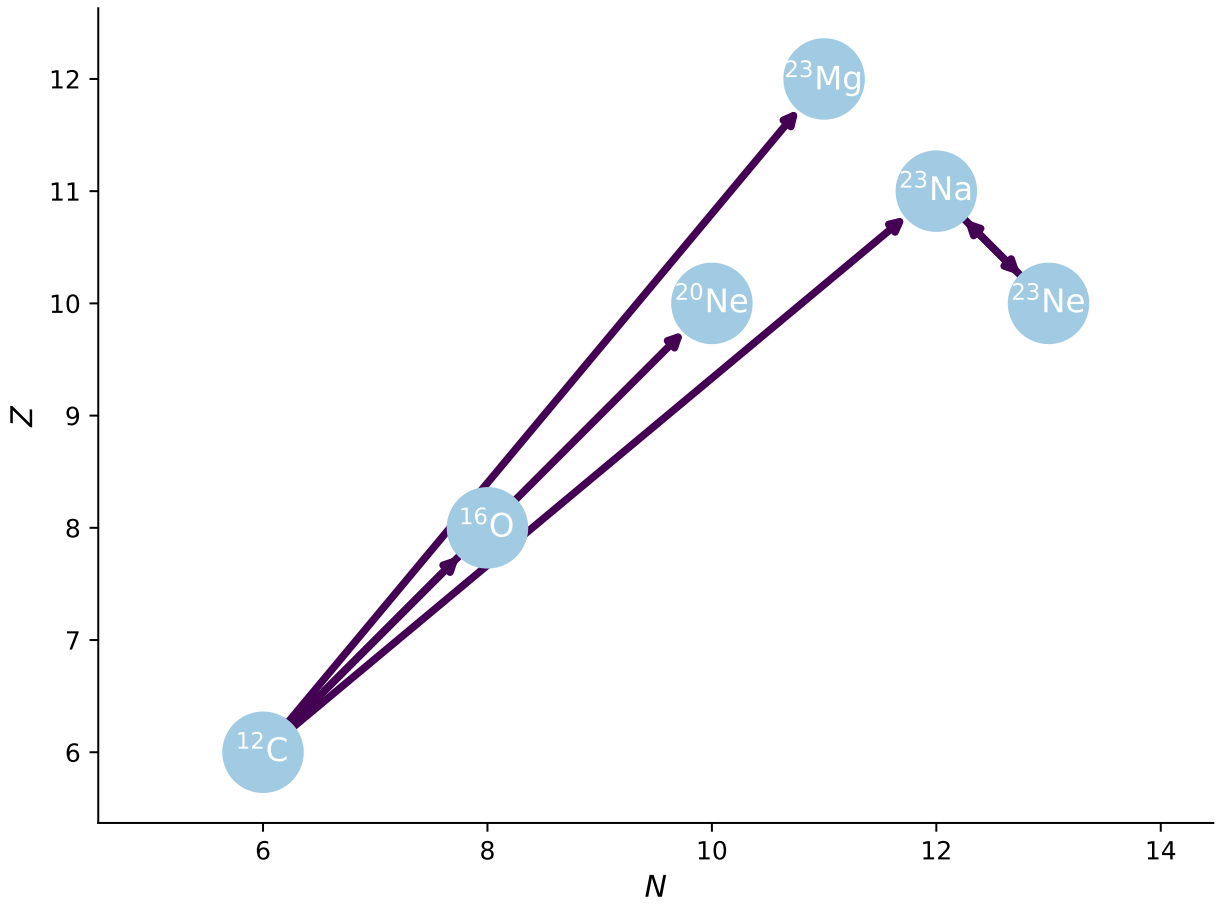

Figure 6: Graph showing links between the major nuclei in the Urca network used in this study. The network consists of ^{12}C fusion rates as well as the electron capture and beta decay reactions linking ^{23}Na and ^{23}Ne.

5.2 Overview of Pynucastro

pynucastro addresses two needs in the field of nuclear astrophysics: visual exploration of nuclear reaction rates or networks and automated code generation for integrating reaction network ODEs. pynucastro accomplishes this by interfacing with nuclear reaction rate parameterizations published by the JINA Reaclib project (Cyburt et al., 2010). Interactive exploration is enabled by a set of classes that provide methods to visualize the temperature dependency of a rate, evaluate it at a particular temperature, and find the exponent, n, for a simple T^n parameterization. From a collection of rates, the flow between the nuclei can be visualized interactively using Jupyter widgets. These features help both with designing a network for a simulation as well as for teaching nuclear astrophysics in the classroom. After selecting a set of rates for a given problem, pynucastro can construct a reaction network from those rates consisting of Python code to calculate the ODE right hand side. Generated Python right hand sides evolve species in the reaction network, and pynucastro includes a Python example integrating the CNO cycle for hydrogen burning.

pynucastro can also generate Fortran code implementing reaction networks, using SymPy (Meurer et al., 2017) to determine the system of ODEs comprising the network. From the symbolic expressions for the ODE right hand side, pynucastro also generates a routine to compute the analytic Jacobian matrix for implicit integration. Fortran networks incorporate weak, intermediate, and strong reaction rate screening for the Reaclib rates (Graboske et al., 1973; Alastuey & Jancovici, 1978; Itoh et al., 1979). These networks can also include selected weak reaction rate tabulations via Suzuki et al. (2016). To calculate energy generation in Fortran networks, pynucastro uses nuclear binding energies from the Atomic Mass Data Center (Huang et al., 2017; Wang et al., 2017) and the 2014 CODATA recommended values for the fundamental physical constants (Mohr et al., 2016).

pynucastro is capable of generating two kinds of Fortran reaction networks. The first type is a standalone network with a driver program to integrate species and energy generation using the variable-order ODE integration package VODE (Brown et al., 1989). This Fortran driver program is designed to be easy to use and can integrate reaction networks significantly faster than is possible for the generated Python networks. Secondly, pynucastro can generate a Fortran network consisting of right hand side and Jacobian modules that evolve species, temperature, and energy generation for the StarKiller Microphysics code. Via StarKiller Microphysics astrophysical simulation codes such as Castro (Almgren et al., 2010) and Maestro (Nonaka et al., 2010) can directly use pynucastro reaction networks. pynucastro includes a carbon burning network with tabulated $A = 23$ Urca weak reactions currently used for studying white dwarf convection with Maestro as presented in this dissertation.

Future work will focus on implementing nuclear partition functions to compute reverse reaction rates in the Reaclib library (Rauscher & Thielemann, 2000; Rauscher, 2003). It is also in some cases necessary to compute reverse reaction rates using detailed balance with a consistent nuclear mass model instead of using the parameterized reverse reaction rates in Reaclib (Lippuner & Roberts, 2017). Additionally, work is ongoing to port the networks generated for StarKiller Microphysics to CUDA Fortran to support parallel reaction network integration on GPU systems (Zingale et al., 2018). We intend to implement this port directly into the pynucastro-generated networks. For more information about our work porting network integration to GPUs, see Appendix A.

6 Urca Model Design and Equilibrium

6.1 Central Densities and Convective Masses

We present simulations from three central densities based on the prior work of Stein & Wheeler (2006) (3.5×10^9 g cm^{-3}) and Martínez-Rodríguez et al. (2016) (4.5×10^9 g cm^{-3}, 5.5×10^9 g cm^{-3}) for comparison. For a star undergoing the convective Urca process, convection couples closely to the nuclear energy generation rate via the weak Urca process reactions. Thus, the exact composition structure of the convective zone, and its extent as a function of central temperature, are among the features we wish to measure in this study and do not know *a priori*. Given a central density and temperature, there are several parameters we use to construct the initial radial profile for the WD model to initialize the Maestro simulations. The first of these is the mass of the central convective zone M_{conv}, which determines the mass coordinate where we transition from an isentropic (for mass coordinate $m < M_{conv}$) to an isothermal (for $m > M_{conv}$) prescription. This is intended to capture the effect of a pre-existing convection zone in enforcing isentropic conditions out to a maximum mass coordinate. In the case of central densities based on Martínez-Rodríguez et al. (2016), we are interested in determining the behavior of convection near the A = 23 Urca shell at the time central convection extends to or just beyond the A = 23 Urca shell. Because the true extent of the convection zone is unknown we used $M_{conv} = 0.5$ $M_\odot$ for our exploratory simulations based on Martínez-Rodríguez et al. (2016). For the simulations based on Stein & Wheeler (2006), we used $M_{conv} = 0.79$ $M_\odot$ which they also used as the mass boundary for the isentropic convective core in their initial WD model.

6.2 Initial Composition Structure

The second parameter we choose is, in general, the composition structure of the convection zone. This proved to have a significant impact on the total energy generation due to the sensitivity of the Urca reaction rates on the thermodynamic conditions near the Urca shell. Our first approach was simply to choose constant values of X(^{23}Na) and X(^{23}Ne) inside and outside the Urca shell threshold density with a discontinuous jump in species concentrations at the threshold density itself. This presumes that reaction rates are sufficiently rapid and strongly dependent on density to rapidly equilibrate species concentrations near the Urca shell. However, as shown in Figure 7, this yields a significant, spherically symmetric energy generation at t = 0 not driven by convection but rather by species concentrations locally not in equilibrium.

We solved this problem by changing our parameterization for the A = 23 Urca species concentrations such that in every radial grid cell the electron capture and beta decay rates for the A = 23 Urca process are equal and opposite. In reality, we cannot know the exact composition structure of the model because this is coupled to the (unknown) extent of the convective zone, so our initial model thus constructed will not reflect any such coupling. This provides an initial energy generation profile determined entirely by ^{12}C burning and thermal neutrino losses while the layer of fluid near the Urca shell is in equilibrium with respect to the species. With this method, we use as our free parameter the sum of X(^{23}Na) and X(^{23}Ne) (denoted X_{23}), set it to a constant everywhere, and solve for the combination of values that

satisfy the rate equilibrium constraint. For the models based on Martínez-Rodríguez et al. (2016) we chose X_{23} to be 5×10^{-4}, $X(^{12}C) = 0.39975$, and $X(^{16}O) = 0.59975$, similar to the values they obtain at the start of carbon simmering in their fiducial model as shown in Figures 4 and 8 of that paper. For our models based on Stein & Wheeler (2006) we choose X_{23} to be 4×10^{-4} and $X(^{12}C) = X(^{16}O) = 0.4998$ for consistency with their WD models denoted with the "S-4" prefix.

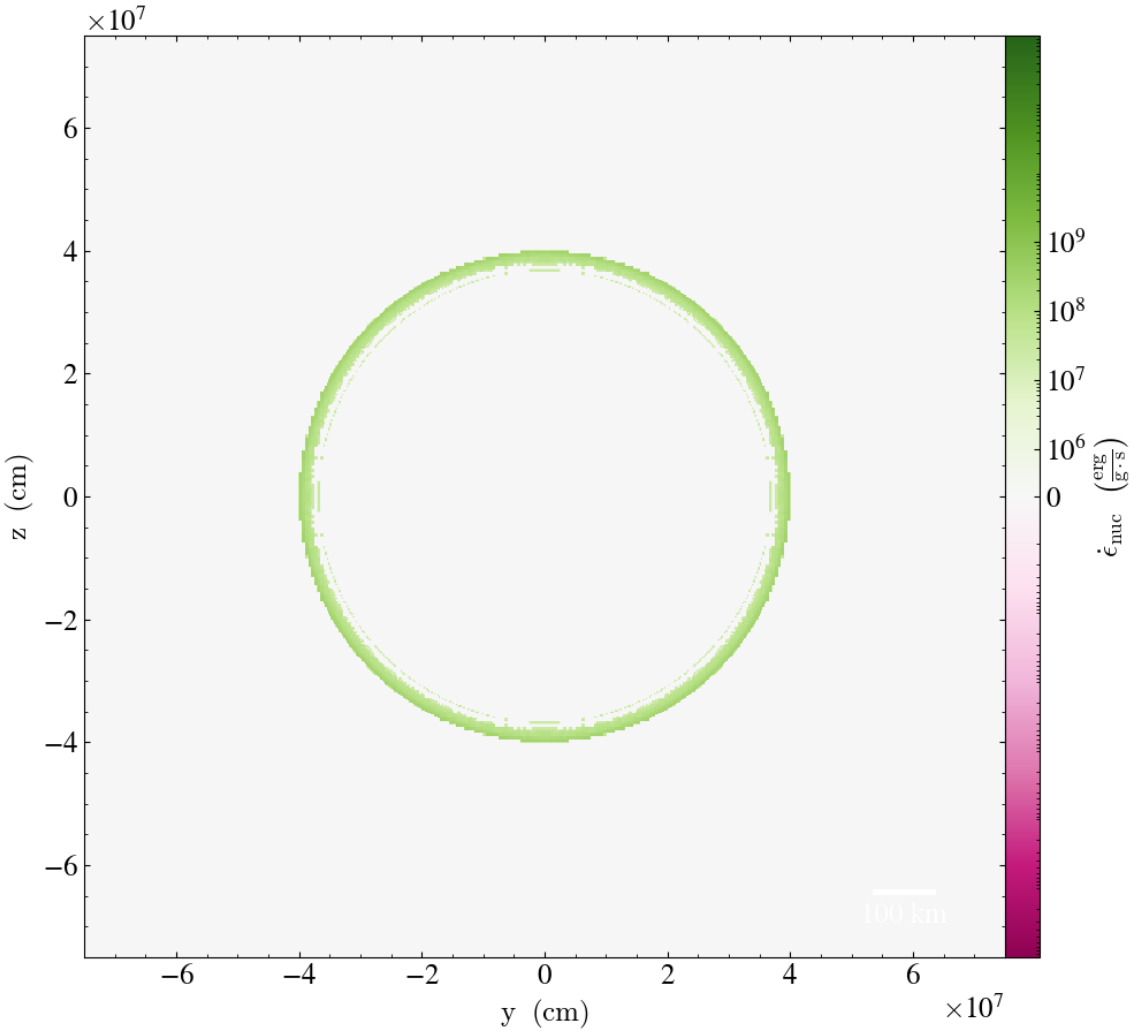

Figure 7: Slice along the x-axis in 3-D cartesian geometry at $t = 0$ showing positive (green) and negative (magenta) specific energy generation in the core of a WD. Discontinuous jump conditions are used for the A = 23 Urca species at the Urca shell, yielding a ring of material out of equilibrium near the Urca shell at initialization. The central density is 3.5×10^9 g cm^{-3} and central temperature is 3.0×10^8 K.

6.3 Initial Hydrostatic and Species Equilibrium

To construct our model WD profiles given the above parameters, we integrate the equation of hydrostatic equilibrium Equation 12 (HSE) supplemented by either an isentropic or isothermal temperature constraint. Denoting the zone for which the solution (ρ_i, T_i, X_i) is desired by the index i we write the hydrostatic equilibrium equation as

$$p_{i+1} - p_i = \frac{1}{2}\Delta r \left(\rho_{i+1} + \rho_i\right) g_{i+1/2} \tag{12}$$

and similarly denote the isentropic ($s_{i+1} = s_i$) and isothermal ($T_{i+1} = T_i$) thermodynamic constraints. The notation $g_{i+1/2}$ indicates we calculate the gravitational acceleration at the interface of zones i and $i+1$ due to the mass contained within the radius of the interface. At each zone we use an iterative procedure to solve Equation 12 together with the thermodynamic constraints appropriate given our choice of $\mathrm{M_{conv}}$ and the mass coordinate of the zone. In each iteration we construct the quantity $A = p_{i+1} - p(\rho, T)$ and, for the isentropic region, $B = s_{i+1} - s(\rho, T)$ with $p(\rho, T)$ and $s(\rho, T)$ supplied by the Helmholtz EOS described in subsection 4.2. We then use a two dimensional Taylor expansion of $A(\rho, T) = 0$ and $B(\rho, T) = 0$ to find the values of ρ, T for the next iteration. To begin each iteration we use $\rho = \rho_i$ and $T = T_i$ from the previous zone. For the isothermal case, this simplifies to a one dimensional Taylor expansion in ρ. We iterate this procedure until we satisfy the following HSE convergence criteria

$$\left| \frac{p_{i+1} - p_i}{\Delta r} - \frac{1}{2}\left(\rho_{i+1} + \rho_i\right) g_{i+1/2} \right| < \varepsilon_{HSE} \left| \frac{p_{i+1} - p_i}{\Delta r} \right| \tag{13}$$

with ε_{HSE} set as near as 1×10^{-10} as we can numerically reach (typically, 3×10^{-10}).

We supplement the preceding discussion by nesting a second iterative procedure inside the inner loop above to determine the composition vector X_i prior to calling the EOS. This consists of a series of Newton iterations to solve the following constraint equations for the mass fractions of the A = 23 Urca-active nuclei ^{23}Na and ^{23}Ne:

$$\mathrm{X}(^{23}\mathrm{Na})\lambda_{23}^{e.c.} - \mathrm{X}(^{23}\mathrm{Ne})\lambda_{23}^{\beta^-} = 0 \tag{14}$$

and

$$\mathrm{X}(^{23}\mathrm{Na}) + \mathrm{X}(^{23}\mathrm{Ne}) = \mathrm{X}_{23}. \tag{15}$$

In order to ensure the Newton iterations remain numerically well-behaved we choose X(^{23}Na) as the independent variable if the left hand side of Equation 14 is positive and X(^{23}Ne) otherwise. We repeat the Newton iterations until the left hand side of Equation 14 is below 1×10^{-10}. In Equation 14, the electron capture and beta-decay rates for the Urca reactions are respectively denoted by $\lambda_{23}^{e.c.}$ and $\lambda_{23}^{\beta^-}$ and depend on the electron fraction Y_e for each iteration of the Newton loop.

6.4 Convective Velocity Initialization

All models were initialized with a multipole convective velocity field in the interior of the WD core, where we used the multipole scheme of Zingale et al. (2009) to prevent an unphysical

thermal runaway at the start of the simulation. For example, we initialize the models with central density 4.5×10^9 g cm^{-3} and 5.5×10^9 g cm^{-3} using the multipole velocity perturbations as follows (in the notation of Zingale et al. (2009)): velocity perturbation amplitude $A = 100$ cm s^{-1}, perturbation transition width $d = 2.5$ km, perturbation radius $r_{\rm pert} = 250$ km, and spatial scale $\sigma = 250$ km. A plot of the radial velocity at initialization is shown in Figure 8, and this quickly gives rise to the convective fields discussed in the following sections. For the model with central density 3.5×10^9 g cm^{-3}, we initialized the velocity field with $A = 10^6$ cm s^{-1}, $d = 2.5$ km, $r_{\rm pert} = 200$ km, and $\sigma = 665.75$ km in order to attempt to match the actual convective field more closely.

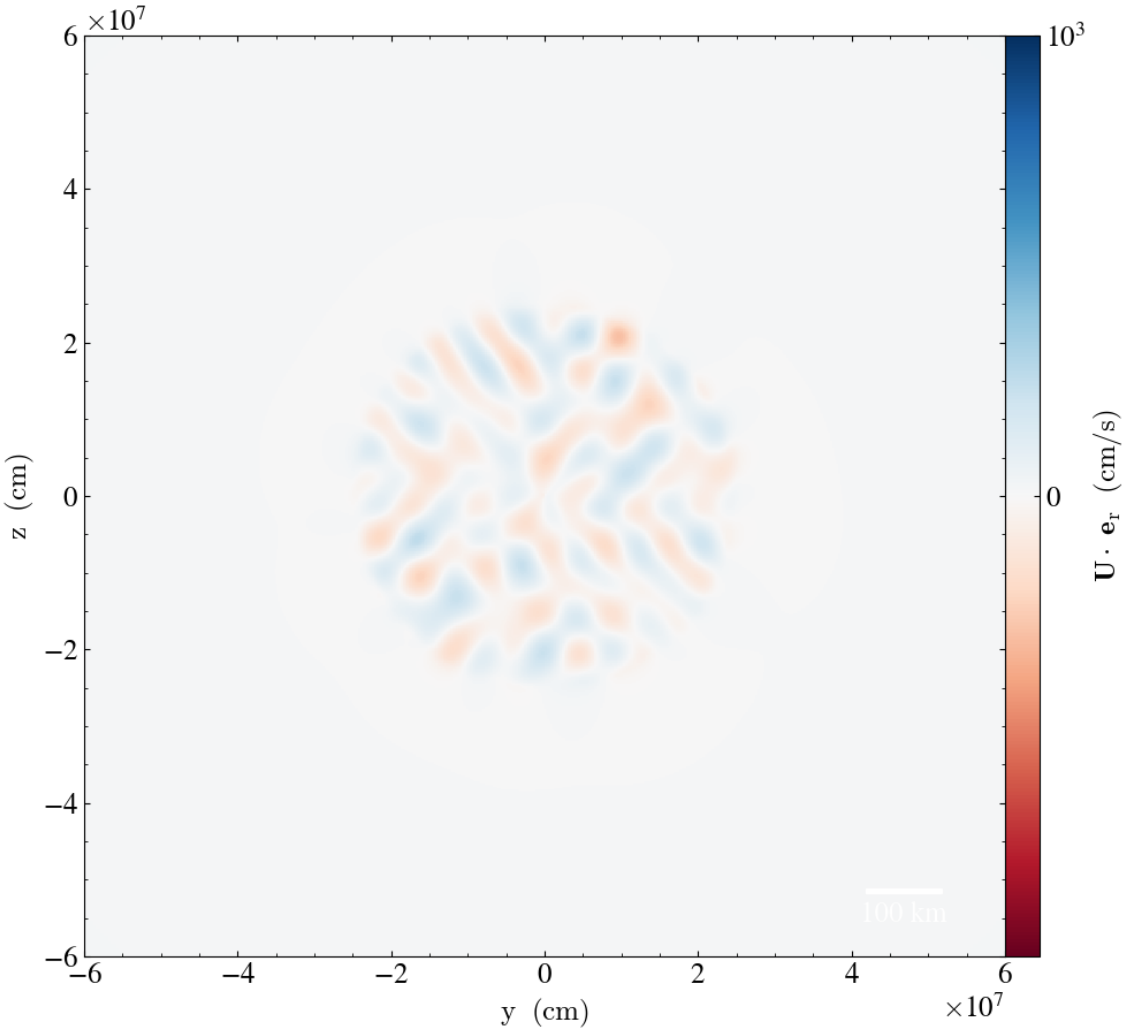

Figure 8: Slice along the x-axis in 3-D cartesian geometry at $t = 0$ s showing positive (blue) and negative (red) radial velocities in the core of a WD due to the initial velocity perturbation. The central density is 4.5×10^9 g cm^{-3} and central temperature is 5.5×10^8 K.

7 Convective Urca Simulations

7.1 Overview

In what follows we present the main results from the WD models with different central densities included in this study, using the methodology of section 4, the reaction network from section 5, and the initial model setup from section 6. As described in subsection 6.1, we choose central densities 3.5×10^9 g cm^{-3}, 4.5×10^9 g cm^{-3}, and 5.5×10^9 g cm^{-3}. All simulations were performed at a spatial resolution of 2.5 km for the region of the WD cores where the density exceeded 10^9 g cm^{-3}, less than the A = 23 Urca threshold density of approximately 1.66×10^9 g cm^{-3}, as given by Suzuki et al. (2016). Regions outside the WD cores are refined less finely, with a base spatial grid at 20 km resolution.

We ran each of these models until the initial fluctuations from the initial conditions subsided and the WD was left slowly evolving with an established convection zone. In subsection 7.2, subsection 7.3, and subsection 7.4 we show the general extent and behavior of the convection zone and energy generating regions for the central densities we explored. Because we were interested in the extent of the convection zone during early ^{12}C simmering when the convection zone interacts with the Urca shell, we did not continue these simulations up until the point of thermonuclear runaway in this study.

7.2 Central Density: 4.5×10^9 g cm^{-3}

For the model with central density 4.5×10^9 g cm^{-3} we found that to obtain strong mixing across the Urca shell due to convection, a central temperature near 5.5×10^8 K was required. We carried out a Maestro simulation with these central conditions and a spatial resolution of 2.5 km, using 3 levels of refinement for a total of 4 spatial levels. In Figure 9 we show the radial velocities after 443 s of evolution, demonstrating a developed central convection zone that extends just past 400 km in radius, the approximate location of the Urca shell. Outside this radius convection lies a region approximately 100 km thick where gravity waves excited by the underlying convective zone yield a radially oscillating pattern in the velocity field. Still further out the flow is stagnant, leading to small-scale noise in the velocity field as computed with Maestro. We believe this noise largely results from regions of the domain outside the finest level of refinement where the base state in Maestro no longer aligns with the cartesian grid. For a detailed discussion of how Maestro implements alignment and mapping between the cartesian grid and radial base state for spherical problems such as 3D WD convection, see Section 4 of Nonaka et al. (2010). Extending the finest level to cover a larger portion of the star would increase the computational cost of the simulation without adding any scientific value, as convection does not operate outside the central region shown. We therefore do not attempt to resolve these regions in our simulations.

As to the location of the Urca shell itself, we also plot the contours of zero specific energy generation rate, which form three shell-like regions. The innermost such contour corresponds to the transition from the exothermic ^{12}C burning region at the center of the WD to an endothermic region outside it where electron captures onto ^{23}Na provide local cooling. The middle such contour is in the vicinity of the A = 23 Urca shell, where the energy contributions from electron captures onto ^{23}Na balance those of beta decays from

^{23}Ne. Between the middle and outer contours, energy release is exothermic, driven by the beta decays from ^{23}Ne transported up past the Urca shell, and outside the outer contour no products of ^{12}C burning are present and no reactions occur.

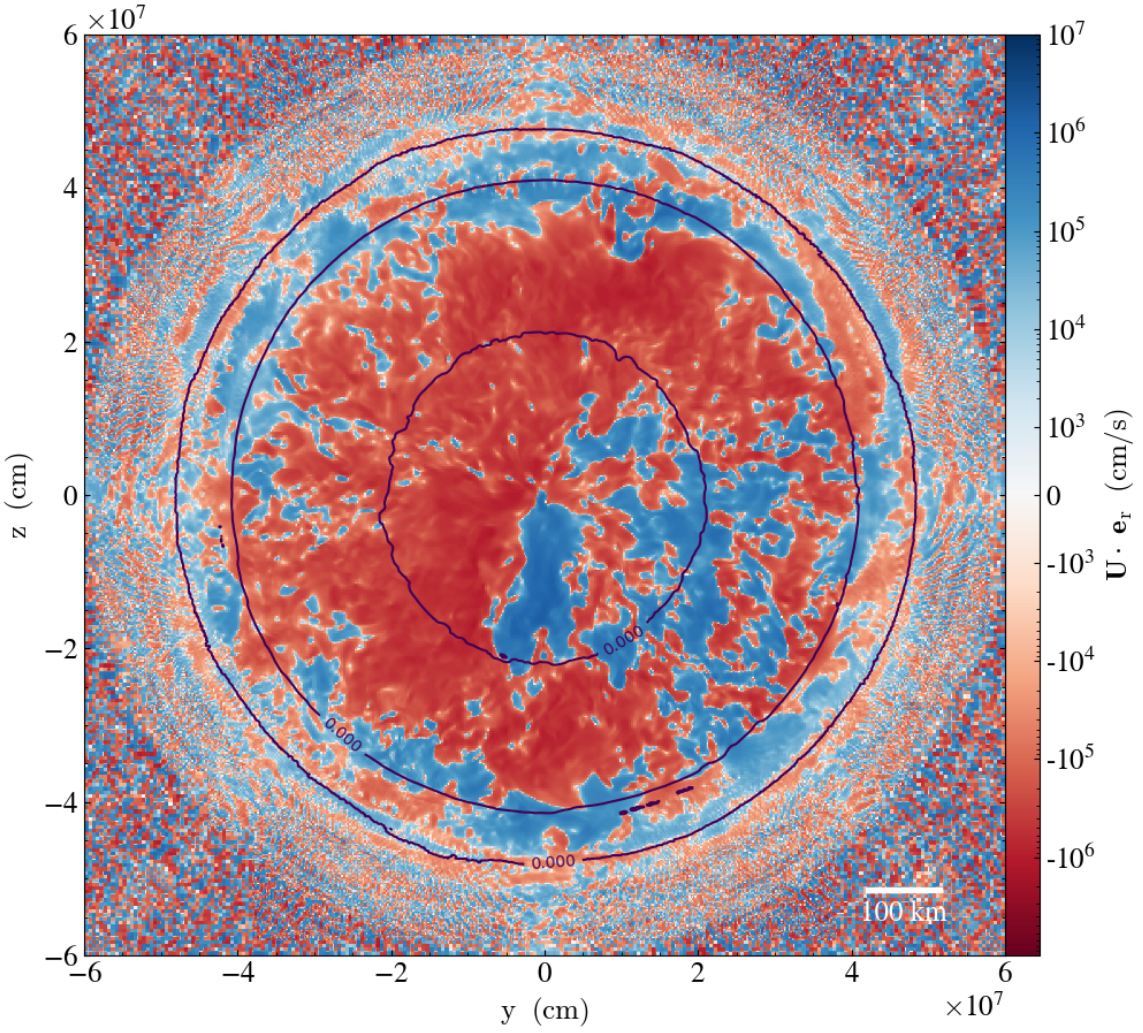

Figure 9: Slice along the x-axis in 3-D cartesian geometry at $t = 443$ s showing positive (blue) and negative (red) radial velocities in the core of a WD. Contours in zero specific energy generation are shown in purple. The central density is 4.5×10^9 g cm^{-3} and central temperature is 5.5×10^8 K. Simulation time is 443 s.

Corresponding with this radial velocity structure is the specific energy generation rate, shown in Figure 10 with positive energy generation (green) and negative energy generation (magenta) denoted. Positive energy generation interior to about 200 km in radius indicates the central ^{12}C-burning region, which drives the convection. The negative energy generation region between 200 km and 400 km in radius is where electron captures occur rapidly enough on ^{23}Na so as to provide local cooling. It is possible for ^{23}Na to enter this region in two ways, being brought up from the core as a product of ^{12}C fusion, or transported down from above

the A = 23 Urca shell at 400 km in radius. Outside this Urca shell, convection brings ^{23}Ne up to lower densities than the core where it may beta decay, yielding the ring of positive energy generation there. Waves of energy generation are visible here at the top of the convection zone and the velocity structure is also evident in the electron-capture region below. This demonstrates that the structure of the convection is a source of spatial asymmetries in the energy generation due to the degree of local mixing across the Urca shell and the direction of flow.

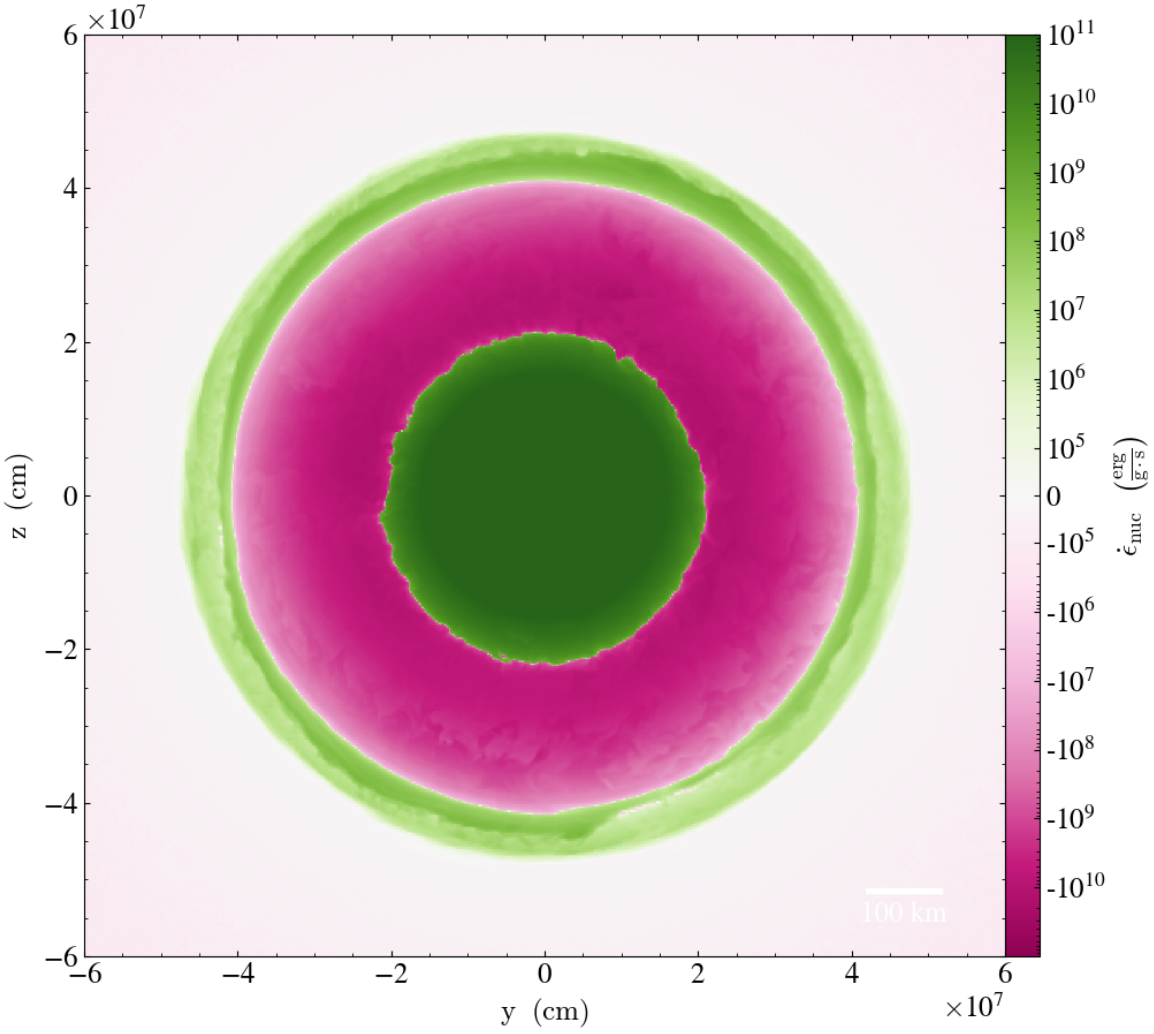

Figure 10: Slice along the x-axis in 3-D cartesian geometry at $t = 443$ s showing positive (green) and negative (magenta) specific energy generation in the core of a WD. The central density is 4.5×10^9 g cm^{-3} and central temperature is 5.5×10^8 K.

To complement the velocity and energy generation structure we also show the electron fraction asymmetry, which we define as $Y_e - 0.5$ and plot in Figure 11. On this scale negative numbers with a larger magnitude indicate neutron-rich regions compared to negative numbers with a smaller magnitude, and the effect of the A = 23 Urca shell is to divide the

star into two regions by composition. Outside the Urca shell at 400 km, the WD has no ^{23}Ne, it having beta decayed to ^{23}Na. Within and across the Urca shell we see that the effect of the convection zone is to transport material from within the Urca shell to the overlying region and to transport material from above the Urca shell to the core. Orange indicates regions close to the Urca shell where both ^{23}Na and ^{23}Ne are present in significant quantities because the electron capture and beta decay rates coupling them to each other are competitive. One of the important features of this plot is that the composition does not feature a sharp, discontinuous jump at the Urca shell. Rather, the composition changes along the path of the convective plumes in an extended region from the center of the WD to outside the Urca shell.

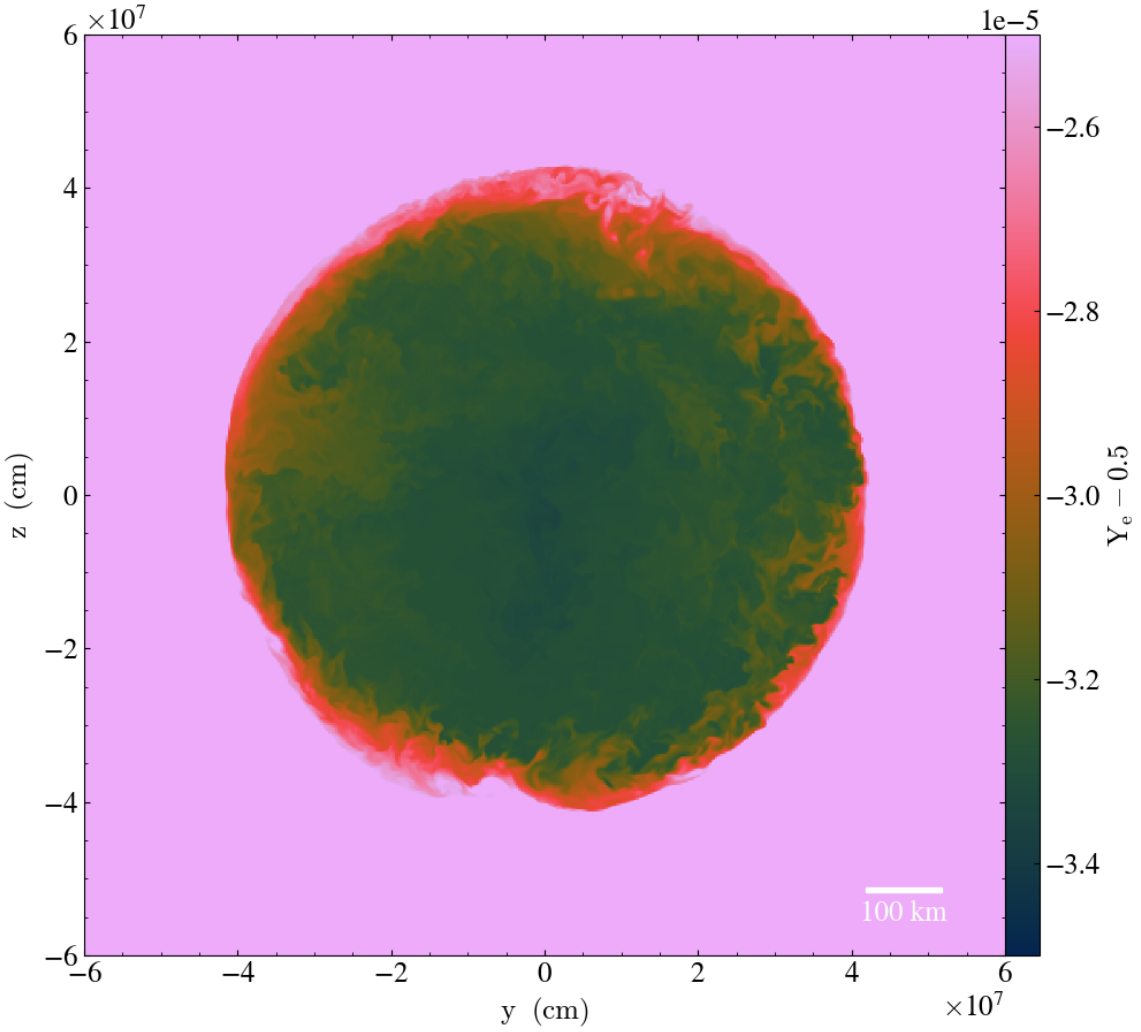

Figure 11: Slice along the x-axis in 3-D cartesian geometry at $t = 443$ s showing the electron fraction asymmetry $Y_e - 0.5$ in the core of a WD. The central density is 4.5×10^9 g cm^{-3} and central temperature is 5.5×10^8 K.

We also evaluate the ^{12}C burning products to assess the extent of mixing of material

from the ^{12}C-burning core upwards past the Urca shell, as also done by Stein & Wheeler (2006). For this purpose we plot the quantity $0.5 - X(^{12}\mathrm{C})$, labeled as `xc12_complement` in Figure 12. Recall that we initialize this WD model with $\mathrm{X}(^{12}\mathrm{C}) = 0.39975$ so the 0.5 in this quantity is merely to provide a convenient reference point. We see that there is a high concentration of ^{12}C burning products in the core of the WD where ^{12}C burning is rapid and that its burning products are spread by convection to the top of the convective zone near 400 km in radius. No significant mixing spreads ^{12}C burning products above the Urca shell, suggesting that neutronization during ^{12}C burning explored by Martínez-Rodríguez et al. (2016) at even the high temperature of 5.5×10^8 K affects only the region interior to the A = 23 Urca shell.

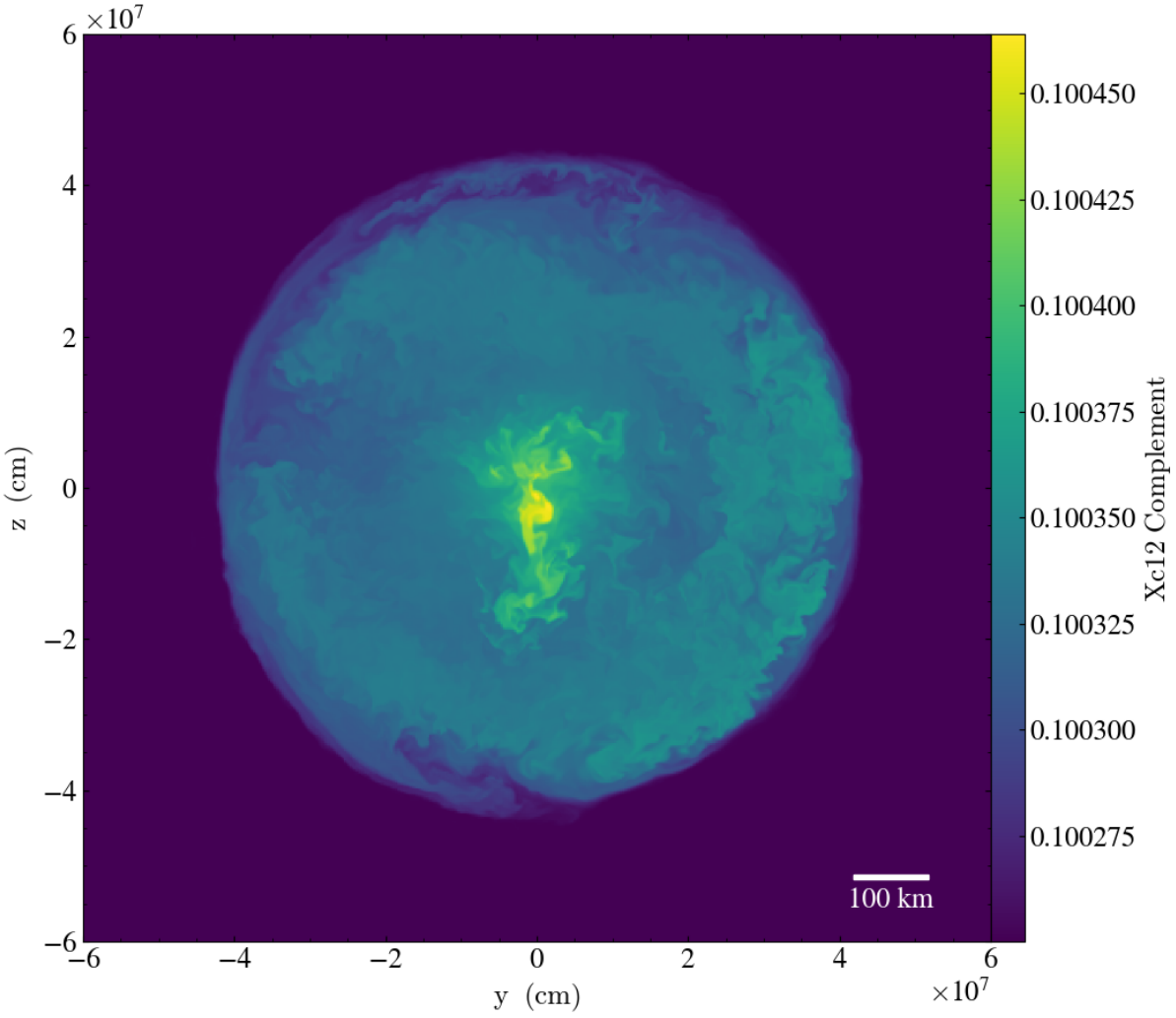

Figure 12: Slice along the x-axis in 3-D cartesian geometry showing $0.5 - \mathrm{X}(^{12}\mathrm{C})$, a scaled proxy for the ^{12}C burning products in the core of a WD including the A = 23 Urca reactions simulated with Maestro. Within approximately 10^8 g cm^{-3}, the WD core is resolved to 2.5 km using 4 levels of refinement to resolve the energy generating regions. The WD shown has central density 4.5×10^9 g cm^{-3} and central temperature 5.5×10^8 K. Simulation time is 443 s.

7.3 Central Density: 5.5×10^9 g cm^{-3}

For the WD model with central density 5.5×10^9 g cm^{-3} and central temperature 5.5×10^8 K, we plot the radial velocity in Figure 13. Under these conditions the central convection extends just across the A = 23 Urca shell near 400 km in radius. Above this radius, the convective eddy turnovers excite gravity waves that propagate throughout the outer regions of the white dwarf at significantly lower velocities. Both convection and gravity waves contribute to the Urca reactions via species mixing near the Urca shell. As before, we plot contours in zero specific energy generation rate to easily identify the Urca shell in the convection zone, and we see that it is just inwards of the top of the convective plumes. Convection does not progress significantly beyond the Urca shell at this central temperature but still mixes material across the Urca shell to sustain a convective Urca process.

We can compare this convective velocity field with the specific energy generation of this model in Figure 14 to show the result of mixing material across the Urca shell. We complement this picture with the electron fraction asymmetry ($Y_e - 0.5$) in Figure 15 to show the spatial extent over which electron captures neutronize the material brought down from above the Urca shell. We note that the extent of convection to transport ^{23}Ne above the Urca shell is more limited than for the lower density WD model we explore in subsection 7.2.

We observe that the largest concentration of ^{12}C burning products is at the WD center where the ^{12}C burning rate is the fastest because of the high central temperature. The ^{12}C burning products are then distributed by convection throughout the WD core within the Urca shell, but the region above the Urca shell is not mixed with the core and therefore lacks any products of ^{12}C burning. From this we can conclude that the Urca shell acts as a boundary for the convective zone similar to the findings of Stein & Wheeler (2006) for their model labeled "S-4-2E4" which seeded the WD with X(^{23}Ne) $= 4 \times 10^{-4}$ inside the A = 23 Urca shell and the same value of X(^{23}Na) outside it. For that model, Stein & Wheeler (2006) also multiplied reaction rates by a factor of 2×10^4 and Urca rates by a factor of 2×10^3. The fact that we see similar behavior, albeit for a different central density and temperature, suggests that the convective zone bounding they observe was likely not an unphysical result introduced by their artificially scaled reaction rates or 2D geometry.

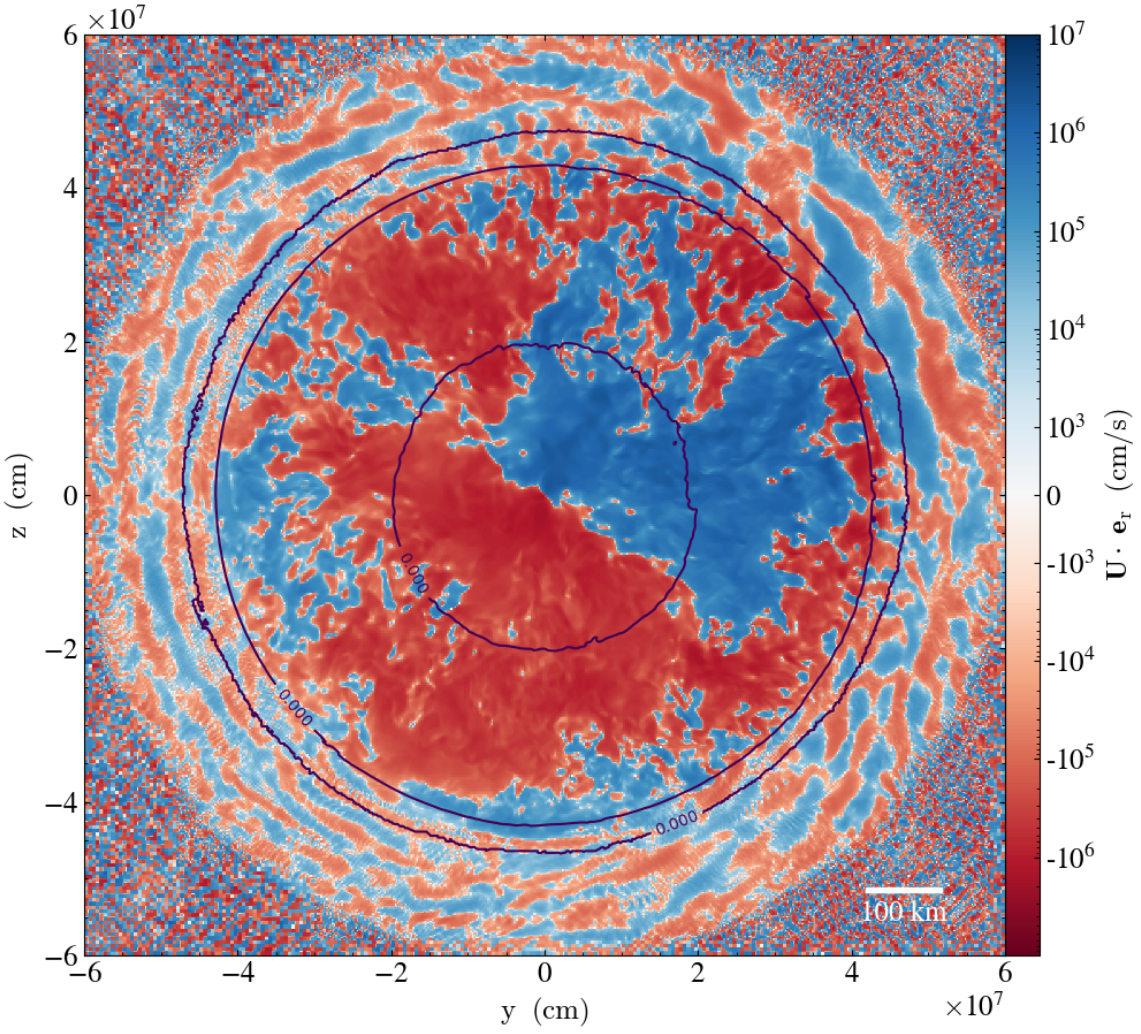

Figure 13: Slice along the x-axis in 3-D cartesian geometry showing positive (blue) and negative (red) radial velocities in the core of a WD including the A = 23 Urca reactions simulated with Maestro. Contours of zero specific energy generation are plotted in purple. Within approximately 10^8 g cm^{-3}, the WD core is resolved to 2.5 km using 4 levels of refinement to resolve the energy generating regions. The WD shown has central density 5.5×10^9 g cm^{-3} and central temperature 5.5×10^8 K. Simulation time is 356 s.

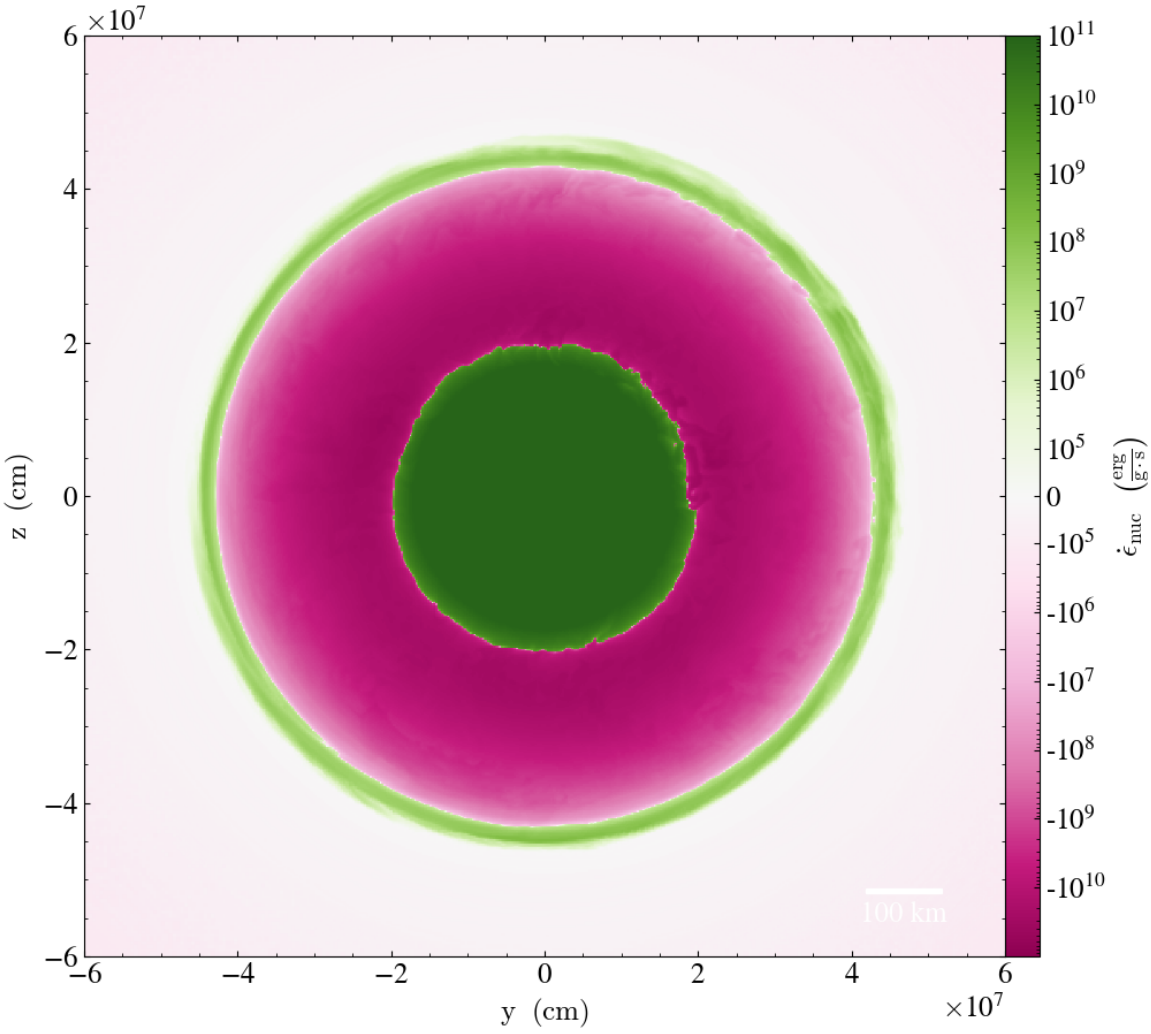

Figure 14: Slice along the x-axis in 3-D cartesian geometry at $t = 356$ s showing positive (green) and negative (magenta) specific energy generation in the core of a WD. The central density is 5.5×10^9 g cm^{-3} and central temperature is 5.5×10^8 K.

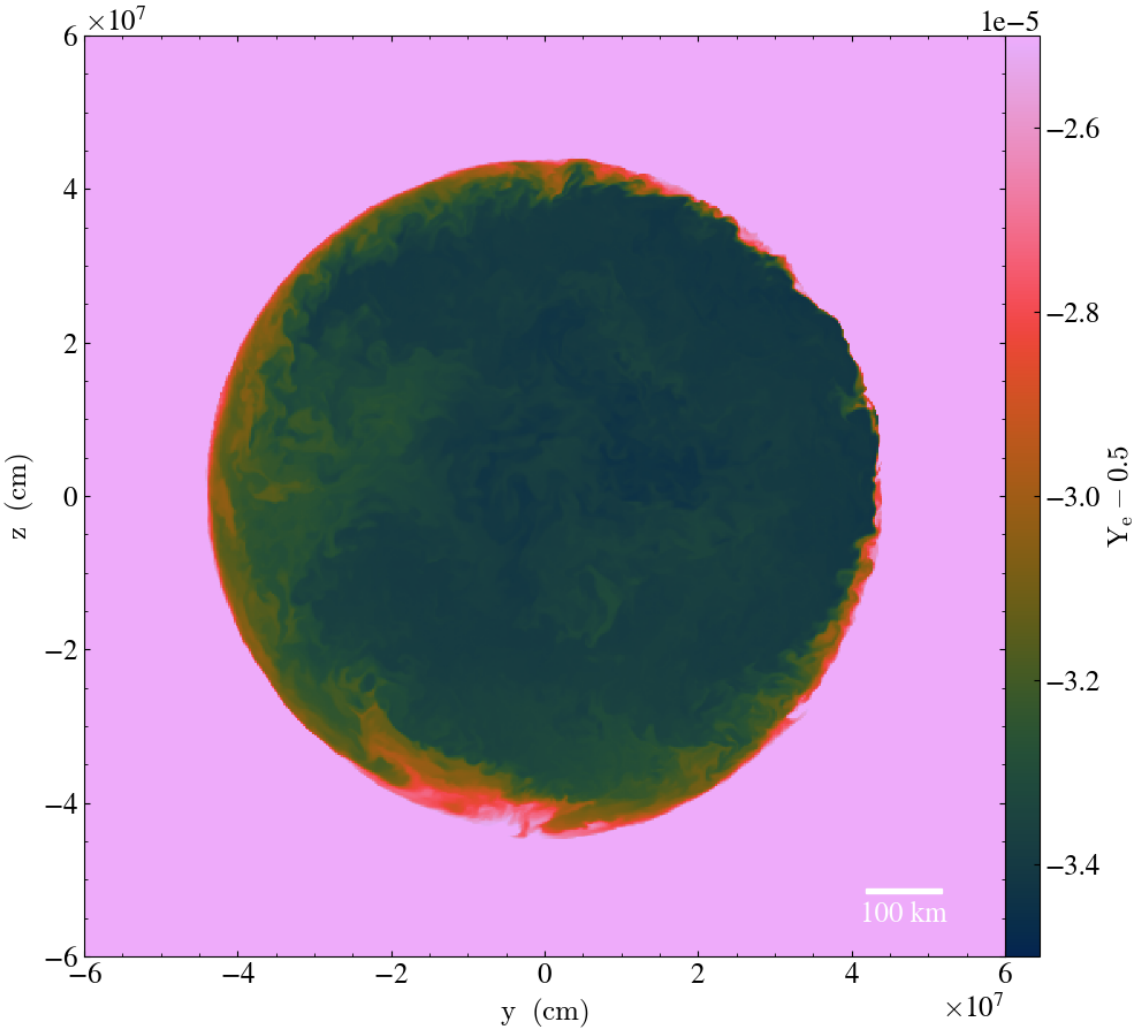

Figure 15: Slice along the x-axis in 3-D cartesian geometry at $t = 356$ s showing the electron fraction asymmetry $Y_e - 0.5$ in the core of a WD. The central density is 5.5×10^9 g cm^{-3} and central temperature is 5.5×10^8 K.

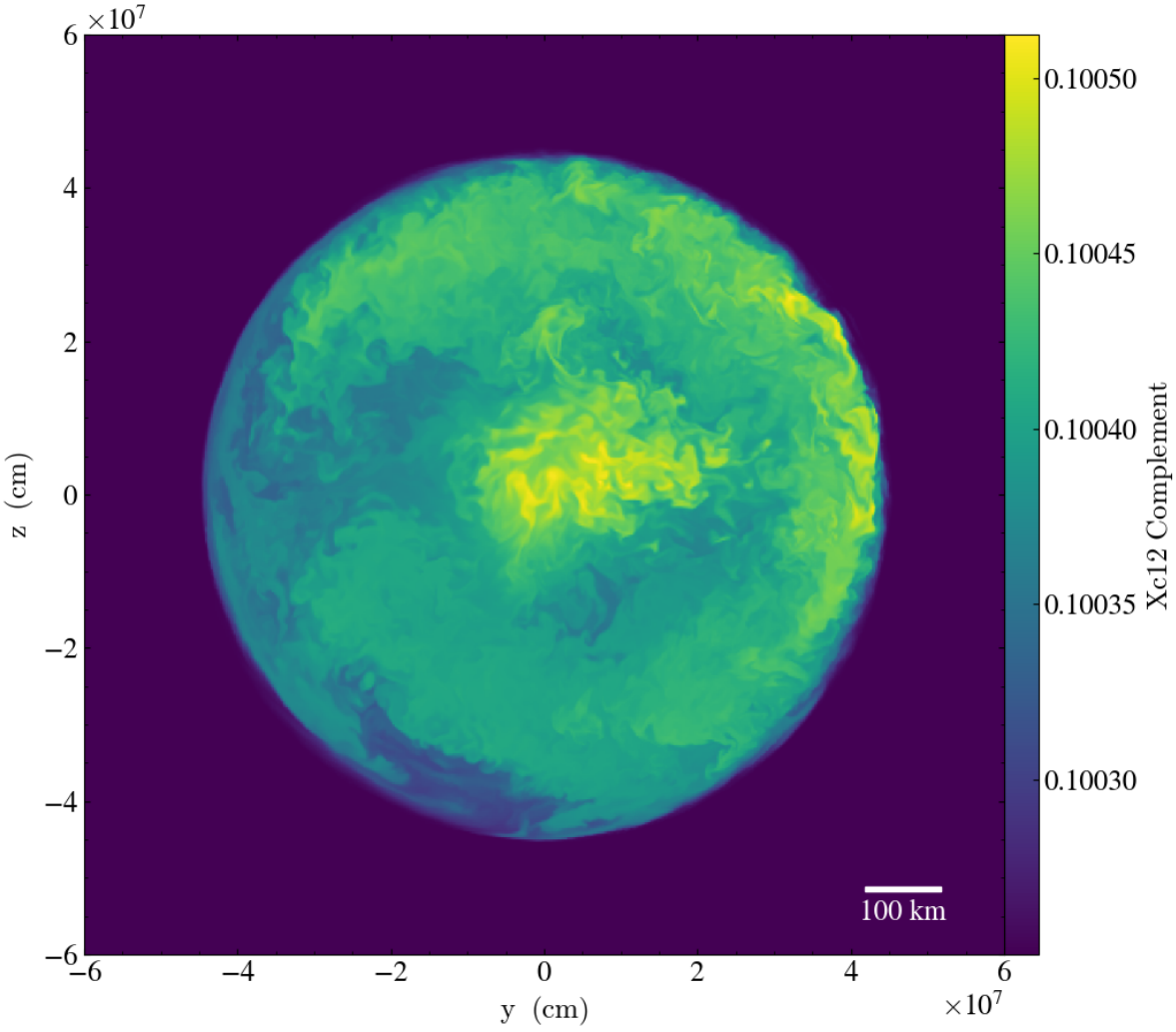

Figure 16: Slice along the x-axis in 3-D cartesian geometry showing $0.5 - \mathrm{X}(^{12}\mathrm{C})$, a scaled proxy for the ^{12}C burning products in the core of a WD including the A = 23 Urca reactions simulated with Maestro. Within approximately 10^8 g cm^{-3}, the WD core is resolved to 2.5 km using 4 levels of refinement to resolve the energy generating regions. The WD shown has central density 5.5×10^9 g cm^{-3} and central temperature 5.5×10^8 K. Simulation time is 356 s.

7.4 Central Density: 3.5×10^9 g cm^{-3}

We also carried out simulations of a WD model with central density 3.5×10^9 g cm^{-3} and central temperature 3×10^8 K, for comparison with the two dimensional simulations of Stein & Wheeler (2006). Initialization of this model is described in section 6, and we evolve this model to 460 s with a spatial resolution of 2.5 km using 4 spatial levels in Maestro. We show the central convection zone using the radial velocities plotted in Figure 17. The bulk of the large scale central convective flow at the highest velocities appears limited to approximately 350 km which is the location of the A = 23 Urca shell for this central density. Outside this region out to 600 km in radius, the velocity structure is imprinted with gridding artifacts that limit our ability to predict the behavior of the flow outside the Urca shell. The fact that these artifacts are visible in this simulation and not our simulations at other densities may be related to the fact that in this simulation we initialize slow convective flow outside the Urca shell at $t = 0$ to attempt consistency with the estimated extent of the convective zone that Stein & Wheeler (2006) used in their initialization. It may be, however, that this region is stable against convection due to the effects of the convective Urca process.

It is noteworthy that the extent of the central convection zone appears limited to the region inside the A = 23 Urca shell, which agrees well with the convective structure of Stein & Wheeler (2006) in their Figure 3c. While Stein & Wheeler (2006) use the distribution of ^{12}C burning products as their proxy for assessing the extent of mixing above the WD core, it is evident from their velocity arrows that the central convective zone is limited in this way. An important point of comparison is that the geometry of the convection is very different between our Figure 17 and the results of Stein & Wheeler (2006) in which convection appears as a large-scale extended swirl instead of the more jet-like structures we obtain. This is a result of the two-dimensionality of the Stein & Wheeler (2006) study and the inversion of the turbulence cascade to large wavenumbers which occurs in 2D, see Boffetta & Ecke (2012) for a recent review of two-dimensional turbulence.

We also show the specific energy generation rate in Figure 18, where we observe the importance of convection in setting up the geometry of the energy-generating regions. The ^{12}C burning region in the core, for example, is in some places dominated in energy by electron captures onto ^{23}Na both produced by ^{12}C-^{12}C fusion and brought into the core from outside the Urca shell. Because the ^{12}C burning rate is largely independent of the presence of ^{23}Na, it is likely that ^{23}Na transported into the core is responsible for the locally endothermic regions in the center of the WD. Outside the Urca shell small waves and plumes are visible where locally exothermic beta decays deposit some of the ^{12}C-burning energy transported upwards from the core and stored as the binding energy of ^{23}Ne. No beta decays occur outside a radius of 500 km as a result of the limited extent of the central convection zone.

As before, we also demonstrate the composition structure deriving from this convective structure using the electron fraction asymmetry $Y_e - 0.5$ in Figure 19, which shows a sharp transition in electron fraction at the Urca shell. We note that we used relative and absolute tolerances of 1×10^{-12} for the species mass fractions in the reaction network integration for this simulation, and that the ^{12}C burning rate is sufficiently low at the central temperature of 3.0×10^8 K that although we obtain energy generation from ^{12}C burning, we do not track the small changes in ^{12}C mass fraction over the course of the simulation. Since we capture the energy generation, however, we can interpret these results as indicating the global dynamics

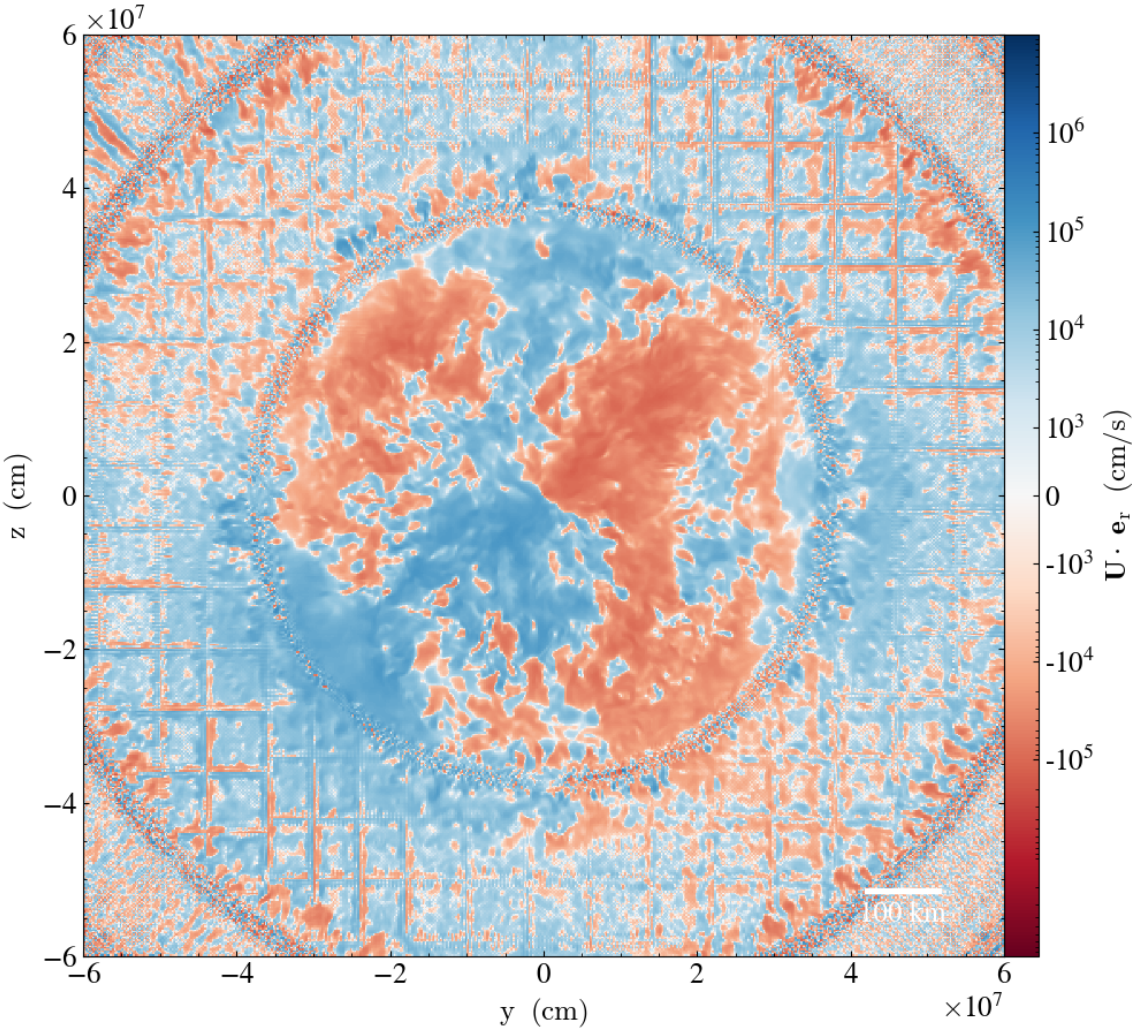

Figure 17: Slice along the x-axis in 3-D cartesian geometry at $t = 460$ s showing positive (blue) and negative (radial) radial velocities in the core of a WD. The central density is 3.5×10^9 g cm^{-3} and central temperature is 3.0×10^8 K.

of the WD over the few minutes we simulated.

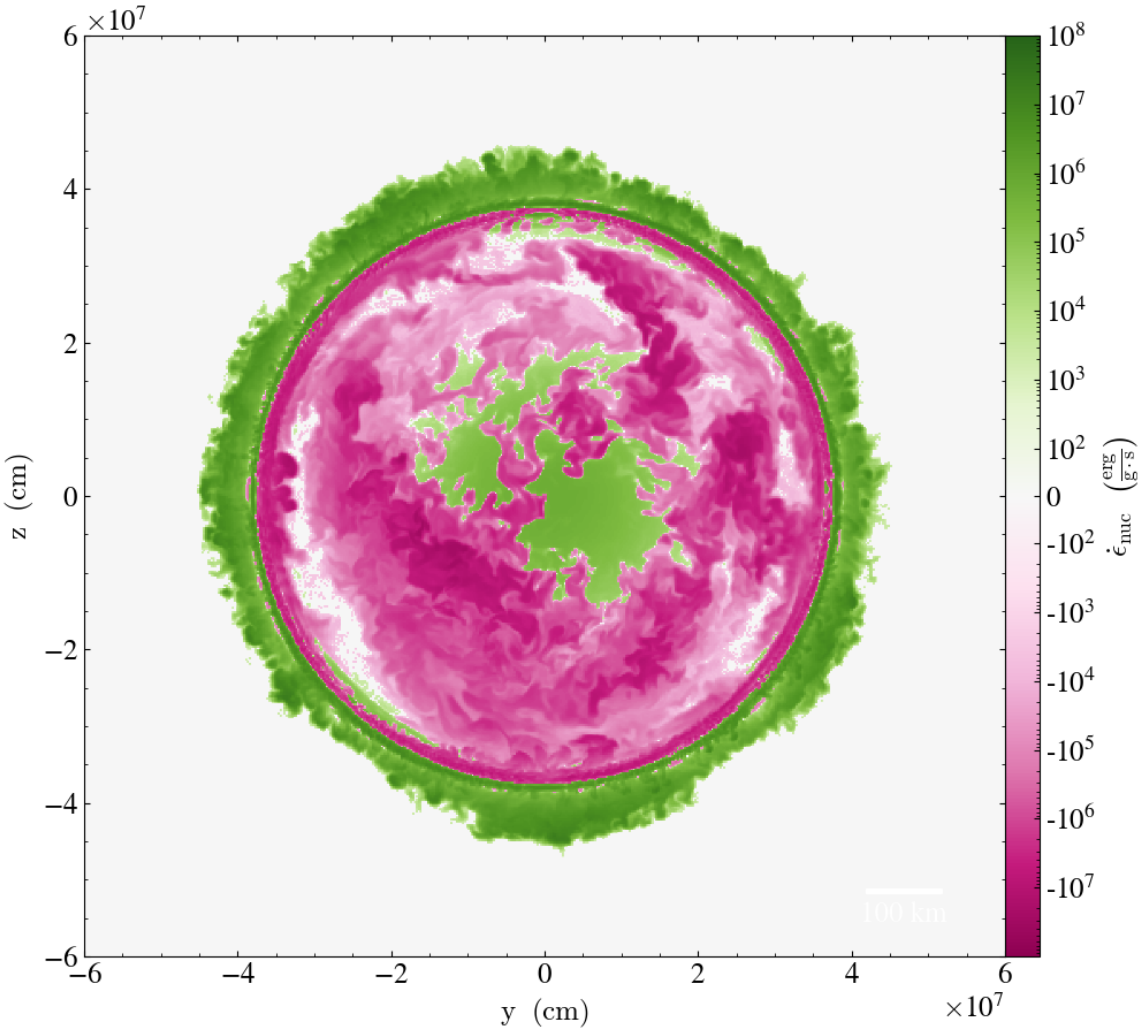

Figure 18: Slice along the x-axis in 3-D cartesian geometry at $t = 460$ s showing positive (green) and negative (magenta) specific energy generation in the core of a WD. The central density is 3.5×10^9 g cm^{-3} and central temperature is 3.0×10^8 K.

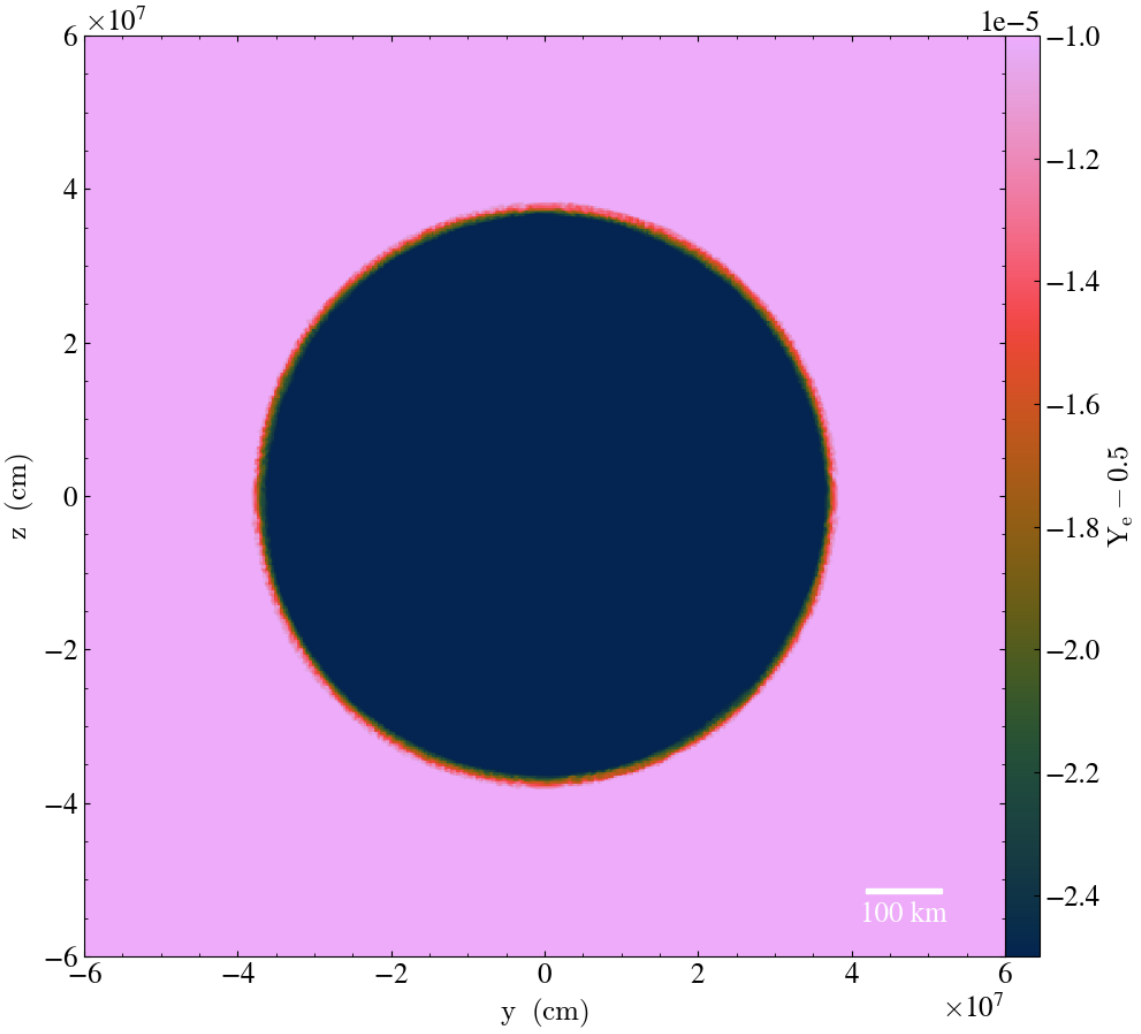

Figure 19: Slice along the x-axis in 3-D cartesian geometry at $t = 460$ s showing the electron fraction asymmetry $Y_e - 0.5$ in the core of a WD. The central density is 3.5×10^9 g cm^{-3} and central temperature is 3.0×10^8 K.

8 Conclusions for the Urca Study

We have presented exploratory 3D simulations of WD convection in the presence of the A = 23 convective Urca process for two central densities at temperatures well within the carbon simmering phase for Chandrasekhar mass WDs. We show that although the convection zone does not extend significantly beyond the Urca shell under these conditions, convection mixes material sufficiently across the Urca shell that a single ^{23}Na or ^{23}Ne nucleus could undergo cycles of electron capture or beta decay as it is carried by the convection. While this is the most important outcome of our study, we also established a method for carrying out Urca process simulations using Maestro which has opened several possibilities for future work.

One of the important questions remaining concerns the behavior of convection around the Urca shell as the WD approaches thermonuclear runaway, and the issue of whether convection overwhelms the containing effects of the convective Urca process and under what conditions. The best way to approach this is to perform simulations at higher central temperatures such as 6.25×10^8 K, as used by Zingale et al. (2011), where the WD will be just a few hours from runaway ignition and the convection zone is expected to extend significantly further in radius. Although the convection zone in our current simulations at 5.5×10^8 K does not extend significantly beyond the A = 23 Urca shell, such simulations at higher temperatures will also make it important to consider another effect as discussed next.

Prior studies, most recently Martínez-Rodríguez et al. (2016), show that another Urca pair operating under conditions appropriate to these WD cores is the ^{25}Na/^{25}Mg pair. This pair possesses a lower Urca threshold density for electron captures onto ^{25}Mg of $\log_{10}(\rho Y_e) = 8.77$ (with $Q = 3.83$ MeV), compared to $\log_{10}(\rho Y_e) = 8.92$ (with $Q = 4.38$ MeV) for the A = 23 Urca pair we studied (Suzuki et al., 2016). This suggests that the A = 25 Urca process will be active at lower densities, and thus larger radii, and will also influence the energy generation in the WD less strongly for a given combination of electron capture and β^--decay processes compared to the A = 23 Urca process. This assessment is consistent with the findings of Martínez-Rodríguez et al. (2016) as shown in their Figure 2, where the cooling effect when the A = 25 process activates is less than for the A = 23 process. If we were to add the A = 25 Urca process to our current simulations we could assess the degree to which gravity waves slosh material across the A = 25 Urca shell to drive reactions, but it would likely not be convectively driven. We thus chose to explore the A = 23 process for its greater importance and the simplicity of assessing the effect of a single Urca process before adding complexity. However, the A = 25 Urca process would be significant for simulations of thermonuclear runaway, as described above.

References

Alastuey, A., & Jancovici, B. 1978, The Astrophysical Journal, 226, 1034

Almgren, A. S., Bell, J. B., Nonaka, A., & Zingale, M. 2008, \ApJ, 684, 449

Almgren, A. S., Bell, J. B., Rendleman, C. A., & Zingale, M. 2006a, Astrophysical Journal, 637, 922

—. 2006b, Astrophysical Journal, 649, 927

Almgren, A. S., Beckner, V. E., Bell, J. B., et al. 2010, The Astrophysical Journal, 715, 1221

Arnett, W. D., Truran, J. W., & Woosley, S. E. 1971, Astrophysical Journal, 165, 87

Boffetta, G., & Ecke, R. E. 2012, Annual Review of Fluid Mechanics, 44, 427

Brown, P., Byrne, G., & Hindmarsh, A. 1989, SIAM Journal on Scientific and Statistical Computing, 10, 1038

Bruenn, S. W. 1973, The Astrophysical Journal Letters, 183, L125

Calder, A. C., Krueger, B. K., Jackson, A. P., et al. 2010, ArXiv e-prints, arXiv:1011.4022

Calder, A. C., Krueger, B. K., Jackson, A. P., et al. 2017, 837, 012005

Chen, M. C., Herwig, F., Denissenkov, P. A., & Paxton, B. 2014, Monthly Notices of the Royal Astronomical Society, 440, 1274

Colgate, S. A., & McKee, C. 1969, Astrophysical Journal, 157, 623

Couch, R. G., & Arnett, D. W. 1974, \ApJ, 194, 537

Couch, R. G., & Arnett, W. D. 1973, \ApJL, 180, L101

—. 1975, The Astrophysical Journal, 196, 791

Cyburt, R. H., Amthor, A. M., Ferguson, R., et al. 2010, The Astrophysical Journal Supplement Series, 189, 240

Dan, M., Rosswog, S., Brüggen, M., & Podsiadlowski, P. 2014, Monthly Notices of the Royal Astronomical Society, 438, 14

Denissenkov, P. A., Herwig, F., Truran, J. W., & Paxton, B. 2013, Astrophysical Journal, 772, 37

Denissenkov, P. A., Truran, J. W., Herwig, F., et al. 2015, Monthly Notices of the Royal Astronomical Society, 447, 2696

Dewitt, H. E., Graboske, H. C., & Cooper, M. S. 1973, Astrophysical Journal, 181, 439

Fuller, G. M., Fowler, W. A., & Newman, M. J. 1980, \ApJS, 42, 447

García-Senz, D., & Bravo, E. 2005, Astronomy and Astrophysics, 430, 585

Graboske, H. C., Dewitt, H. E., Grossman, A. S., & Cooper, M. S. 1973, Astrophysical Journal, 181, 457

Höflich, P., Khokhlov, A. M., & Wheeler, J. C. 1995, Astrophysical Journal, 444, 831

Hoyle, F., & Fowler, W. A. 1960, Astrophysical Journal, 132, 565

Huang, W., Audi, G., Wang, M., et al. 2017, Chinese Physics C, 41, 030002

Iben, Jr., I. 1978a, Astrophysical Journal, 226, 996

—. 1978b, Astrophysical Journal, 219, 213

—. 1982, Astrophysical Journal, 253, 248

Iben, Jr., I., & Tutukov, A. V. 1984, Astrophysical Journal Supplement, 54, 335

Ichimaru, S. 1993, Reviews of Modern Physics, 65, 255

Itoh, N., Hayashi, H., Nishikawa, A., & Kohyama, Y. 1996, Astrophysical Journal Supplement, 102, 411

Itoh, N., Tomizawa, N., Tamamura, M., Wanajo, S., & Nozawa, S. 2002, The Astrophysical Journal, 579, 380

Itoh, N., Totsuji, H., Ichimaru, S., & Dewitt, H. E. 1979, The Astrophysical Journal, 234, 1079

Jacobs, A. M., Zingale, M., Nonaka, A., Almgren, A. S., & Bell, J. B. 2016, The Astrophysical Journal, 827, 84

Jones, E., Oliphant, T., Peterson, P., et al. 2001, SciPy: Open source scientific tools for Python, [Online; accessed 2018-07-18]

Jordan, IV, G. C., et al. 2008, Astrophysical Journal, 681, 1448

Kashyap, R., Fisher, R., García-Berro, E., et al. 2015, Astrophysical Journal Letters, 800, L7

Katz, M. P., Zingale, M., Calder, A. C., et al. 2016, Astrophysical Journal, 819, 94

Khokhlov, A. M. 1991, Astronomy and Astrophysics, 245, 114

Krueger, B. K., Jackson, A. P., Calder, A. C., et al. 2012, Astrophysical Journal, 757, 175

Krueger, B. K., Jackson, A. P., Townsley, D. M., et al. 2010, Astrophysical Journal Letters, 719, L5

Lazareff, B. 1975, Astronomy and Astrophysics, 45, 141

Lesaffre, P., Podsiadlowski, P., & Tout, C. A. 2005, Monthly Notices of the Royal Astronomical Society, 356, 131

Lippuner, J., & Roberts, L. F. 2017, The Astrophysical Journal Supplement Series, 233, 18

Livio, M., & Mazzali, P. 2018, Physics Reports, 736, 1

Livne, E., & Arnett, D. 1993, The Astrophysical Journal Letters, 415, L107

Malone, C. M., Nonaka, A., Almgren, A. S., Bell, J. B., & Zingale, M. 2011, The Astrophysical Journal, 728, 118

Malone, C. M., Zingale, M., Nonaka, A., Almgren, A. S., & Bell, J. B. 2014, The Astrophysical Journal, 788, 115

Maoz, D., & Mannucci, F. 2012, Publ. Astron. Soc. Aust., 29, 447

Martínez-Rodríguez, H., Piro, A. L., Schwab, J., & Badenes, C. 2016, The Astrophysical Journal, 825, 57

Mazzali, P. A., Nomoto, K., Cappellaro, E., et al. 2001, The Astrophysical Journal, 547, 988

Mazzali, P. A., & Podsiadlowski, P. 2006, Monthly Notices of the Royal Astronomical Society, 369, L19

Meurer, A., Smith, C. P., Paprocki, M., et al. 2017, PeerJ Computer Science, 3, e103

Miles, B. J., van Rossum, D. R., Townsley, D. M., et al. 2016, The Astrophysical Journal, 824, 59

Mohr, P. J., Newell, D. B., & Taylor, B. N. 2016, Rev. Mod. Phys., 88, 035009

Moll, R., Raskin, C., Kasen, D., & Woosley, S. E. 2014, Astrophysical Journal, 785, 105

Nomoto, K., Thielemann, F.-K., & Yokoi, K. 1984, Astrophysical Journal, 286, 644

Nonaka, A., Almgren, A. S., Bell, J. B., et al. 2010, \ApJS, 188, 358

Paczyński, B. 1972, Astrophysical Letters, 11, 53

Perlmutter, S., Gabi, S., Goldhaber, G., et al. 1997, The Astrophysical Journal, 483, 565

Phillips, M. M. 1993, Astrophysical Journal Letters, 413, L105

Rauscher, T. 2003, The Astrophysical Journal Supplement Series, 147, 403

Rauscher, T., & Thielemann, F. 2000, At. Data Nucl. Data Tables, 75, 1

Riess, A. G., Filippenko, A. V., Challis, P., et al. 1998, Astronomical Journal, 116, 1009

Röpke, F. K., Hillebrandt, W., Schmidt, W., et al. 2007, Astrophysical Journal, 668, 1132

Rosswog, S., Kasen, D., Guillochon, J., & Ramirez-Ruiz, E. 2009, Astrophysical Journal Letters, 705, L128

Sato, Y., Nakasato, N., Tanikawa, A., et al. 2015, Astrophysical Journal, 807, 105

Schwab, J., Bildsten, L., & Quataert, E. 2017a, Monthly Notices of the Royal Astronomical Society, 472, 3390, arXiv: 1708.07514

Schwab, J., Martínez-Rodríguez, H., Piro, A. L., & Badenes, C. 2017b, The Astrophysical Journal, 851, 105, arXiv: 1711.04780

Shen, K. J., & Bildsten, L. 2014, The Astrophysical Journal, 785, 61

Slattery, W. L., Doolen, G. D., & Dewitt, H. E. 1982, Physical Review A, 26, 2255

Stein, J., & Wheeler, J. C. 2006, Astrophysical Journal, 643, 1190

Suzuki, T., Toki, H., & Nomoto, K. 2016, The Astrophysical Journal, 817, 163

Tanikawa, A., Nakasato, N., Sato, Y., et al. 2015, Astrophysical Journal, 807, 40

Timmes, F. X., & Swesty, F. D. 2000, Astrophysical Journal Supplement, 126, 501

Tremblay, P.-E., Cummings, J., Kalirai, J. S., et al. 2016, Monthly Notices of the Royal Astronomical Society, 461, 2100

Wang, M., Audi, G., Kondev, F., et al. 2017, Chinese Physics C, 41, 030003

Webbink, R. F. 1984, Astrophysical Journal, 277, 355

Willcox, D. E., Townsley, D. M., Calder, A. C., Denissenkov, P. A., & Herwig, F. 2016, The Astrophysical Journal, 832, 13

Willcox, D. E., & Zingale, M. 2018, The Journal of Open Source Software, 3, 588

Woosley, S. E., & Weaver, T. A. 1986, Annual Review of Astronomy and Astrophysics, 24, 205

Woosley, S. E., Wunsch, S., & Kuhlen, M. 2004, Astrophysical Journal, 607, 921

Zingale, M., Almgren, A. S., Bell, J. B., Nonaka, A., & Woosley, S. E. 2009, Astrophysical Journal, 704, 196

Zingale, M., Nonaka, A., Almgren, A. S., et al. 2013, The Astrophysical Journal, 764, 97

Zingale, M., Nonaka, A., Almgren, A. S., et al. 2011, Astrophysical Journal, 740, 8

Zingale, M., Almgren, A. S., Sazo, M. G. B., et al. 2018, Journal of Physics: Conference Series, 1031, 012024

A GPU Acceleration for Reaction Networks

One of the commonly used ODE integrators for evolving reaction networks in Maestro and Castro simulations is the variable-order VODE package Brown et al. (1989) which we include in our StarKiller Microphysics repository. Because evolving reactions can be an expensive part of a total simulation we have implemented a port of VODE to CUDA Fortran for offloading our reaction network integration onto GPU accelerators. The goal of this project is to accelerate reaction network integration on GPU-based supercomputing systems such as OLCF Summit. This development effort has already yielded performance improvements for networks with up to 13 species in test problems and my ongoing work will extend these gains to larger networks. We show in Figure 20 the speedup of the CUDA Fortran VODE implicit integration on a Tesla P100 GPU compared to a single core of a Power 8 CPU, run on the Summitdev test machine at OLCF. Efficient ODE integration on GPUs will allow the hydrodynamics codes Maestro and Castro to offload reaction network integration to GPUs. For further discussion of this project in the context of the AMReX astrophysics codes, see Zingale et al. (2018).

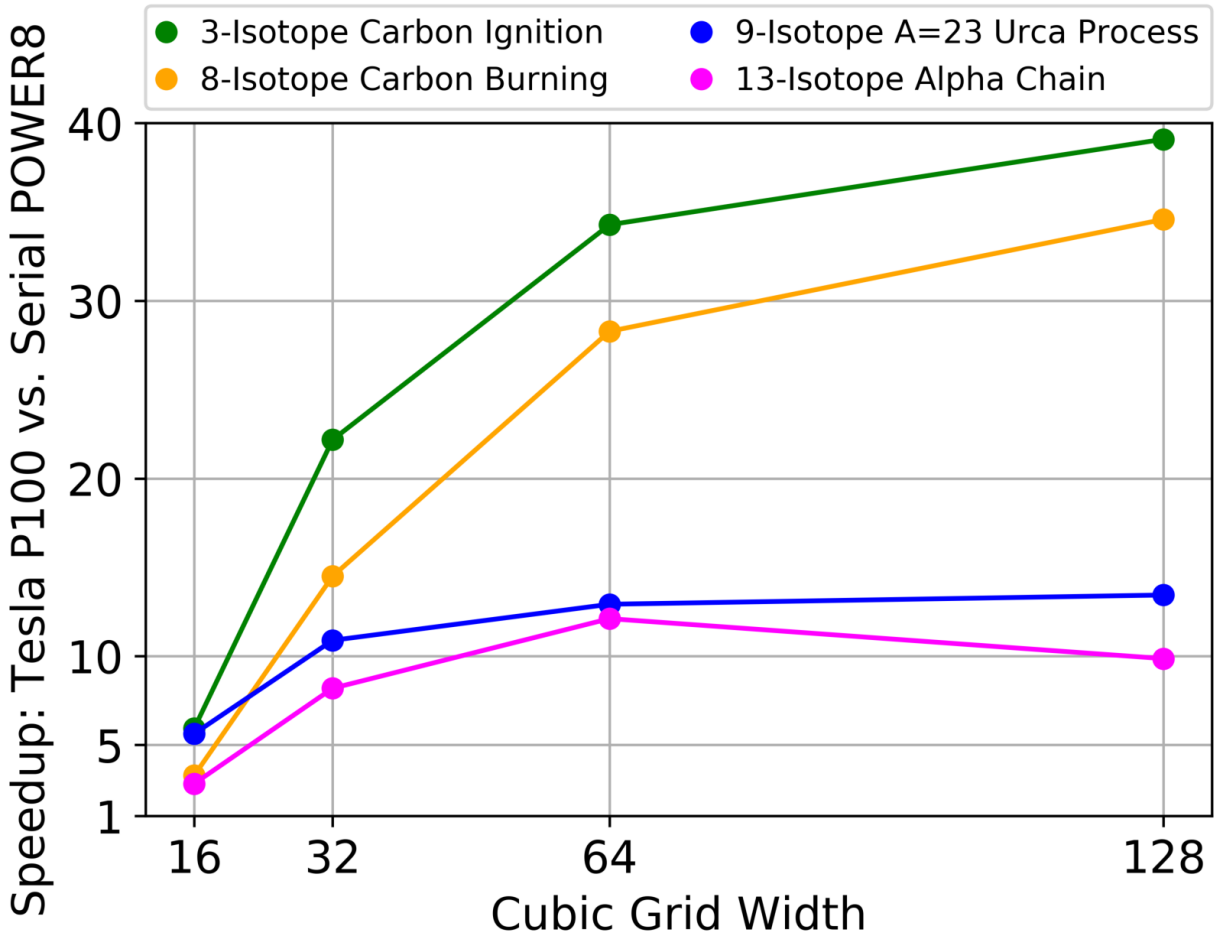

Figure 20: Speedup of VODE implicit integration using CUDA Fortran on a Tesla P100 GPU compared to a single Power8 CPU core for several reaction networks. The 3-isotope carbon burning network has been used in previous Maestro simulations of WD convection and I am currently using the 9-isotope Urca network for the A = 23 WD Urca process. The 8-isotope carbon burning network is the Urca network without tabulated weak reactions, and the 13-isotope approximate alpha chain network is for explosive burning problems.